THE JOURNAL OF PHYSICAL CHEMISTRY C

Article

pubs.acs.org/JPCC

Light Harvesting and Charge Separation in a π-Conjugated Antenna Polymer Bound to TiO_2

Gyu Leem,[†] Zachary A. Morseth,[‡] Egle Puodziukynaite,[†] Junlin Jiang,[†] Zhen Fang,[‡] Alexander T. Gilligan,[‡] John R. Reynolds,[§] John M. Papanikolas,*[,‡] and Kirk S. Schanze*[,†]

[†]Department of Chemistry, University of Florida, Gainesville, Florida 32611, United States

[‡]Department of Chemistry, University of North Carolina at Chapel Hill, Chapel Hill, North Carolina 27599, United States

[§]School of Chemistry and Biochemistry, School of Materials Science and Engineering, Center for Organic Photonics and Electronics, Georgia Institute of Technology, Atlanta, Georgia 30332, United States

Supporting Information

ABSTRACT: This paper describes the photophysical and photoelectrochemical characterization of a light harvesting polychromophore array featuring a polyfluorene backbone with covalently attached Ru(II) polypyridyl complexes (PF-Ru-A), adsorbed on the surface of mesostructured TiO_2 (PF-Ru-A//TiO_2). The surface adsorbed polymer is characterized by transmission electron microscopy (TEM), scanning electron microscopy (SEM), and attenuated total reflectance-Fourier transform infrared (ATR-FTIR) spectroscopy, providing evidence for the morphology of the surface adsorbed polymer and the mode of binding. Photoexcitation of the Ru(II) complexes bound to the metal oxide surface (proximal) results in electron injection into the conduction band of TiO_2, which is then followed by ultrafast hole transfer to the polymer to form oxidized polyfluorene (PF^+). More interestingly, chromophores that are not directly bound to the TiO_2 interface (distal) that are excited participate in site-to-site energy transfer processes that transport the excited state to surface bound chromophores where charge injection occurs, underscoring the antenna-like nature of the polymer assembly. The charge separated state is long-lived and persists for >100 μs, a consequence of the increased separation between the hole and injected electron.

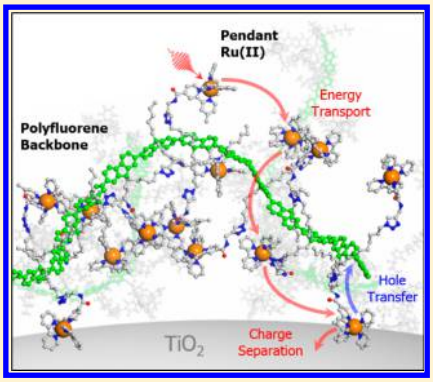

INTRODUCTION

The development of molecular assemblies that mimic the characteristics of photosynthetic systems is central to the realization of solar fuel technologies. Using natural photosynthesis as a guide, artificial photosynthetic assemblies must be able to perform multiple functions spanning light harvesting, charge separation, and charge transfer of the redox equivalents to catalytic sites that drive multielectron reactions such as water oxidation or CO_2 reduction.[1,2] Coupling of light harvesting to charge separation has been successfully demonstrated in a number of solution phase systems employing a broad range of sensitizers.[3−5] Although these molecular systems elegantly demonstrate proof-of-concept principles regarding the photophysical mechanisms of directional energy flow, they are typically limited to a single or small group of chromophores and are difficult to synthesize, limiting their scalability to practical solar energy conversion applications. Multichromophore light harvesting assemblies based on polymers,[6−8] dendrimers,[9] and peptides[10] are less challenging to synthesize and thus provide a potentially scalable architecture, but only a few examples exist in which multiple functions (e.g., light harvesting, energy transport, charge separation) are incorporated into a single assembly.[10,11]

We previously reported the synthesis and photophysical study of a polyfluorene (PF)-based Ru(II) polypyridyl assembly (PF-Ru, Chart 1), where selective photoexcitation of the PF backbone gives rise to a kinetic competition between ultrafast energy and electron transfer to the pendant Ru(II) sites, producing a charge-separated state that persists for approximately 6 ns.[6] In the present investigation, we describe an approach that anchors a structurally similar PF-based assembly through ionic carboxylate-functionalized Ru(II) chromophores to metal oxide (TiO_2) films. When bound to TiO_2, the polymer exhibits multifunctional characteristics in which light absorption is coupled with energy transport and charge separation. Through pump−probe transient absorption methods the photophysical events are followed on time scales ranging from hundreds of femtoseconds to hundreds of microseconds. Photoexcitation of one of the Ru(II) complexes is followed by energy transport through site-to-site hopping to the interface, where electrons inject (i.e., charge separation) into the TiO_2. Hole transfer from the oxidized Ru complex to the PF backbone regenerates the chromophore at the interface on the picosecond time scale. The holes that reside on the PF

Received: November 12, 2014
Published: November 17, 2014

dx.doi.org/10.1021/jp5113558 | J. Phys. Chem. C 2014, 118, 28535−28541

Chart 1. Structure of Model-Ru-A, PF-Ru, and PF-Ru-A

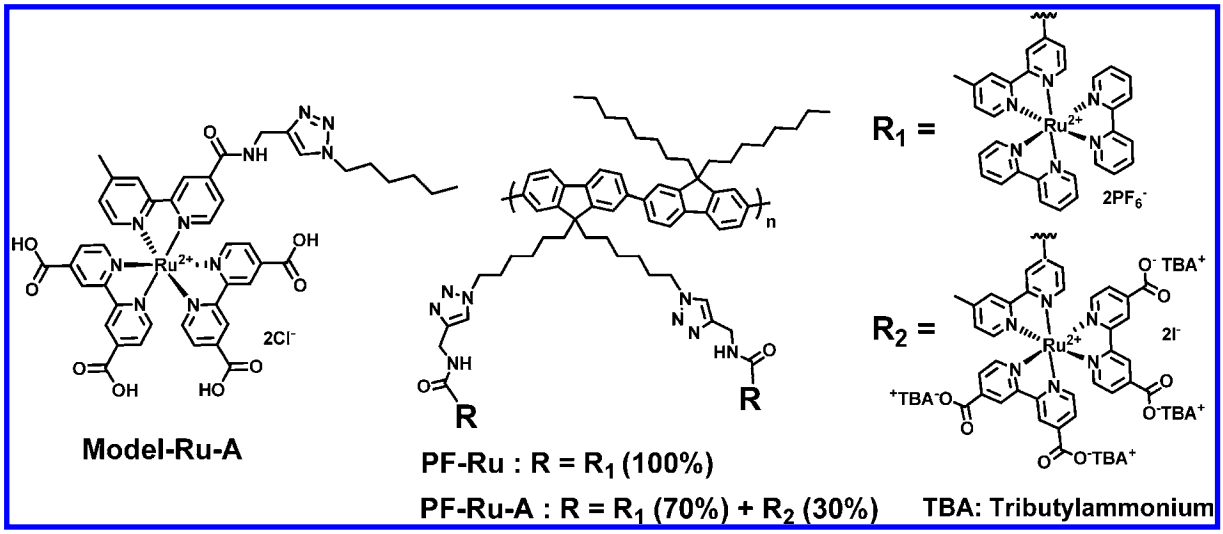

backbone are stable for >100 μs, implying that the PF serves not only as a structural scaffold but also as a functional element that can transport and potentially store multiple oxidative equivalents, for consumption by relatively slow catalytic cycles.

EXPERIMENTAL SECTION

Materials. The required materials, i.e., 4,4′-dimethyl-2,2′-bipyridyl, selenium dioxide, silver nitrate, potassium dichromate, potassium hydroxide, *N*,*N*′-dicyclohexylcarbodiimide (DCC), *N*-hydroxysuccinimide (NHS), sodium azide, potassium carbonate, potassium acetate, 1,6-dibromohexane, 1-bromohexane, 1-bromooctane, fluorene, tetrabutylammonium bromide, tributylamine, 1,8-diazabicyclo[5.4.0]undec-7-ene (DBU), sodium ascorbate, 4-(dimethylamino)pyridine (DMAP), *N*-bromosuccinimide, copper(I) bromide (CuBr, 99.999%), hexafluorophosphoric acid solution (~55 wt % in H_2O), hydrochloride acid (37% in water), tetrabutylammonium hydroxide solution (~40 wt % in H_2O), and *N*,*N*,*N*′,*N*″,*N*″-pentamethyldiethylenetriamine (PMDETA), were purchased from Sigma-Aldrich. Ammonium hexafluorophosphate (NH_4PF_6), ruthenium(III) chloride hydrate, and *cis*-bis(2,2′-bipyridine)dichlororuthenium(II) dihydrate ($Ru(bpy)_2Cl_2 \cdot 2H_2O$) were purchased from Alfa Aesar. Tetrakis-(triphenylphosphine)palladium and dichloro[1,1′-bis-(diphenylphosphino)ferrocene]palladium(II) dichloromethane adduct ($Pd(dppf)Cl_2$) were purchased from STREM Chemicals, Inc. All the chemicals were used as received unless otherwise indicated. Silica gel or alumina gel (reactivity grade I) was used for column chromatography. Dry solvents were obtained from a MBRAUN MB-SPS dry solvent system or purified using standard methods.[12] Solvents or liquid reagents for the use in a glovebox were also degassed using at least three freeze−pump−thaw cycles.

Synthesis of the Model-Ru-A and Polymer Assemblies PF-Ru-A. Synthesis details and characterization data for the new materials Model-Ru-A and PF-Ru-A are provided in the Supporting Information.

Fabrication of Dye Sensitized Solar Cells (DSSCs). The DSSCs were fabricated and modified following the literature.[13,14] Briefly, the TiO_2 paste was doctor-bladed onto a clean FTO glass slide followed by sintering at 500 °C for 30 min with 1 °C of the heating and cooling rate. The TiO_2 layer thickness was approximately 12−13 μm as measured by SEM. After cooling down to 80 °C, the annealed TiO_2 films were then dipped into the PF-Ru-A solution in a 1:2 (v/v) mixture of acetonitrile:methanol for 48 h. The PF-Ru-A//TiO_2 active cell area was controlled as 0.18 cm^2 to allow for consistent measurements of IPCE and *J*−*V* characteristics. A Pt counter electrode was prepared by spinning 0.01 M H_2PtCl_6 in isopropyl alcohol on FTO substrates with two holes created using a drill and by sintering 450 °C for 30 min. A Surlyn (25 μm, Solaronix) film as a spacer was sandwiched and fixed together at ~80 °C between PF-Ru-A//TiO_2 photoanode and a Pt counter electrode. Finally, an electrolyte solution containing 0.05 M I_2 and 0.1 M LiI, 0.5 M 4-*tert*-butylpyridine, and 0.6 M 1-methyl-3-*n*-propylimidazolium iodide in an anhydrous nitrite solution was injected into two holes on the Pt counter electrode side.

The current−voltage characteristics of the cells were measured with a Keithley 2400 source meter under AM1.5 (100 mW/cm^2) solar simulator. For IPCE measurements, the cells were illuminated by monochromatic light from an Oriel Cornerstone spectrometer, and the current response under short circuit conditions was recorded at 10 nm intervals using a Keithley 2400 source meter.

Characterization Methods. NMR spectra were measured on a Gemini-300 FT-NMR, a VXR 300 FT-NMR, or a Mercury-300 FT-NMR. High-resolution mass spectrometry was performed on a Bruker APEX II 4.7 T Fourier transform ion cyclotron resonance mass spectrometer (Bruker Daltonics, Billerica, MA) or a Finnigan LCQ-quadrupole ion trap (Thermo Finnigan, San Jose, CA). The ATR-FTIR spectra were obtained with a PerkinElmer Spectrum One ATR-FTIR spectrometer. The spectra were collected for 128 scans at a resolution of 4 cm^{-1}. A Hitachi H-7000 TEM was operated at an accelerating voltage of 100 kV to monitor the morphology of PF-Ru-A anchored TiO_2 particles. Analysis of SEM was performed using a Hitachi S-4000 with an accelerating voltage of 10 kV, and additional carbon conductive layers were coated on both bare TiO_2 and PF-Ru-A//TiO_2 films.

Transient Absorption Measurements. Transient absorption measurements were performed using a home-built transient absorption spectrometer. The spectrometer is based on a commercially available ultrafast laser system (Clark MXR

dx.doi.org/10.1021/jp5113558 | J. Phys. Chem. C 2014, 118, 28535−28541

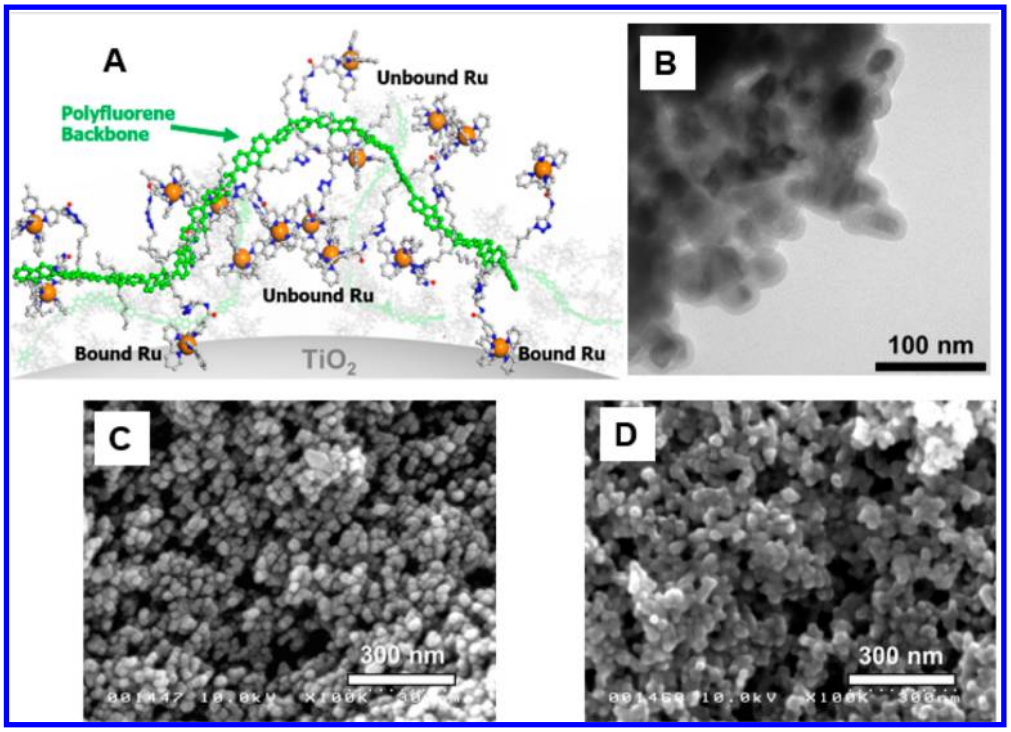

Figure 1. (A) Cartoon of PF-Ru-A anchored onto a TiO_2 surface. (B) TEM image of PF-Ru-A coated onto TiO_2 nanoparticles deposited on a carbon-coated grid. SEM images of as-prepared TiO_2 film (C) before and (D) after the immobilization of PF-Ru-A.

CPA-2210). The system consists of an erbium-doped fiber ring oscillator pumped by a solid-state fiber coupled laser diode operating at 980 nm and a chirped pulse Ti:sapphire regenerative amplifier pumped by a frequency-doubled, Q-switched Nd:YAG laser. Following pulse compression, the amplifier produces pulses centered at 775 nm with 120 fs fwhm duration at 1 kHz with pulse energies of 1.6 mJ/pulse. The 450 nm pump pulse was generated in a 2 mm BBO crystal by sum frequency generation of the 775 nm fundamental and the second harmonic of the 1070 nm signal from an optical parametric amplifier (Light Conversion TOPAS-C). The femtosecond probe pulse is generated by focusing 3 mW of the 775 nm amplifier output into a translating 5 mm thick CaF_2 window. The pump beam is focused onto the sample using a 300 mm lens, and the probe beam is focused and overlapped with a 250 mm spherical aluminum mirror. Spectra were collected on a shot-by-shot (1 kHz) basis over the range of 350−820 nm with a sensitivity of up to 0.1 mOD. The angle between the pump and probe polarization vectors was set to magic angle (~54.7°) to avoid polarization effects and ensure that only excited-state population dynamics were being monitored, and the sample was raster scanned to provide for a fresh sample between laser pulses. Following data collection, the frequency chirp in the probe pulse was characterized using the optical Kerr response of liquid CCl_4 in a 2 mm cuvette in a polarization gating geometry. The spectra were chirp-corrected using a data processing program written in LabVIEW.

Sub-nanosecond transient measurements were performed with an Ultrafast Systems EOS spectrometer, in which the probe pulse is generated by continuum generation from a photonic crystal fiber and detected by a fiber-optic coupled multichannel spectrometer with a CMOS sensor. The pump−probe delay is electronically controlled. The kinetic window ranges from 500 ps to 400 μs, and the time resolution of the instrument is around 500 ps, dictated by the width of the probe pulse and the timing electronics.

For transient absorption sample preparation, thin films of TiO_2 deposited on FTO glass were soaked for 48 h in a solution containing the sensitizer dissolved in a 1:2 (v/v) mixture of acetonitrile:methanol and were placed in a homemade 1 cm quartz cuvette at a 45° angle relative to the front face of the cuvette. All transient absorption experiments were performed with the sensitized films immersed in argon-saturated solutions of 100 mM $LiClO_4$ dissolved in acetonitrile and were raster scanned to prevent photodegradation of the samples.

Injection yield calculations were determined by comparing the intensity of the 385 nm $bpy^{\bullet-}$ absorption to the 450 nm ground state bleach. The maximum absorbance at 385 nm occurs when Φ_{inj} = 0%, which is observed from the transient absorption spectrum on ZrO_2, where injection is not possible due to the location of the conduction band edge. The minimum absorbance at 385 nm occurs when Φ_{inj} = 100%, in which the transient absorption spectrum represents Ru(III) on TiO_2. This is approximated as the inverse of the ground state absorption spectrum, normalized to the Ru(II) bleach. By comparing the amplitude of the 385 nm band with respect to these two limits, we can estimate Φ_{inj} as a function of pump−probe delay times.

Transient Absorption Kinetics Fitting Parameters. The fsTA kinetics traces at 385 nm were fit to a biexponential function with an *x*- and *y*-offset as implemented in Origin 9.0. The instrument response function (IRF) at 385 nm from the cross-correlation determined the earliest time point in the fitting function. The fitting function was minimized using the Levenberg−Marquardt method until a reduced χ^2 value of $1e^{-9}$ was achieved.

Molecular Dynamics Simulations. The polymer structures for the MD simulations were constructed using the Materials Studio suite (Accelrys Software, Inc., San Diego,

dx.doi.org/10.1021/jp5113558 | J. Phys. Chem. C 2014, 118, 28535−28541

2011). The ground-state geometry of the monomer was optimized using the B3LYP DFT functional and the LANL2DZ basis set, as implemented in Gaussian09 version 09a02.[15] After optimizing the gas-phase monomer structures, the homopolymer was constructed in Materials Studio. The gas-phase geometries of the polymers were then optimized and annealed with atomic charges (NPA) obtained from the Gaussian09 QM calculations. The annealing step consisted of five temperature cycles using the universal force field with the temperature ranging from 300 to 700 K in a time step of 1 fs, with five heating ramps per cycle and 200 dynamics steps per ramp for a total of 1 ns. The simulation cell consisted of an eight-repeat unit polymer, 32 PF_6^- (counterion), and 1180 CH_3CN molecules. The cell was then annealed using the same force field as the gas phase polymer with the temperature ranging from 300 to 1200 K in a time step of 1 fs with two heating ramps per cycle and 100 000 dynamics steps per ramp for a total of 800 ps. The annealed simulation cells were then used for molecular dynamics calculations with the canonical ensemble, NVT, at a temperature of 298 K controlled by the Nose thermostat with a Q-ratio of 0.01. Dynamics were calculated for a total of 1 ns in each polymer system, and snapshots were collected every 1 ps, giving a trajectory with 1000 snapshots for analysis for each annealed simulation cell.

RESULTS AND DISCUSSION

The chemical structures of the molecular systems studied are shown in Chart 1 which include the model Ru(II) complex (Model-Ru-A) and polymer assemblies PF-Ru and PF-Ru-A. PF-Ru was previously studied[6] in solution, leading us to design PF-Ru-A to allow anchoring of the assembly to metal oxide surfaces. Within the PF-Ru-A assembly, 30% of the pendant Ru(II) chromophores feature 4,4′-(dicarboxylate)-2,2-bipyridine ligands allowing for multiple surface binding points randomly positioned along the chain, leaving 70% of the unsubstituted Ru(II) 2,2-bipyridine chromophores to participate as antennas that transfer excited state energy to surface bound Ru(II) centers.[16] Figure 1A schematically illustrates the structure of PF-Ru-A obtained from solution molecular dynamics (MD) simulations. The MD simulation indicates that the polymer takes on an extended cylindrical conformation, with an effective diameter of approximately 6 nm. In the cartoon PF-Ru-A is shown anchored onto a TiO_2 surface (PF-Ru-A//TiO_2), with surface attachment facilitated by interaction of the polar carboxylate units with the oxide interface.

In the experiments, PF-Ru-A was adsorbed on mesoporous TiO_2 films by deposition from a 1:2 (v/v) mixture of acetonitrile:methanol solution for 48 h, followed by rinsing with MeOH and acetonitrile. The resulting surface was characterized by scanning electron microscopy (SEM), and the polymer modified TiO_2 particles were also imaged by transmission electron microscopy (TEM). Figure 1B shows a TEM image of PF-Ru-A//TiO_2 nanoparticles that were gently removed from a mesoporous film and transferred onto a TEM grid. The TEM image clearly shows an approximately 6 ± 2 nm coating of PF-Ru-A on the TiO_2 nanoparticles; note that this layer thickness is consistent with the diameter of the solution structure obtained from MD simulations, suggesting that the polymer adsorbs as a monolayer on the TiO_2 surface. SEM images of uncoated mesoporous TiO_2 films and PF-Ru-A//TiO_2 films are shown in Figure 1C,D. Analysis of the particle size distribution in the SEM image for the TiO_2 films after the deposition of PF-Ru-A revealed that the particles have an average size of roughly 26.2 ± 5.5 nm for the uncoated TiO_2 film and 31.9 ± 5.3 nm for PF-Ru-A//TiO_2 films, consistent with the PF-Ru-A layer thickness determined from TEM images. The binding of the PF-Ru-A to the TiO_2 nanoparticles indicated by the images presumably results from the interaction of the ionic carboxylate groups from multiple complexes per chain with the TiO_2 surface.[17]

The photoelectrochemical response of the PF-Ru-A//TiO_2 films was tested in a standard dye-sensitized solar cell (DSSC) configuration. Figure 2 shows that the photocurrent action

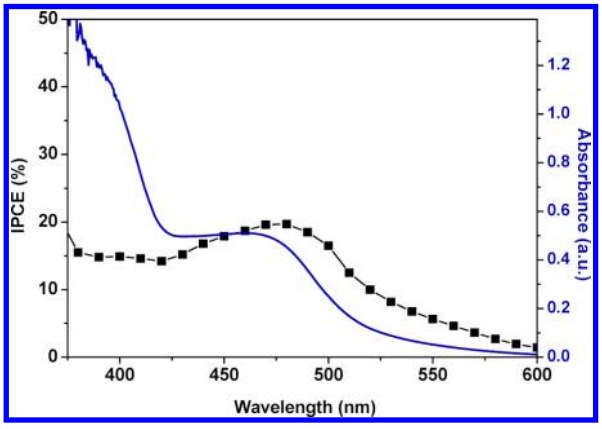

Figure 2. Incident photon to current efficiency (IPCE) spectra of a photoelectrochemical cell based on a PF-Ru-A//TiO_2 photoanode (black solid line with squares). UV−vis absorption spectrum of a PF-Ru-A//TiO_2 photoanode (blue solid curve) for comparison with IPCE plot. Note that the absorption increase for λ < 425 nm is due to onset of the PF backbone absorption.

spectrum (IPCE) of the PF-Ru-A sensitized solar cell exhibits a peak IPCE value of ∼20% at 480 nm. Importantly, the most pronounced band seen in the photocurrent spectrum corresponds to the metal-to-ligand charge transfer (MLCT) absorption of the Ru(II) chromophores. A feature corresponding to absorption of the PF backbone (λ < 425 nm) is weaker than expected in the photocurrent spectrum, indicating that excitations on the polymer are less efficient in charge injection compared to excitations on the Ru chromophores.[18] In these polymer assemblies, PF excitation decays through competitive PF* to Ru(II) energy and charge transfer pathways.[6]

Energy transfer from PF* to Ru(II)* should give the same photocurrent (on a per absorbed photon basis) as direct photoexcitation of a surface bound Ru(II) unit. On the other hand, deactivation via PF* to Ru(II) charge transfer will likely produce little or no photocurrent due to the kinetic competition between transport of the charge between unbound complexes to the surface for charge injection and the rapid charge recombination time (∼6 ns). The reduced photocurrent efficiency observed for PF excitation could indicate that on the TiO_2 surface charge separation/recombination is the dominant decay pathway. The PF-Ru-A//TiO_2 cell exhibited a peak absorbed photon-to-current efficiency (APCE = IPCE/[1 − T], where T = transmittance) value of ∼30% at 480 nm. Under 100 mW, AM 1.5 simulated solar illumination the performance of the PF-Ru-A//TiO_2 DSSC exhibited a photocurrent density−photovoltage (J−V) curve as shown in Figure S4, with an open-circuit voltage of V_{oc} = 0.54 V, short-circuit current density of J_{sc} = 1.31 mA/cm^2, fill factor of FF = 0.59, and overall power conversion efficiency of η = 0.43%.

dx.doi.org/10.1021/jp5113558 | J. Phys. Chem. C 2014, 118, 28535−28541

Transient absorption measurements performed on Model-Ru-A//TiO_2 and PF-Ru-A//TiO_2 films reveal a cascading series of energy and electron transfer events that occur following photoexcitation, as illustrated in Scheme 1. Photoexcitation of a surface-bound (proximal) Ru(II) chromophore (1b) results in rapid electron injection into TiO_2 (3), followed by the transfer of the hole on the oxidized Ru(III) complex to the PF backbone (4). Excitation of a Ru(II) chromophore that is distal with respect to the interface (1a) can lead to multiple Ru* → Ru energy hopping events (2). Transport of the energy to surface bound chromophores is followed by electron injection (3) and hole transfer to the polymer (4). On longer time scales, back electron transfer between Ru(III) and $TiO_2(e^-)$ (5a) or charge recombination between PF^+ and $TiO_2(e^-)$ (5b) give the original ground state Ru(II) species.

Scheme 1. Schematic Representation of Photophysical Events of PF-Ru-A on the Surface of TiO_2[a]

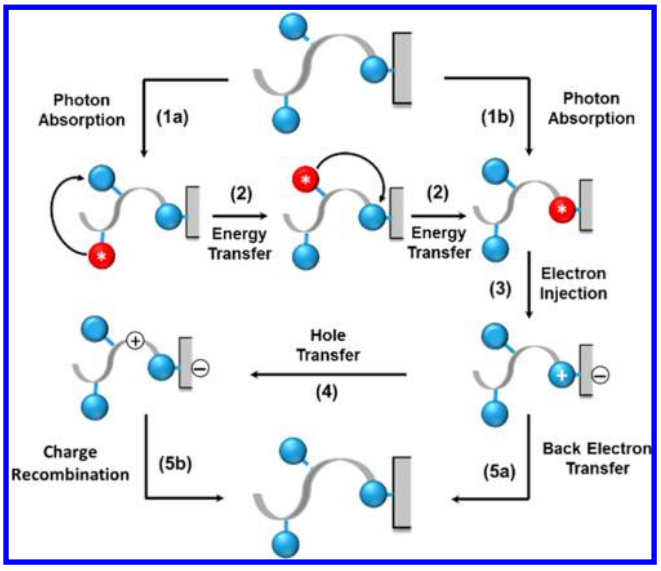

[a]Balls represent $Ru(L)_3^{2+}$ chromophores, and the gray ribbon represents the poly(fluorene) backbone.

The electron injection process (3) is monitored by fs−ps transient absorption on the Model-Ru-A//TiO_2 film. Spectra acquired shortly after 450 nm excitation of the Model-Ru-A//TiO_2 film (Figure 3A) show the characteristic $\pi \rightarrow \pi^*$ absorption at 385 nm of the reduced polypyridyl radical anion ($bpy^{\bullet-}$) along with a prominent ground-state bleach at 450 nm and a ligand-to-metal charge transfer (LMCT) and $bpy^{\bullet-}$ band that extends to the red of 500 nm.[19] Loss of the $bpy^{\bullet-}$ absorption at 385 nm without loss of the ground state bleach at 450 nm is the spectral signature of electron injection into the TiO_2. By monitoring the loss of the 385 nm excited state absorption (Figure 3B), the decay is described well by fast (τ_1 = 60 ps) and slow (τ_2 = 500 ps) components. Photoinduced electron injection has been shown to be a multiexponential process, owing to the intrinsic heterogeneity and dynamic relaxation processes following excitation.[20,21] These slower decay components most likely reflect electron injection from a thermalized ^{3}MLCT excited state, as reported for other Ru(II) dyes.[20] The presence of multiple kinetic components has been observed for other related sensitizers and arises from a number of factors, including the dye-binding motifs, electronic coupling, and overlap of the dye donor levels with the TiO_2 acceptor states.[22−24] Furthermore, based on the analysis of the transient spectra,[25] there is negligible ultrafast (τ < 200 fs) electron injection in this complex, and by 1.4 ns the overall injection yield is 45%.[26]

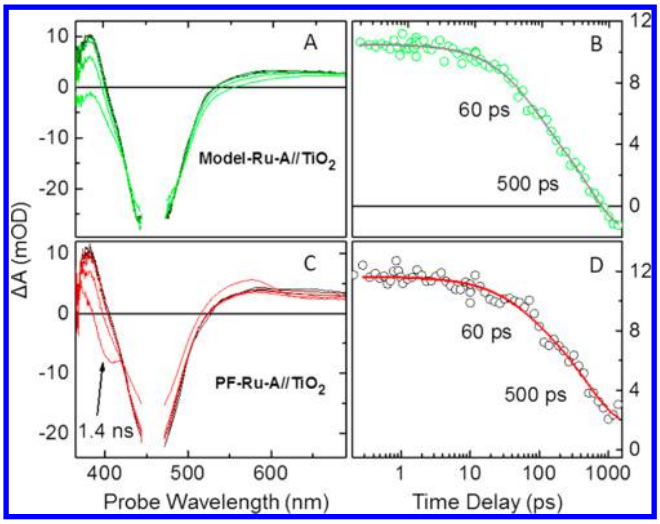

Figure 3. (A) Transient absorption spectra following 450 nm laser excitation for the Model-Ru-A complex on TiO_2 at 0.25, 1, 5, 10, 100, and 1400 ps. (B) Model-Ru-A//TiO_2 kinetics trace at 385 nm. (C) Transient absorption spectra of PF-Ru-A//TiO_2 at 0.25, 1, 5, 10, 100, and 1400 ps. (D) PF-Ru-A//TiO_2 kinetics trace at 385 nm. The films were immersed in argon-saturated acetonitrile with 0.1 M $LiClO_4$.

Photoexcitation of the PF-Ru-A//TiO_2 film at 450 nm gives rise to similar spectral features as seen for the Model-Ru-A//TiO_2 film at early times (Figure 3C). The intensity of the 385 nm absorption decays with time components that are similar to the Model-Ru-A complex (τ_1 = 60 ps and τ_2 = 500 ps) (Figure 3D), but the overall injection yield is significantly lower based on inspection of the transient spectra.[25] In addition, the transient spectra for the PF-Ru-A//TiO_2 assembly show additional bleach and absorption features at 400 and 580 nm, respectively (Figure 3C), and a concomitant loss of the MLCT ground state bleach at 450 nm. The 400 nm bleach and the 580 nm absorption are both attributed to oxidized PF polymer (PF^+) on the basis of spectroelectrochemical observations.[6] The absence of these two features in the transient spectra for PF-Ru-A//ZrO_2 (Figure S5) indicates that formation of PF^+ is a consequence of charge injection, most likely due to hole transfer from Ru(III), produced by charge injection, to the PF backbone (Scheme 1, step 4). Furthermore, the loss of the $bpy^{\bullet-}$ absorption at 385 nm occurs simultaneously with appearance of the PF^+ feature at 400 nm, suggesting that hole transfer takes place on a time scale that is short compared to the longer injection components.

The spectral features associated with the formation of PF^+ at 400 and 580 nm become increasingly pronounced on longer time scales, as seen in Figure 4A,C. Their continued growth during the first 200−300 ns is consistent with triplet−triplet energy transport from unbound Ru(II) complexes through site-to-site hopping to a chromophore bound to the TiO_2 surface, which then undergoes electron injection and hole localization on the PF (Scheme 1, steps 2 and 3). Thus, the time scale associated with the growth of the PF^+ features at 400 and 580 nm reflects the total time needed for the Ru* created by photoexcitation to reach the interface, which in turn depends upon the Ru* → Ru hopping time as well as the number of

dx.doi.org/10.1021/jp5113558 | J. Phys. Chem. C 2014, 118, 28535−28541

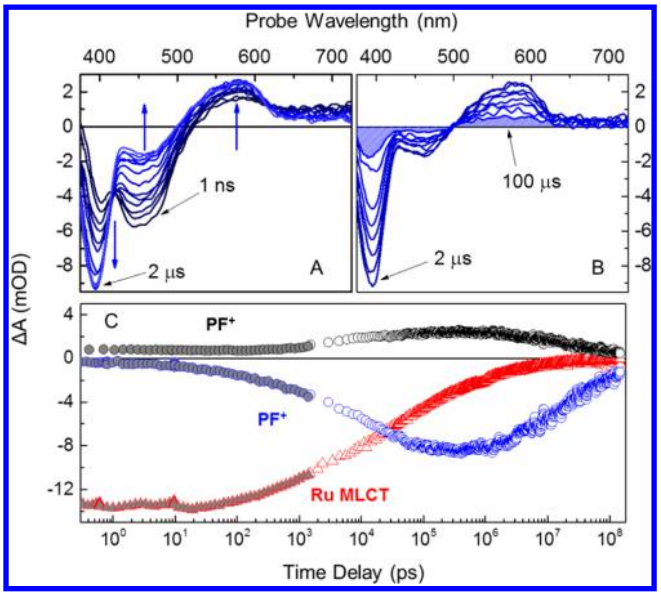

Figure 4. (A) Nanosecond transient absorption spectra of PF-Ru-A//TiO_2 films following excitation at 450 nm from 1 ns to 2 μs. (B) Nanosecond transient absorption spectra of PF-Ru-A//TiO_2 films from 2 to 100 μs. The shaded region is the spectrum at 100 μs. (C) Kinetics traces for PF-Ru-A//TiO_2 films at probe wavelengths 400 nm (blue), 485 nm (red), and 580 nm (black) from 250 fs to 150 μs following 450 nm excitation. The gray-filled points represent the femtosecond and picosecond kinetic traces. The films were immersed in argon-saturated acetonitrile with 0.1 M $LiClO_4$.

hops. Work on a related polymer assembly[27−29] suggests that the Ru* → Ru hopping time is <10 ns. Thus, the growth of PF^+ over 200−300 ns implies that some Ru(II)* excited states may make as many as 20−30 hops prior to charge injection, underscoring the antenna-like nature of the PF-Ru-A polymer assembly. The fraction of unbound Ru(II)* that reach the interface (F_s) can be estimated from the APCE efficiency (η_{APCE}) and the injection efficiency (η_{inj}), i.e., where f_B and f_U are the fractions of complexes that are bound and unbound to the surface, respectively. Using an APCE efficiency of 30% and an injection efficiency of 45%, we estimate (to a lower limit) that approximately 50% of the photoexcitations on unbound complexes are eventually transported to the surface where they can undergo electron injection.

$$F_s = \left(\frac{\eta_{APCE}}{\eta_{inj}} - f_B\right)\frac{1}{f_U}$$

By 200−300 ns after photoexcitation, the transient spectrum contains both the prominent features associated with the PF^+ as well as a significant Ru(II) bleach at 450 nm. Since hole transfer to form the positive polaron repopulates the Ru(II) ground state, the bleach must arise from Ru(III) complexes that have not undergone hole transfer or Ru(II)* excited states that remain. Although it is difficult to distinguish between these two contributions, the rapid hole transfer time would suggest that it is the Ru(II)* that is responsible for the bleach.

Furthermore, the Ru(II) ground state bleach decays before the PF^+ features (Figure 4B,C), indicating that the transient spectrum observed at the longest times arises almost entirely from the positive polaron, PF^+. A small population of Ru(III) still exists at 150 μs, most likely a result of the similar oxidation potentials for PF and non-carboxylated Ru(II) chromophores, leading to an equilibrium between the hole residing on the polymer backbone and the pendant chromophores. The charge-separated state decays through recombination of the injected electron in the TiO_2 with holes on the PF backbone (Scheme 1, 5b). Its lifetime (~150 μs) is significantly longer than that of Model-Ru-A//TiO_2 (Figure S6), consistent with a greater separation between the PF positive polaron and the surface.

CONCLUSION

PF-Ru chromophores functionalized with a small fraction of ionic carboxylate moieties have been prepared by "click" chemistry to attach the mixture of Ru(II) polypyridyl complexes and ester-containing Ru(II) polypyridyl complexes, following the deprotection step to form ionic carboxylate functionalized Ru(II) polypyridyl complexes. With the successful synthesis of PF-Ru-A, the polymer-based chromophores were anchored to TiO_2 films. The solar characteristics demonstrate TiO_2 surface anchoring and light harvesting ability when applied in solar photoelectrochemical cells. These light harvesting mechanisms were studied with femtosecond pump−probe spectroscopy, where direct excitation of the Ru(II) chromophores leads to rapid and efficient electron injection for chromophores directly bound to the TiO_2 surface. This event is followed by ultrafast hole transfer to the polyfluorene chain, thereby facilitating repopulation of the ground state Ru(II) species and avoiding deleterious charge recombination processes. The pendant Ru(II) chromophores undergo energy transfer to surface-bound chromophores on the nanosecond time scale, where electron injection can precede hole transfer to the polymer backbone. Charge recombination for the Ru(II) chromophores occurs on the microsecond time scale, where injected electrons recombine with oxidized chromophores that have not undergone hole transfer, whereas charge recombination involving the oxidized polymer occurs on longer time scales. This study reveals the promise for coupling polymeric assemblies to a semiconductor interface for light harvesting, charge separation, and transient charge storage. Work in progress seeks to include oxidation catalyst centers into the assemblies with the objective of accomplishing water oxidation at the photoanode of a dye-sensitized photoelectrosynthesis cell.

ASSOCIATED CONTENT

Supporting Information

Experimental procedures, ATR-FTIR, TEM, AFM, $J-V$ curve, absorption and emission spectra of PF-Ru-A//TiO_2 films, and transient absorption spectra of PF-Ru-A//ZrO_2 results. This material is available free of charge via the Internet at http://pubs.acs.org.

AUTHOR INFORMATION

Corresponding Authors

*E-mail kschanze@chem.ufl.edu (K.S.S.).
*E-mail john_papanikolas@unc.edu (J.M.P.).

Author Contributions

G.L. and Z.A.M. contributed equally.

Notes

The authors declare no competing financial interest.

ACKNOWLEDGMENTS

This material is based on work supported as part of the UNC EFRC: Solar Fuels and Next Generation Photovoltaics, an

Energy Frontier Research Center funded by the U.S. Department of Energy, Office of Science, Office of Basic Energy Sciences, under Award DE-SC0001011. We also thank Karen L. Kelly in the Interdisciplinary Center for Biotechnology Research (ICBR) Electron Microscopy and Bioimaging Laboratory at University of Florida for help with the TEM and SEM.

REFERENCES

(1) Ashford, D. L.; Song, W.; Concepcion, J. J.; Glasson, C. R. K.; Brennaman, M. K.; Norris, M. R.; Fang, Z.; Templeton, J. L.; Meyer, T. J. Photoinduced Electron Transfer in a Chromophore−Catalyst Assembly Anchored to TiO_2. *J. Am. Chem. Soc.* **2012**, *134*, 19189−19198.

(2) Song, W.; Glasson, C. R. K.; Luo, H.; Hanson, K.; Brennaman, M. K.; Concepcion, J. J.; Meyer, T. J. Photoinduced Stepwise Oxidative Activation of a Chromophore−Catalyst Assembly on TiO_2. *J. Phys. Chem. Lett.* **2011**, *2*, 1808−1813.

(3) Tomizaki, K.; Loewe, R. S.; Kirmaier, C.; Schwartz, J. K.; Retsek, J. L.; Bocian, D. F.; Holten, D.; Lindsey, J. S. Synthesis and Photophysical Properties of Light-Harvesting Arrays Composed of a Porphyrin Bearing Multiple Perylene-Monoimide Accessory Pigments. *J. Org. Chem.* **2002**, *67*, 6519−6534.

(4) Gust, D.; Moore, T. A.; Moore, A. L. Mimicking Photosynthetic Solar Energy Transduction. *Acc. Chem. Res.* **2001**, *34*, 40−48.

(5) Wasielewski, M. R. Photoinduced Electron Transfer in Supramolecular Systems for Artificial Photosynthesis. *Chem. Rev.* **1992**, *92*, 435−461.

(6) Wang, L.; Puodziukynaite, E.; Vary, R. P.; Grumstrup, E. M.; Walczak, R. M.; Zolotarskaya, O. Y.; Schanze, K. S.; Reynolds, J. R.; Papanikolas, J. M. Competition between Ultrafast Energy Flow and Electron Transfer in a Ru(II)-Loaded Polyfluorene Light-Harvesting Polymer. *J. Phys. Chem. Lett.* **2012**, *3*, 2453−2457.

(7) Wang, L.; Puodziukynaite, E.; Grumstrup, E. M.; Brown, A. C.; Keinan, S.; Schanze, K. S.; Reynolds, J. R.; Papanikolas, J. M. Ultrafast Formation of a Long-Lived Charge-Separated State in a Ru-Loaded Poly(3-hexylthiophene) Light-Harvesting Polymer. *J. Phys. Chem. Lett.* **2013**, *4*, 2269−2273.

(8) Chen, Z.; Grumstrup, E. M.; Gilligan, A. T.; Papanikolas, J. M.; Schanze, K. S. Light-Harvesting Polymers: Ultrafast Energy Transfer in Polystyrene-Based Arrays of π-Conjugated Chromophores. *J. Phys. Chem. B* **2014**, *118*, 372−378.

(9) Adronov, A.; Gilat, S. L.; Frechet, J. M. J.; Ohta, K.; Neuwahl, F. V. R.; Fleming, G. R. Light Harvesting and Energy Transfer in Laser-Dye-Labeled Poly(Aryl Ether) Dendrimers. *J. Am. Chem. Soc.* **2000**, *122*, 1175−1185.

(10) Ma, D.; Bettis, S. E.; Hanson, K.; Minakova, M.; Alibabaei, L.; Fondrie, W.; Ryan, D. M.; Papoian, G. A.; Meyer, T. J.; Waters, M. L.; Papanikolas, J. M. Interfacial Energy Conversion in Ru-II Polypyridyl-Derivatized Oligoproline Assemblies on TiO_2. *J. Am. Chem. Soc.* **2013**, *135*, 5250−5253.

(11) Sykora, M.; Maxwell, K. A.; DeSimone, J. M.; Meyer, T. J. Mimicking the Antenna-Electron Transfer Properties of Photosynthesis. *Proc. Natl. Acad. Sci. U. S. A.* **2000**, *97*, 7687−7691.

(12) Armarego, W. L. F.; Chai, C. *Purification of Laboratory Chemicals*, 5th ed.; Butterworth-Heinemann: Oxford, UK, 2003.

(13) Fang, Z.; Eshbaugh, A. A.; Schanze, K. S. Low-Bandgap Donor−Acceptor Conjugated Polymer Sensitizers for Dye-Sensitized Solar Cells. *J. Am. Chem. Soc.* **2011**, *133*, 3063−3069.

(14) Lee, Y.-G.; Park, S.; Cho, W.; Son, T.; Sudhagar, P.; Jung, J. H.; Wooh, S.; Char, K.; Kang, Y. S. Effective Passivation of Nanostructured TiO_2 Interfaces with Peg-Based Oligomeric Coadsorbents to Improve the Performance of Dye-Sensitized Solar Cells. *J. Phys. Chem. C* **2012**, *116*, 6770−6777.

(15) Frisch, M. J.; et al. *Gaussian 09, Revision C.01*; Gaussian, Inc.: Wallingford, CT, 2009.

(16) The 30% loading of the bis(dicarboxy)bpy Ru(II) on the polyfluorene chain reflects the stoichiometry in the click reaction used to attach the acetylene functionalized Ru(II) chromophores to the azide functionalized polyfluorene.

(17) Comparison of ATR-IR spectra of PF-Ru-A and PF-Ru-A//TiO_2 (Figure S1) supports the premise that the surface bonding is via the carboxylate groups.

(18) The absorption of the polyfluorene backbone has a band maximum at 393 nm; see absorption spectrum in Supporting Information, Figure S5.

(19) Rack, J. J. Electron Transfer Triggered Sulfoxide Isomerization in Ruthenium and Osmium Complexes. *Coord. Chem. Rev.* **2009**, *253*, 78−85.

(20) Koops, S. E.; O'Regan, B. C.; Barnes, P. R. F.; Durrant, J. R. Parameters Influencing the Efficiency of Electron Injection in Dye-Sensitized Solar Cells. *J. Am. Chem. Soc.* **2009**, *131*, 4808−4818.

(21) Juozapavicius, M.; Kaucikas, M.; van Thor, J. J.; O'Regan, B. C. Observation of Multiexponential Pico- to Subnanosecond Electron Injection in Optimized Dye-Sensitized Solar Cells with Visible-Pump Mid-Infrared-Probe Transient Absorption Spectroscopy. *J. Phys. Chem. C* **2013**, *117*, 116−123.

(22) Giokas, P. G.; Miller, S. A.; Hanson, K.; Norris, M. R.; Glasson, C. R. K.; Concepcion, J. J.; Bettis, S. E.; Meyer, T. J.; Moran, A. M. Spectroscopy and Dynamics of Phosphonate-Derivatized Ruthenium Complexes on TiO_2. *J. Phys. Chem. C* **2013**, *117*, 812−824.

(23) Li, L. S.; Giokas, P. G.; Kanai, Y.; Moran, A. M. Modeling Time-Coincident Ultrafast Electron Transfer and Solvation Processes at Molecule-Semiconductor Interfaces. *J. Chem. Phys.* **2014**, *140*, 234109.

(24) Asbury, J. B.; Anderson, N. A.; Hao, E. C.; Ai, X.; Lian, T. Q. Parameters Affecting Electron Injection Dynamics from Ruthenium Dyes to Titanium Dioxide Nanocrystalline Thin Film. *J. Phys. Chem. B* **2003**, *107*, 7376−7386.

(25) Wang, L.; Ashford, D. L.; Thompson, D. W.; Meyer, T. J.; Papanikolas, J. M. Watching Photoactivation in a Ru(II) Chromophore−Catalyst Assembly on TiO_2 by Ultrafast Spectroscopy. *J. Phys. Chem. C* **2013**, *117*, 24250−24258.

(26) This injection yield is substantially lower than those observed for similar Ru(II) complexes on TiO_2. It is most likely a result of the chemical modification needed to attach the complex to the polymer, which could lead to low-energy MLCT excited states associated with the ancillary ligands that slow electron injection and diminish the overall injection yield.

(27) Fleming, C. N.; Maxwell, K. A.; DeSimone, J. M.; Meyer, T. J.; Papanikolas, J. M. Ultrafast Excited-State Energy Migration Dynamics in an Efficient Light-Harvesting Antenna Polymer Based on Ru(II) and Os(II) Polypyridyl Complexes. *J. Am. Chem. Soc.* **2001**, *123*, 10336−10347.

(28) Fleming, C. N.; Jang, P.; Meyer, T. J.; Papanikolas, J. M. Energy Migration Dynamics in a Ru(II)- and Os(II)-Based Antenna Polymer Embedded in a Disordered, Rigid Medium. *J. Phys. Chem. B* **2004**, *108*, 2205−2209.

(29) Fleming, C. N.; Brennaman, M. K.; Papanikolas, J. M.; Meyer, T. J. Efficient, Long-Range Energy Migration in Ru-II Polypyridyl Derivatized Polystyrenes in Rigid Media. Antennae for Artificial Photosynthesis. *Dalton Trans.* **2009**, 3903−3910.

THE JOURNAL OF PHYSICAL CHEMISTRY C

Article

pubs.acs.org/JPCC

Photophysical Characterization of a Helical Peptide Chromophore–Water Oxidation Catalyst Assembly on a Semiconductor Surface Using Ultrafast Spectroscopy

Stephanie E. Bettis, Derek M. Ryan, Melissa K. Gish, Leila Alibabaei, Thomas J. Meyer, Marcey L. Waters, and John M. Papanikolas*

Department of Chemistry, CB 3290, University of North Carolina, Chapel Hill, North Carolina 27599, United States

Supporting Information

ABSTRACT: We report a detailed kinetic analysis of ultrafast interfacial and intra-assembly electron transfer following excitation of an oligoproline scaffold functionalized by chemically linked light-harvesting chromophore $[Ru(pbpy)_2(bpy)]^{2+}$ (pbpy = 4,4′-$(PO_3H_2)_2$-2,2′-bipyridine, bpy = 2,2′-bipyridine) and water oxidation catalyst $[Ru(Mebimpy)(bpy)OH_2]^{2+}$ (Mebimpy = 2,6-bis(1-methylbenzimidazol-2-yl)pyridine). The oligoproline scaffold approach is appealing due to its modular nature and helical tertiary structure. They allow for the control of electron transfer distances in chromophore–catalyst assemblies for applications in dye-sensitized photoelectrosynthesis cells (DSPECs). The proline chromophore–catalyst assembly was loaded onto nanocrystalline TiO_2 with the helical structure of the oligoproline scaffold maintaining the controlled relative positions of the chromophore and catalyst. Ultrafast transient absorption spectroscopy was used to analyze the kinetics of the first photoactivation step for oxidation of water in the assembly. A global kinetic analysis of the transient absorption spectra reveals that photoinduced electron injection occurs in 18 ps and is followed by intra-assembly oxidative activation of the water oxidation catalyst on the hundreds of picoseconds time scale ($k_{ET} = 2.6 \times 10^9\ s^{-1}$; τ = 380 ps). The first photoactivation step in the water oxidation cycle of the chromophore–catalyst assembly anchored to TiO_2 is complete within 380 ps.

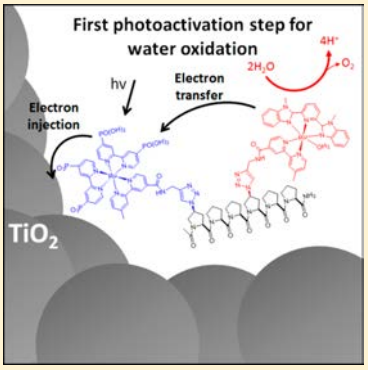

INTRODUCTION

Dye sensitized photoelectrosynthesis cells (DSPECs) provide a promising strategy for using sunlight to drive the conversion of water and carbon dioxide into chemical fuels.[1,2] Integral to the DSPEC approach is integration of molecular components for harvesting light, separating redox equivalents, and using them to drive the solar fuel half reactions. The functional elements have been demonstrated separately, but examples where all three have been integrated are rare.[3−11] We describe here the use of ultrafast spectroscopy to characterize the initial photoactivation step in a molecular assembly that couples a light-harvesting chromophore and water oxidation catalyst.

Water oxidation requires the transfer of four electrons and four protons with O−O bond formation, $2H_2O \rightarrow O_2 + 4H^+ + 4e^-$.[1] Significant progress has been made in the development of polypyridyl-based Ru(II)-aqua catalysts for water oxidation with mechanistic details established both in solution and on oxide surfaces (Scheme 1).[12−14] The initial activation step involves oxidation of $[Ru^{II}—OH_2]^{2+}$ to $[Ru^{III}—OH_2]^{3+}$ followed by proton loss to give $[Ru^{III}—OH]^{2+}$ above the pK_a of the coordinated water. Further oxidation results in e^-/H^+ loss to give $[Ru^{IV}═O]^{2+}$. Transfer of the third oxidative equivalent yields $[Ru^{V}═O]^{3+}$. It is active toward water oxidation by O—O bond formation and proton loss to give $[Ru^{III}—OOH]^{2+}$ in what is typically the rate limiting step.

Scheme 1. Illustration of the Water Oxidation Catalytic Cycle for Single-Site Ru^{II} Catalysts

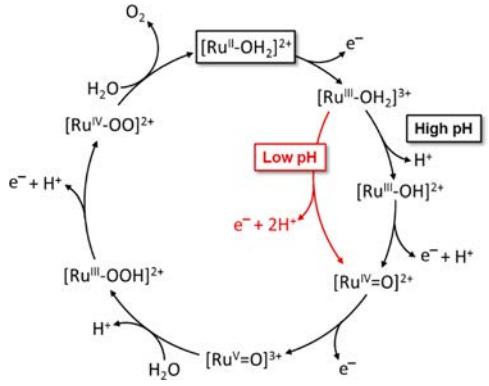

Transfer of the fourth oxidative equivalent occurs with H^+ loss to give $[Ru^{IV}—OO]^{2+}$, where O_2 replaced H_2O in a reductive substitution step to regenerate the initial catalyst $[Ru^{II}—OH_2]^{2+}$.

Received: October 28, 2013
Revised: March 4, 2014

   dx.doi.org/10.1021/jp410646u | J. Phys. Chem. C XXXX, XXX, XXX−XXX

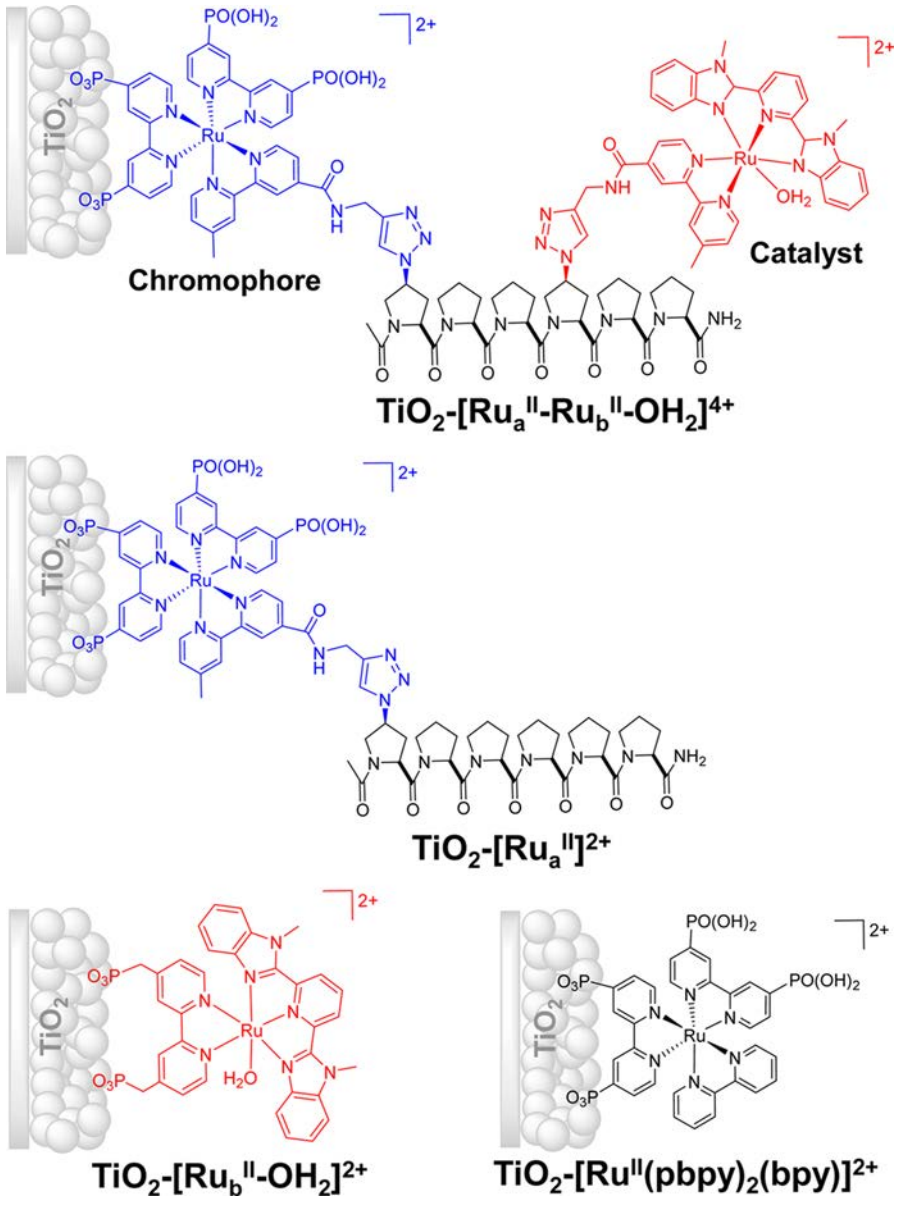

Figure 1. Illustration of the molecular structures of the assembly $[Ru_a^{II}–Ru_b^{II}–OH_2]^{4+}$, chromophore $[Ru_a^{II}]^{2+}$, catalyst $[Ru_b^{II}–OH_2]^{2+}$, and control chromophore $[Ru^{II}(pbpy)_2(bpy)]^{2+}$ on nanocrystalline TiO_2.

The DSPEC approach marries the excitation, electron transfer, and catalyst activation steps in surface-bound chromophore–catalyst assemblies[3−11] with the interfacial and electron transport properties of high band gap oxide semiconductors. A variety of chemical approaches have explored the design of chromophore–catalyst assemblies, but most require a unique synthetic approach for each new assembly.[3−11] In contrast, peptide scaffolds offer a flexible design motif, since step-by-step synthesis techniques can be used to control primary sequence and secondary structure as a way to control electron transfer flow and rates. In a previous report, we described an assembly consisting of two Ru^{II} complexes positioned along an oligoproline chain.[15] Molecular dynamics simulations suggested that folding of the peptide backbone brought the two complexes into close contact with a Ru–Ru interunit spacing of 13 Å. The double-chromophore assembly was anchored by chemical binding to TiO_2, and intra-assembly energy transfer and electron injection were characterized by ultrafast spectroscopic methods.

This paper extends that work to a functioning molecular assembly for water oxidation, $TiO_2–[Ru_a^{II}–Ru_b^{II}–OH_2]^{4+}$. It consists of a light-harvesting chromophore ($[Ru_a^{II}]^{2+}$ = $[Ru(pbpy)_2(L)]^{2+}$ (pbpy = 4,4′-$(PO_3H_2)_2$-2,2′-bipyridine, L = 4′-methyl-(2,2′-bipyridine)-4-propargyl amide)) and water oxidation catalyst ($[Ru_b^{II}–OH_2]^{2+}$ = $[Ru(Mebimpy)(L)OH_2]^{2+}$ (Mebimpy = 2,6-bis(1-methylbenzimidazol-2-yl)pyridine)) linked by a six-residue oligoproline scaffold, Figure 1. The chromophore is placed on the N-terminal residue (i) and the water oxidation catalyst on the fourth proline residue (i + 3).[16] In aqueous solution, the peptide chain adopts a left-handed PPII helical structure with three residues per turn, bringing the chromophore and catalyst on adjacent turns into close spatial proximity.

This paper focuses on the use of ultrafast spectroscopy to characterize the initial photoactivation step of this chromo-

dx.doi.org/10.1021/jp410646u | J. Phys. Chem. C XXXX, XXX, XXX–XXX

phore−catalyst assembly. Photoexcitation of the assembly on TiO_2, TiO_2−[Ru_a^{II}−Ru_b^{II}−OH_2]$^{4+}$, results in either excitation of the chromophore (Scheme 2, eq 1a) or the catalyst (eq 1b).

Scheme 2. Schematic Representation of the Events in TiO_2−[Ru_a^{II}−Ru_b^{II}−OH_2]$^{4+}$ upon Photoexcitation

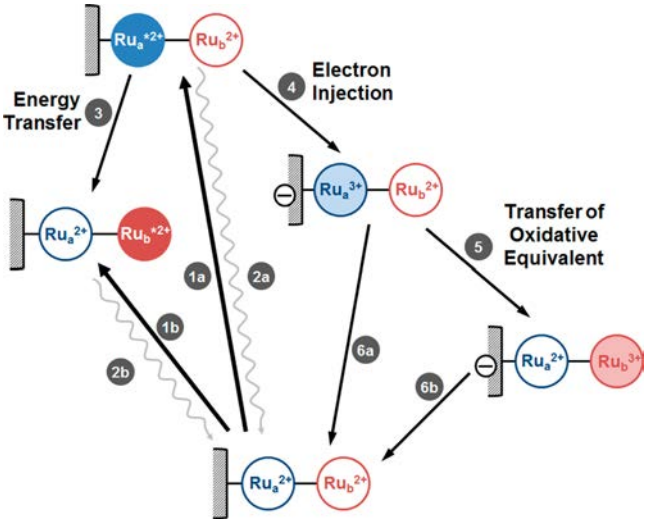

Chromophore excitation is followed by efficient electron injection

$$TiO_2-[Ru_a^{II}*-Ru_b^{II}-OH_2]^{4+} \rightarrow TiO_2(e^-)-[Ru_a^{III}-Ru_b^{II}-OH_2]^{5+} \quad (4)$$

in competition with energy transfer to the catalyst, resulting in the formation of oxidized chromophore at the surface. Once formed, transfer of the oxidative equivalent to the catalyst occurs by electron transfer from the catalyst to the oxidized chromophore

$$TiO_2(e^-)-[Ru_a^{III}-Ru_b^{II}-OH_2]^{5+} \rightarrow TiO_2(e^-)-[Ru_a^{II}-Ru_b^{III}-OH_2]^{5+} \quad (5)$$

returning the chromophore to its original oxidation state and completing the first of four steps in the water oxidation catalyst cycle. Energy transfer from photoexcited chromophore to the catalyst

$$TiO_2-[Ru_a^{II}*-Ru_b^{II}-OH_2]^{4+} \rightarrow TiO_2-[Ru_a^{II}-Ru_b^{II}*-OH_2]^{4+} \quad (3)$$

is also possible, and a potentially deleterious energy loss pathway; however, it is significantly slower than electron injection and does not interfere with injection.

Following injection, "recombination" by back electron transfer from the semiconductor surface

$$TiO_2(e^-)-[Ru_a^{II}-Ru_b^{III}-OH_2]^{5+} \rightarrow TiO_2-[Ru_a^{II}-Ru_b^{II}-OH_2]^{4+} \quad (6b)$$

returns the surface assembly to its initial state with the transiently stored oxidative equivalent lost as heat. Successful utilization of the interfacial injection/electron transfer schemes requires long recombination times or rapid removal of injected electrons from the semiconductor, both of which are being pursued experimentally.

EXPERIMENTAL SECTION

Sample Preparation. All samples were loaded onto nanocrystalline films of TiO_2 (1 μm thick) and ZrO_2 (3 μm thick) by soaking overnight in a 150 mM aqueous 0.1 M $HClO_4$ solution. The surface coverages for [Ru_a^{II}]$^{2+}$ and [Ru_a^{II}−Ru_b^{II}−OH_2]$^{4+}$ are nearly full with $\Gamma = 2.2 \times 10^{-8}$ and 1.7×10^{-8} mol/cm^2/μm, respectively, on TiO_2 and $\Gamma = 2.2 \times 10^{-8}$ and 1.5×10^{-8} mol/cm^2/μm, respectively, on ZrO_2.[17] The films were placed in a 1.0 cm cuvette at a 45° angle from the incident laser beam. All samples were in 0.1 M $HClO_4$ and purged with argon for >45 min just prior to data collection.

Instrumentation. Ground-state absorbance measurements were conducted with a Hewlett-Packard 8453 UV−vis−NIR absorption spectrophotometer. Steady-state emission (SSE) data were collected using an Edinburgh Instruments FLS920 equipped with a 450 W xenon lamp and photomultiplier tube (Hamamatsu 2658P). SSE data were collected using a bandwidth no larger than 4.0 nm and, once collected, were corrected for the emission spectrophotometer's spectral response. The FLS920 was also used for time-resolved measurements by the time-correlated single photon counting (TCSPC) technique with an instrument response of 2 ns, using a 444.2 nm diode laser (Edinburgh Instruments EPL-445, 73 ps fwhm pulse width) operated at 200 kHz. A 495 nm long pass color filter was used for emission experiments.

Femtosecond transient absorption measurements were done using a pump−probe technique based on a 1 kHz Ti:sapphire chirped pulse amplifier (Clark-MXR CPA-2001). The 420 nm pump pulse (100 nJ) was produced by sum frequency generation of 900 nm, the frequency doubled output from an Optical Parametric Amplifier (OPA), and a portion of the 775 nm regenerative amplifier beam. A white light continuum generated in a CaF_2 window was used as a probe pulse. The pump and probe polarizations were set to magic angle, and the two beams were focused to 150 μm spot size spatially overlapped at the sample. The probe beam was then collected and directed into a fiber optic coupled multichannel spectrometer with a CMOS sensor. The pump beam was chopped at 500 Hz with a mechanical chopper synchronized to the laser, and pump-induced changes in the white light continuum were measured on a pulse-to-pulse basis. The instrument has a sensitivity 1 mOD, and is capable of measuring transient absorption spectra from 360 to 750 nm with a time resolution of approximately 250 fs. Pump−probe transient absorption measurements on the ps to μs time scale were accomplished using the same pump pulse as the femtosecond instrument, but the probe pulse was generated by continuum generation in a diode-laser pumped photonic crystal fiber and electronically delayed relative to the pump pulse. The time resolution of the instrument is 500 ps dictated primarily by the timing electronics.

RESULTS AND DISCUSSION

We have used transient absorption spectroscopy, on time scales ranging from sub-picosecond to hundreds of microseconds, to characterize the initial photoactivation step in the water oxidation cycle of a chromophore−catalyst assembly anchored to TiO_2. In the subsections that follow, we address each of the dynamical processes involved in the initial photoactivation step.

Photoexcitation. Ground-state absorption spectra for the chromophore [Ru_a^{II}]$^{2+}$ and the catalyst [Ru_b^{II}−OH_2]$^{2+}$ anchored to TiO_2 and ZrO_2 are shown in Figure 2. Both

dx.doi.org/10.1021/jp410646u | J. Phys. Chem. C XXXX, XXX, XXX−XXX

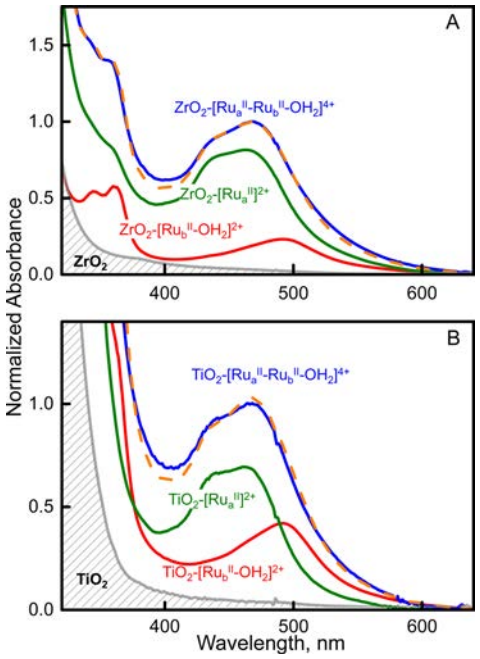

Figure 2. (A) Ground-state absorption of 3 μm ZrO_2 (gray), ZrO_2–$[Ru_a^{II}]^{2+}$ (green), ZrO_2–$[Ru_b^{II}$–$OH_2]^{2+}$ (red), ZrO_2–$[Ru_a^{II}$–Ru_b^{II}–$OH_2]^{4+}$ (blue), and sum of ZrO_2–$[Ru_a^{II}]^{2+}$ and ZrO_2–$[Ru_b^{II}$–$OH_2]^{2+}$ (dashed). (B) Ground-state absorption for 1 μm TiO_2 film (gray), TiO_2–$[Ru_a^{II}]^{2+}$ (green), TiO_2–$[Ru_b^{II}$–$OH_2]^{2+}$ (red), TiO_2–$[Ru_a^{II}$–Ru_b^{II}–$OH_2]^{4+}$ (blue), and the sum of TiO_2–$[Ru_a^{II}]^{2+}$ and TiO_2–$[Ru_b^{II}$–$OH_2]^{2+}$ (dashed). All film samples were in a quartz cuvette containing aqueous 0.1 M $HClO_4$, 25 °C.

complexes in the assembly exhibit singlet metal-to-ligand charge transfer (^{1}MLCT) bands centered between 400 and 500 nm, which is typical of Ru(II) polypyridyl complexes (Figure 2).[18] The absorption maximum for the catalyst (495 nm) appears at lower energy compared to the chromophore (465 nm), in large part due to greater π conjugation in the Mebimpy ligand.

The ground-state absorption centered at 470 nm of the assembly on ZrO_2 (ZrO_2–$[Ru_a^{II}$–Ru_b^{II}–$OH_2]^{4+}$) is the superposition of absorption spectra for the chromophore (ZrO_2–$[Ru_a^{II}]^{2+}$) and model catalyst (ZrO_2–$[Ru_b^{II}$–$OH_2]^{2+}$), consistent with weak interactions and essentially electronically isolated chromophores. The intensity of the catalyst absorption in the assembly on ZrO_2 is ~3.5 times smaller than the chromophore at their respective maxima even though the ratio of molar extinction coefficients, $\varepsilon_{[Rua]}/\varepsilon_{[Rub]}$, is only 1.3 times smaller.[17,19] This apparent decrease is consistent with samples partly converted to the Ru(IV) peroxide form of the assembly, $[Ru_a^{II}$–$Ru_b^{IV}(OO)]^{4+}$. On both ZrO_2 and TiO_2, equilibria are set up on the surfaces between the two forms, ZrO_2–$[Ru_a^{II}$–Ru_b^{II}–$OH_2]^{4+}$ + O_2 ⇄ ZrO_2–$[Ru_a^{II}$–$Ru_b^{IV}(OO)]^{4+}$ + H_2O, with the underlying details currently under investigation.

On the ZrO_2-loaded slide, ~40% of the assembly sites were converted into the weakly absorbing peroxide forms, $[Ru_b^{IV}$–$OO]^{2+}$, as assessed by ground-state absorption measurements. In the photophysical measurements, the peroxide forms behave dynamically as isolated ($[Ru_a^{II}*]^{2+}$) sites without noticeable perturbation or participation by the peroxide sites $[Ru_b^{II}(OO)^{2+}]$. A similar conversion occurs on TiO_2 films, but the extent of conversion to the peroxide depends on conditions, and in those samples, spectral comparisons show that ~20% of the catalysts were converted to the peroxide for the samples used. Since the Ru(IV) peroxide form in assemblies is only weakly absorbing in the visible, is not further oxidized by the chromophore, and is not involved in the photophysical properties of the assembly, it is a spectator to the photophysics studied here.

Because of the large degree of overlap in the absorption spectra, between chromophore and catalyst in $[Ru_a^{II}$–Ru_b^{II}–$OH_2]^{4+}$, selective excitation of the chromophore is not possible. On the basis of the relative intensities of the component ground-state spectra on TiO_2, we estimate that, at 420 nm, the excitation wavelength used in this work, 85% of the photons are absorbed by the chromophore and 15% by the catalyst.

Electron Injection. Transient absorption spectra observed 1 ps after photoexcitation for both TiO_2–$[Ru_a^{II}]^{2+}$ and TiO_2–$[Ru_a^{II}$–Ru_b^{II}–$OH_2]^{4+}$ are depicted in Figure 3. Both show

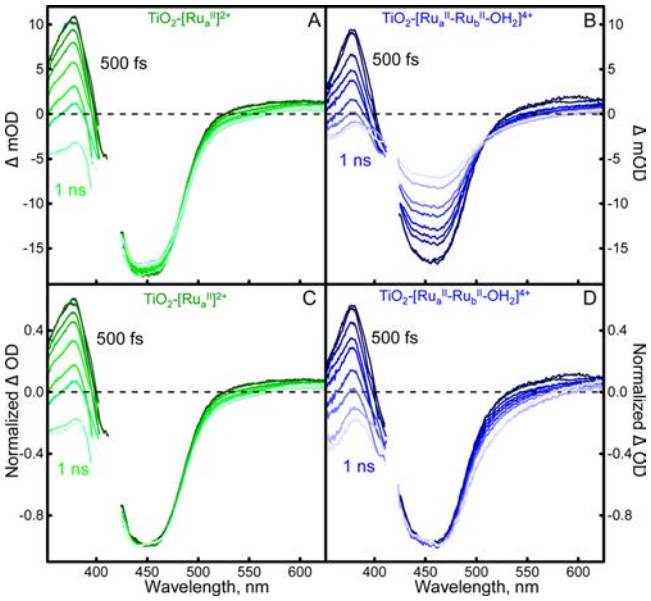

Figure 3. Transient absorption spectra of (A) TiO_2–$[Ru_a^{II}]^{2+}$ and (B) TiO_2–$[Ru_a^{II}$–Ru_b^{II}–$OH_2]^{4+}$ and normalized (C) TiO_2–$[Ru_a^{II}]^{2+}$ and (D) TiO_2–$[Ru_a^{II}$–Ru_b^{II}–$OH_2]^{4+}$ at 500 fs (dark line), 1 ps, 5 ps, 10 ps, 20 ps, 50 ps, 100 ps, 500 ps, and 1 ns (light line) after laser excitation. Both samples were on 1 μm thick nanocrystalline TiO_2 films in aqueous 0.1 M $HClO_4$ at 25 °C. The excitation wavelength was 420 nm.

excited-state absorptions at 380 nm and to the red of 500 nm that arise primarily from $\pi \rightarrow \pi^*$ transitions on the polypyridyl radical anion of the excited state, as well as the ground-state bleach centered at 450 nm. The decay of the excited-state absorptions, which occur without loss of the ground-state bleach (Figure 3A), are a direct signature of electron injection from excited state ($[Ru_a^{II}*]^{2+}$) into TiO_2 (Scheme 2, eq 4).

The rate of electron injection was determined by monitoring the decay of the 380 nm absorption as a function of pump–probe delay, Figure 4A. The decay is multiexponential, with both fast (5.18×10^{10} s^{-1}; τ = 19 ps) and slow (5.0×10^9 s^{-1}; τ = 200 ps) components. In addition to these slower components, there is most likely a sub-100 fs component that falls within our instrument response and, as a consequence, is not detected but has been observed in related complexes.[20]

The distribution of injection rates most likely arises from a combination of factors. Following excitation, the initially formed ^{1}MLCT state, or vibrationally hot triplet states, undergo

dx.doi.org/10.1021/jp410646u | J. Phys. Chem. C XXXX, XXX, XXX–XXX

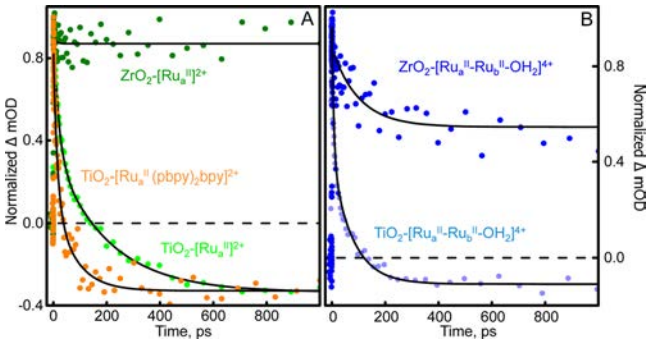

Figure 4. Electron injection kinetics monitored at 380 nm for (A) TiO_2–$[Ru_a^{II}]^{2+}$ (light green), ZrO_2–$[Ru_a^{II}]^{2+}$ (dark green), and TiO_2–$[Ru^{II}(pbpy)_2(bpy)]^{2+}$ (orange) and (B) TiO_2–$[Ru_a^{II}$–Ru_b^{II}–$OH_2]^{4+}$ (light blue) and ZrO_2–$[Ru_a^{II}$–Ru_b^{II}–$OH_2]^{4+}$ (dark blue). The fits are shown in black, and parameters are summarized in Table S1 (Supporting Information). The films were immersed in aqueous 0.1 M $HClO_4$ at 25 °C. The excitation wavelength was 420 nm.

rapid injection. Injection from thermally equilibrated ^{3}MLCT states occurs on time scales ranging from sub-ps to tens of picoseconds.[21,22] The physical origin of the slower injection components arises from the multiple MLCT excited states, each associated with one of the three separate polypyridyl ligands. Injection from TiO_2–$[Ru^{II}(pbpy)_2(bpy)]^{2+}$ (with an amide functionalized ligand replaced by bipyridine, Figure 1) is significantly faster than that from TiO_2–$[Ru_a^{II}]^{2+}$, indicating that the slow components arise from injection by the MLCT excited state lying on the amide-derivatized ligand in the assembly (Figure 4). Partitioning of the photoexcitation among the three ligands gives rise to three excited states with different spatial orientations corresponding to placement of the charge on each of the three ligands. The difference in substituents lifts the degeneracy of the three states, and if the lowest energy ligand is not bound to the surface, its MLCT excited state injects by remote injection,[23,24] or by interligand excitation transfer to the bound ligand followed by injection.[25] Experiments currently underway on a family of related complexes show that localized ligand MLCT excited states are responsible for injection components on the picosecond time scale.

The efficiency of electron injection for TiO_2–$[Ru_a^{II}]^{2+}$ is estimated from the transient absorption spectra on TiO_2 and ZrO_2 to be 72%, with 9% occurring in the first 500 fs after photoexcitation (Figure S1, Supporting Information). Since similar phosphonated chromophores exhibit injection efficiencies approaching unity,[17] the low efficiency observed for this chromophore is most likely due to the slow injection.

The decay of the $\pi \rightarrow \pi^*$ excited-state absorption at 380 and 500 nm in the transient spectra of the assembly on TiO_2, i.e., TiO_2–$[Ru_a^{II}$*–Ru_b^{II}–$OH_2]^{4+}$ (Figure 3B), is qualitative evidence for electron injection following photoexcitation of the assembly. However, these decays also have contributions from the photoexcited catalyst, which has an excited state lifetime of 363 ps (Figure S2, Supporting Information), complicating the quantitative analysis. This rapid deactivation of the catalyst excited state, $[-Ru_b^{II}$*$-OH_2]^{2+}$, is partially responsible for the decay of the bleach observed on TiO_2, as well as the loss of the 380 nm band observed for the assembly on ZrO_2 observed during the first 200 ps (Figure 4B).

Energy Transfer. The photoexcited chromophore can also be deactivated by energy transfer to the catalyst and is observable on ZrO_2 in the absence of injection. Steady-state emission for ZrO_2–$[Ru_a^{II}]^{2+}$ (centered at 640 nm) and ZrO_2–$[Ru_b^{II}OH_2]^{2+}$ (centered at 700 nm) arises from ^{3}MLCT emission following fast intersystem crossing from initially excited ^{1}MLCT (Figure 5A). Emission from ZrO_2–$[Ru_a^{II}$–Ru_b^{II}–$OH_2]^{4+}$ (centered at 665 nm) is quenched and broadened to the red relative to ZrO_2–$[Ru_a^{II}]^{2+}$ due to energy transfer from $[Ru_a^{II}$*$]^{2+}$ to $[Ru_b^{II}$–$OH_2]^{2+}$ (Scheme 2, eq 3). Because the rate of energy transfer (4.8×10^7 s^{-1}, τ = 21 ns), measured by time-resolved emission quenching (Figure 5B), is much faster than the excited state lifetime of the chromophore (450 ns), the efficiency of energy transfer on ZrO_2 is ≈95%. The emission quantum yield for the catalyst is at least 100 times less than emission from the chromophore, based on the relative lifetimes of the two complexes. As a result, emission from the assembly on ZrO_2 arises primarily from the ∼5% of unquenched chromophores that do not undergo energy transfer, as shown by an emission spectrum that resembles the chromophore emission rather than the catalyst. The energy transfer rate for chromophore–catalyst assembly (21 ns) is on the same time scale as in the two chromophore system (33 ns),[4] indicating that the chromophore and catalyst are in close contact in the surface bound assembly.

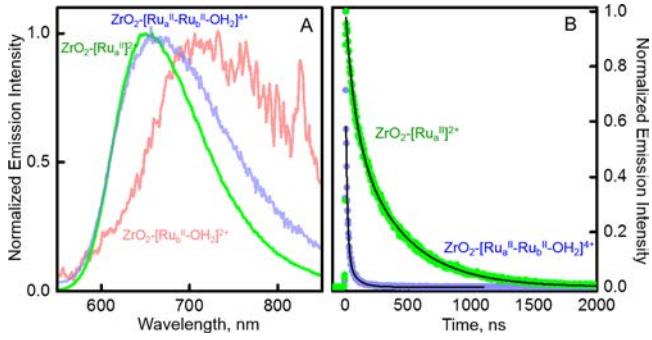

Figure 5. (A) Normalized steady-state emission spectra of ZrO_2–$[Ru_a^{II}]^{2+}$ (green), ZrO_2–$[Ru_a^{II}$–Ru_b^{II}–$OH_2]^{4+}$ (blue), and ZrO_2–$[Ru_b^{II}$–$OH_2]^{2+}$ (red). (B) Time-resolved emission collected at 640 nm of ZrO_2–$[Ru_a^{II}]^{2+}$ (green) and ZrO_2–$[Ru_a^{II}$–Ru_b^{II}–$OH_2]^{4+}$ (blue). The fits (black lines) are summarized in Table S2 (Supporting Information). All film samples were in a quartz cuvette containing aqueous 0.1 M $HClO_4$, 25 °C. The excitation for emission was 450 nm.

Transfer of the Oxidative Equivalent to the Catalyst. The transient absorption spectra of the assembly, TiO_2–$[Ru_a^{II}$–Ru_b^{II}–$OH_2]^{4+}$, differ in detail from those of the chromophore control, TiO_2–$[Ru_a^{II}]^{2+}$. The most notable difference is a decay of the bleach during the first 1 ns after photoexcitation (Figure 3B). This loss of bleach amplitude is due (at least in part) to the presence of photoexcited catalyst, but it also has a contribution associated with the transfer of the oxidative equivalent due to the lower extinction coefficient of the catalyst. While one could in principle extract the time scale for formation of the oxidized catalyst by monitoring this decay, the contribution from catalyst excited state makes this difficult.

The transfer of the oxidative equivalent (Scheme 2, eq 5) can also be detected as a change in shape of the bleach, which broadens to the red as the oxidized chromophore is converted to oxidized catalyst, whose bleach contribution lies to lower energy (Figure 2). This broadening is particularly apparent when the transient spectra are normalized to the maximum bleach intensity (Figure 3D), revealing an 8–10 nm shift in the

dx.doi.org/10.1021/jp410646u | J. Phys. Chem. C XXXX, XXX, XXX–XXX

red edge of the bleach (measured at the 50% point) that begins at about 10 ps and continues over the first nanosecond (Figure 6). This broadening is not observed to the same extent in the

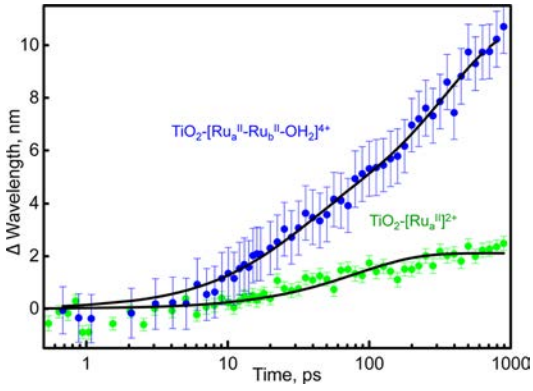

Figure 6. The change in red wavelength of the ground-state bleach (at the 50% point) versus time for TiO_2–$[Ru_a^{II}]^{2+}$ (green) and TiO_2–$[Ru_a^{II}$–Ru_b^{II}–$OH_2]^{4+}$ (blue). The error bars from the linear fit are included. The fits to the curves are shown in black with parameters summarized in Table S3 (Supporting Information).

chromophore control, which shows only a 2 nm shift over this same time period. The shift of the ground-state bleach takes place with both fast (26 ps) and slow (340 ps) components. While the faster component is also observed in the chromophore control, TiO_2–$[Ru_a^{II}]^{2+}$, the slower component is not and we attribute it to the transfer of the oxidative equivalent to the catalyst, $TiO_2(e^-)$–$[Ru_a^{III}$–Ru_b^{II}–$OH_2]^{5+} \rightarrow TiO_2(e^-)$–$[Ru_a^{II}$–$Ru_b^{III}$–$OH_2]^{5+}$.

Because $[-Ru_a^{II}*-]^{2+}$, $[-Ru_a^{III}-]^{3+}$, $[-Ru_b^{II}*-OH_2]^{2+}$, and $[-Ru_b^{III}-OH_2]^{3+}$ all contribute to the transient absorption signal in this spectral window, determining the electron transfer rate simply by monitoring the absorption changes at a single wavelength is problematic. Disentangling the kinetic processes is accomplished by using global analysis based on a singular-value decomposition (SVD) algorithm.

The global analysis fits the transient absorption data matrix between 10 ps and 5 ns to a predefined kinetic model, extracting both spectra for each species and their concentration profiles as a function of time. The kinetic model includes the following processes: (i) electron injection from chromophore excited state (Scheme 2, eq 4), (ii) the transfer of oxidative equivalent to the catalyst (Scheme 2, eq 5), and (iii) excited-state decay of catalyst (Scheme 2, eq 2b). The remaining kinetic processes occur on time scales greater than 5 ns, and are not included in the model. In particular, energy transfer to the catalyst from the chromophore excited state (Scheme 2, eq 3) is 21 ns, $[Ru_a^{II}*]^{2+}$ excited-state decay (Scheme 2, eq 2a) is 450 ns, and back electron transfer (Scheme 2, eq 6) occurs on the microsecond time scale (as discussed below).

The number of adjustable parameters in the global fit of TiO_2–$[Ru_a^{II}$–Ru_b^{II}–$OH_2]^{4+}$ data was reduced by incorporating several key constraints to the spectra and rate constants, which are summarized in Table 1. The injection process was characterized separately by performing the same analysis on the chromophore control, TiO_2–$[Ru_a^{II}]^{2+}$ (Figure 7). This

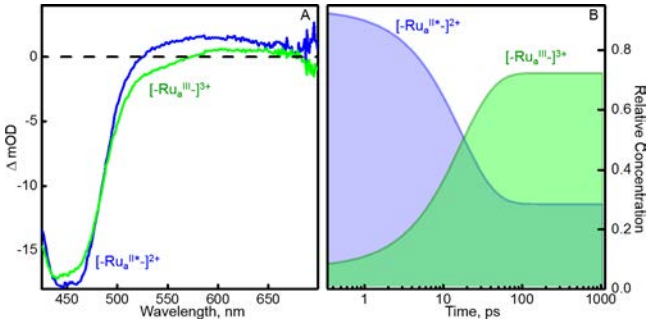

Figure 7. Global analysis of TiO_2–$[Ru_a^{II}]^{2+}$ transient spectra in the 0.5 ps to 1 ns time window. (A) Transient absorption difference spectra for $[-Ru_a^{II}*-]^{2+}$ (blue) and $[-Ru_a^{III}-]^{3+}$ (green). (B) Relative concentration of $[-Ru_a^{II}*-]^{2+}$ (blue) and $[-Ru_a^{III}-]^{3+}$ (green). The residuals for the fit are shown in Figure S3 (Supporting Information).

analysis gave the rate of electron injection (Scheme 2, eq 4) and transient spectra for the chromophore excited state ($[-Ru_a^{II}*-]^{2+}$) and oxidized chromophore ($[-Ru_a^{III}-]^{3+}$). In the analysis of the chromophore control data, the spectrum of $[-Ru_a^{II}*-]^{2+}$ was fixed to the spectrum of TiO_2–$[Ru_a^{II}]^{2+}$ at 500 fs. The initial concentrations of the two species were based on the injection efficiency analysis described above. Specifically, the initial concentrations of $[-Ru_a^{II}*-]^{2+}$ and $[-Ru_a^{III}-]^{3+}$ were set at 0.93 and 0.07 to account for the loss of 9% of the injecting chromophores during the instrument response time. The model also accounted for the 28% of chromophores that do not inject during the first nanosecond. The analysis returned

Table 1. Summary of Global Analysis Constraint and Initial/Final Concentrations

		concentration	
chemical species	spectral contribution	initial	final
chromophore excited state, $[-Ru_a^{II}*-]^{2+}$	fixed[a]	0.79	0.24[c]
oxidized chromophore, $[-Ru_a^{III}-]^{3+}$	fixed[a]	0.06	0.12[d]
catalyst excited state, $[-Ru_b^{II}*-OH_2]^{2+}$	fixed[b]	0.15	0.00
oxidized catalyst, $[-Ru_b^{III}-OH_2]^{3+}$	adjustable	0.00	0.49
ground state	nonabsorptive	0.00	0.15
dynamical process	rate constant		
electron injection, eq 4	fixed[a]	$(18\ ps)^{-1}$	
catalyst excited-state decay, eq 2b	fixed[b]	$(363\ ps)^{-1}$	
oxidative transfer, eq 5	adjustable	$(380\ ps)^{-1}$	

[a]From SVD analysis of TiO_2–$[Ru_a^{II}]^{2+}$ spectra shown in Figure 7A. [b]Transient absorption data obtained for the catalyst control, ZrO_2–$[Ru_b^{II}$–$OH_2]^{2+}$, Supporting Information, Figure S2. [c]Accounts for the $[-Ru_a^{II}*-]^{2+}$ population that does not inject during the first 1 ns, based on injection efficiency measurements. [d]Final concentration accounts for the fraction of chromophores that are attached to assemblies containing catalysts in the peroxide state.

dx.doi.org/10.1021/jp410646u | J. Phys. Chem. C XXXX, XXX, XXX–XXX

a rate constant of 5.6×10^{10} s^{-1} (τ = 18 ps) and the spectra shown in Figure 7A. The global analysis is limited to describing the injection with a single average rate constant, and thus cannot reproduce the kinetic complexity observed in the transient data. Nevertheless, it represents a reasonable description of the injection kinetics and was used for the injection rate in the analysis of the assembly.

Also fixed were the known spectra for $[-Ru_a^{II*}-]^{2+}$, $[-Ru_a^{III}-]^{3+}$, and $[-Ru_b^{II*}-OH_2]^{2+}$ (Table 1). The initial concentrations in Table 1 account for the relative molar absorptivity of the chromophore and catalyst, and the ultrafast injection yield of the chromophore, which results in the presence of oxidized chromophore ($[Ru_a^{III}]^{3+}$) during the instrument response. The kinetic model also takes into account the overall injection yield (72%) and the fraction of assemblies on the surface whose catalysts are in the photophysically inert, peroxide state (20%). The only adjustable parameters in the global analysis are the spectrum of the oxidized catalyst $[-Ru_b^{III}-OH_2]^{3+}$ and the rate constant for the transfer of the oxidative equivalent.

The spectra that result from the global analysis of $TiO_2-[Ru_a^{II}-Ru_b^{II}-OH_2]^{4+}$ are shown in Figure 8A. The spectrum

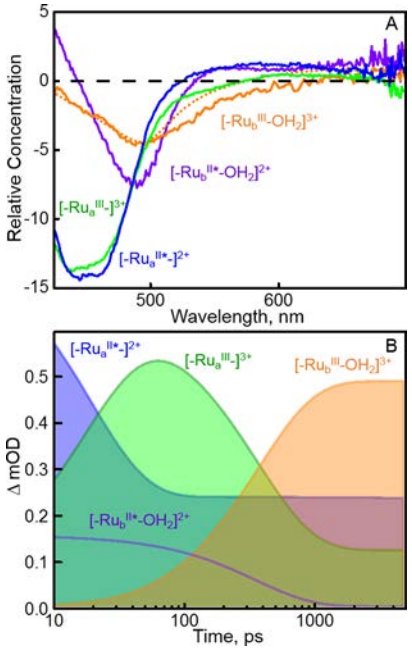

Figure 8. Global analysis of $TiO_2-[Ru_a^{II}-Ru_b^{II}-OH_2]^{4+}$. (A) The spectra of $[-Ru_a^{II*}-]^{2+}$ (blue), $[-Ru_a^{III}-]^{3+}$ (green), $[-Ru_b^{II*}-OH_2]^{2+}$ (purple), and $[-Ru_b^{III}-OH_2]^{3+}$ (orange). Also shown is the calculated ΔA spectrum for $[Ru_b^{II}-OH_2]^{2+}/[Ru_b^{III}-OH_2]^{3+}$ (dashed orange). (B) Relative concentrations of $[-Ru_a^{II*}-]^{2+}$ (blue), $[-Ru_a^{III}-]^{3+}$ (green), $[-Ru_b^{II*}-OH_2]^{2+}$ (purple), and $[-Ru_b^{III}-OH_2]^{3+}$ (orange). The residuals for the global fit are shown in Figure S4 (Supporting Information). The concentrations shown at 10 ps are different from the initial concentrations for the fit due to electron injection of the chromophore that occurs between 500 fs and 10 ps.

for $[-Ru_b^{III}-OH_2]^{3+}$ closely resembles the calculated ΔA spectrum for $[Ru_b^{II}-OH_2]^{2+}/[Ru_b^{III}-OH_2]^{3+}$ obtained spectroelectrochemically. The concentration profiles for $[-Ru_a^{II*-}]^{2+}$, $[-Ru_a^{III}-]^{3+}$, $[-Ru_b^{II}-OH_2]^{2+}$, and $[-Ru_b^{III}-OH_2]^{3+}$ are shown in Figure 8B. From the global analysis, the calculated rate constant for the transfer of the oxidative equivalent to the catalyst is 2.6×10^9 s^{-1} (τ = 380 ps). The rate constants extracted from the global analysis are an oversimplification, and the dynamics are best described by a distribution of rates that arise from several factors. Flexibility in the chromophore–catalyst linker will give rise to a variety of configurations, each with a slightly different rate, and furthermore, since these structures are not static, dynamical fluctuations will cause the rates to change with time. Also complicating the picture is the range of chromophore–TiO_2 binding configurations that are present, with each characteristic configuration potentially giving rise to its own kinetic response. In light of these factors, the rate constants extracted from the SVD analysis should be viewed as average rates. The analysis indicates an overall efficiency for transfer of the oxidative equivalent of 49%. The relatively low efficiency is due to the presence of inactive peroxide assemblies on the surface, as well as the relatively low electron injection efficiency.

Charge Recombination. Recombination of the electron in TiO_2 with the hole on either the chromophore, $[Ru_a^{III}]^{3+}$, or catalyst, $[Ru_b^{III}-OH_2]^{3+}$ (Scheme 2, eq 6), is monitored by following the decay of the ground-state bleach at 490 nm on the microsecond time scale (Figure 9). The decay kinetics are

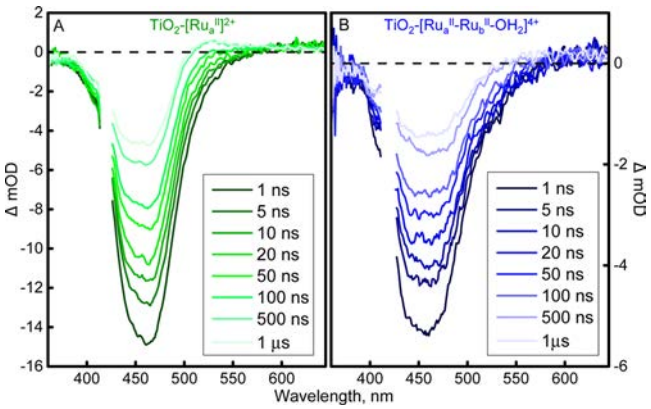

Figure 9. Transient absorption spectra of (A) $TiO_2-[Ru_a^{II}]^{2+}$ and (B) $TiO_2-[Ru_a^{II}-Ru_b^{II}-OH_2]^{4+}$ from 1 ns to 1 μs after laser excitation. Both samples were on 1 μm thick nanocrystalline TiO_2 in aqueous 0.1 M $HClO_4$ at 25 °C. The excitation wavelength was 420 nm.

qualitatively similar for the assembly and the chromophore control, Figure 10. Both are highly multiexponential with power law behavior observed at long times, as indicated by the linear behavior when the decay is depicted in $\log(\Delta A)$ vs $\log(t)$ plots. While power law behavior is characteristic of many types of dynamical phenomena, it is a characteristic feature of trap-to-trap hopping in metal oxide materials.[26–29] This suggests that the decay might be determined more by internal electron dynamics within the TiO_2 than the back electron transfer process itself. Hanson and co-workers reached a similar conclusion in their study of back electron transfer of phosphonate-derivatized Ru(II) dyes on TiO_2.[17] This conclusion also accounts for the similarity observed in recombination kinetics for $TiO_2-[Ru_a^{II}]^{2+}$ and $TiO_2-[Ru_a^{II}-Ru_b^{II}-OH_2]^{4+}$.

CONCLUSIONS

An oligoproline functionalized with a phosphonated $Ru(bpy)_3^{2+}$ chromophore and a $Ru(bpy)(Mebimpy)(OH_2)^{2+}$ derivatized water oxidation catalyst was loaded onto nanoporous TiO_2, and its interfacial and intra-assembly electron

dx.doi.org/10.1021/jp410646u | J. Phys. Chem. C XXXX, XXX, XXX–XXX

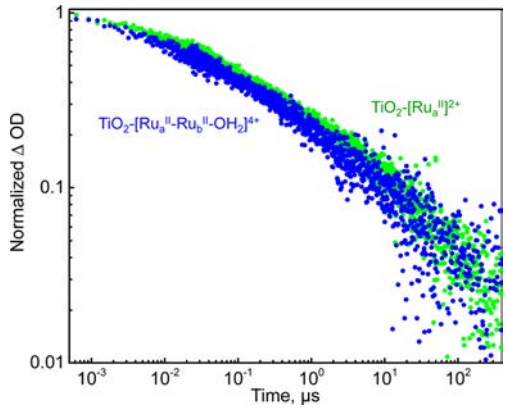

Figure 10. Transient absorption kinetics for back electron transfer monitored at 490 nm for TiO_2–[Ru_a^{II}]$^{2+}$ (green) and TiO_2–[Ru_a^{II}–Ru_b^{II}–OH_2]$^{4+}$ (blue). The signal was inverted and normalized. The excitation wavelength was 420 nm. All samples were on 1 μm thick TiO_2 films in aqueous 0.1 M $HClO_4$ solution at 25 °C.

transfer dynamics were analyzed by transient femtosecond absorption spectroscopy. Upon ultrafast electron injection from the chromophore excited state into TiO_2, the oxidative equivalent is transferred from the chromophore to the catalyst. With the use of global analysis, the transfer of the oxidative equivalent to the catalyst occurred with $k = 2.6 \times 10^9$ s^{-1} (τ = 380 ps). The assembly resulted in efficiency for transfer of the oxidative equivalent to the catalyst of nearly 100%, based on the relative rates for oxidative transfer and charge recombination, with an overall efficiency of 49% for the initial DSPEC photoexcitation step. The loss in overall efficiency is a result of the electron injection efficiency of the chromophore (72%) and the 20% of inactive catalysts in the sample. A redesign of the assembly with a chromophore that has an injection efficiency near unity (by separating the amide functional group from the bipyridine ligand) and 100% active catalysts would increase the overall efficiency to 76%. Future studies will utilize the versatility of the proline scaffold and focus on the influence of spacer distance between the chromophore and catalyst on intra-assembly electron transfer.

■ ASSOCIATED CONTENT

Supporting Information

Additional photophysical data (Figures S1–4 and Tables S1–3). This material is available free of charge via the Internet at http://pubs.acs.org.

■ AUTHOR INFORMATION

Corresponding Author

*E-mail: john_papanikolas@unc.edu. Phone: (919) 962-1619.

Notes

The authors declare no competing financial interest.

■ ACKNOWLEDGMENTS

This research was supported solely by the UNC EFRC: Center for Solar Fuels, an Energy Frontier Research Center funded by the U.S. Department of Energy Office of Basic Energy Science under award DE-SC0001011.

■ REFERENCES

(1) Alstrum-Acevedo, J. H.; Brennaman, M. K.; Meyer, T. J. Chemical Approaches to Artificial Photosynthesis. 2. *Inorg. Chem.* **2005**, *44*, 6802–6827.

(2) Lewis, N. S.; Nocera, D. G. Powering the Planet: Chemical Challenges in Solar Energy Utilization. *Proc. Natl. Acad. Sci. U.S.A.* **2006**, *103*, 15729–15735.

(3) Li, F.; Jiang, Y.; Zhang, B.; Huang, F.; Gao, Y.; Sun, L.; Towards, A. Solar Fuel Device: Light-Driven Water Oxidation Catalyzed by a Supramolecular Assembly. *Angew. Chem., Int. Ed.* **2012**, *51*, 2417–2420.

(4) Norris, M. R.; Concepcion, J. J.; Harrison, D. P.; Binstead, R. A.; Ashford, D. L.; Fang, Z.; Templeton, J. L.; Meyer, T. J. Redox Mediator Effect on Water Oxidation in a Ruthenium-Based Chromophore–Catalyst Assembly. *J. Am. Chem. Soc.* **2013**, *135*, 2080–2083.

(5) Song, W.; Glasson, C. R. K.; Luo, H.; Hanson, K.; Brennaman, M. K.; Concepcion, J. J.; Meyer, T. J. Photoinduced Stepwise Oxidative Activation of a Chromophore–Catalyst Assembly on TiO_2. *J. Phys. Chem. Lett.* **2011**, *2*, 1808–1813.

(6) Ashford, D. L.; Song, W.; Concepcion, J. J.; Glasson, C. R. K.; Brennaman, M. K.; Norris, M. R.; Fang, Z.; Templeton, J. L.; Meyer, T. J. Photoinduced Electron Transfer in a Chromophore–Catalyst Assembly Anchored to TiO_2. *J. Am. Chem. Soc.* **2012**, *134*, 19189–19198.

(7) Wang, L.; Ashford, D. L.; Thompson, D. W.; Meyer, T. J.; Papanikolas, J. M. Watching Photoactivation in a Ru(II) Chromophore–Catalyst Assembly on TiO_2 by Ultrafast Spectroscopy. *J. Phys. Chem. C* **2013**, *117*, 24250–24258.

(8) Huang, Z.; Geletii, Y. V.; Musaev, D. G.; Hill, C. L.; Lian, T. Spectroscopic Studies of Light-driven Water Oxidation Catalyzed by Polyoxometalates. *Ind. Eng. Chem. Res.* **2012**, *51*, 11850–11859.

(9) Magnuson, A.; Anderlund, M.; Johansson, O.; Lindblad, P.; Lomoth, R.; Polivka, T.; Ott, S.; Stensjo, K.; Styring, S.; Sundstrom, V.; et al. Biomimetic and Microbial Approaches to Solar Fuel Generation. *Acc. Chem. Res.* **2009**, *42*, 1899–1909.

(10) Huang, P.; Magnuson, A.; Lomoth, R.; Abrahamsson, M.; Tamm, M.; Sun, L.; van Rotterdam, B.; Park, J.; Hammarstrom, L.; Akermark, B.; et al. Photo-Induced Oxidation of a Dinuclear Mn_2(II,II) Complex to the Mn_2(III,IV) State by Inter- and Intramolecular Electron Transfer to Ru-III Tris-Bipyridine. *J. Inorg. Biochem.* **2002**, *91*, 159–172.

(11) Sun, L. C.; Raymond, M. K.; Magnuson, A.; LeGourrierec, D.; Tamm, M.; Abrahamsson, M.; Kenez, P. H.; Martensson, J.; Stenhagen, G.; Hammarstrom, L.; et al. Towards an Artificial Model for Photosystem II: A Manganese(II,II) Dimer Covalently Linked to Ruthenium(II) Tris-Bipyridine via a Tyrosine Derivative. *J. Inorg. Biochem.* **2000**, *78*, 15–22.

(12) Concepcion, J. J.; Jurss, J. W.; Templeton, J. L.; Meyer, T. J. One Site is Enough. Catalytic Water Oxidation by [Ru(tpy)(bpm)-(OH_2)]$^{2+}$ and [Ru(tpy)(bpz)(OH_2)]$^{2+}$. *J. Am. Chem. Soc.* **2008**, *130*, 16462–16463.

(13) Concepcion, J. J.; Tsai, M.-K.; Muckerman, J. T.; Meyer, T. J. Mechanism of Water Oxidation by Single-Site Ruthenium Complex Catalysts. *J. Am. Chem. Soc.* **2010**, *132*, 1545–1557.

(14) Concepcion, J. J.; Jurss, J. W.; Brennaman, M. K.; Hoertz, P. G.; Patrocinio, A. O. v. T.; Murakami Iha, N. Y.; Templeton, J. L.; Meyer, T. J. Making Oxygen with Ruthenium Complexes. *Acc. Chem. Res.* **2009**, *42*, 1954–1965.

(15) Ma, D.; Bettis, S. E.; Hanson, K.; Minakova, M.; Alibabaei, L.; Fondrie, W.; Ryan, D. M.; Papoian, G. A.; Meyer, T. J.; Waters, M. L.; et al. Interfacial Energy Conversion in RuII Polypyridyl-Derivatized Oligoproline Assemblies on TiO_2. *J. Am. Chem. Soc.* **2013**, *135*, 5250–5253.

(16) Ryan, D. M.; Coggins, M. K.; Concepcion, J. J.; Ashford, D. L.; Fang, Z.; Alibabaei, L.; Ma, D.; Meyer, T. J.; Waters, M. L. Synthesis and Electrochemical Analysis of a Series of Helical Peptide Based Chromophore–Water Oxidation Catalyst Assemblies on a Semiconductor Surface. *J. Am. Chem. Soc.* **2013**, manuscript in preparation.

(17) Hanson, K.; Brennaman, M. K.; Ito, A.; Luo, H.; Song, W.; Parker, K. A.; Ghosh, R.; Norris, M. R.; Glasson, C. R. K.; Concepcion, J. J.; et al. Structure−Property Relationships in Phosphonate-Derivatized, Ru^{II} Polypyridyl Dyes on Metal Oxide Surfaces in an Aqueous Environment. *J. Phys. Chem. C* **2012**, *116*, 14837−14847.
(18) Juris, A.; Balzani, V.; Barigelletti, F.; Campagna, S.; Belser, P.; Vonzelewsky, A. Ru(II) Polypyridine Complexes - Photophysics, Photochemistry, Electrochemistry, and Chemi-Luminescence. *Coord. Chem. Rev.* **1988**, *84*, 85−277.
(19) Concepcion, J. J.; Jurss, J. W.; Norris, M. R.; Chen, Z.; Templeton, J. L.; Meyer, T. J. Catalytic Water Oxidation by Single-Site Ruthenium Catalysts. *Inorg. Chem.* **2010**, *49*, 1277−1279.
(20) Asbury, J. B.; Ellingson, R. J.; Ghosh, H. N.; Ferrere, S.; Nozik, A. J.; Lian, T. Femtosecond IR Study of Excited-State Relaxation and Electron-Injection Dynamics of $Ru(dcbpy)_2(NCS)_2$ in Solution and on Nanocrystalline TiO_2 and Al_2O_3 Thin Films. *J. Phys. Chem. B* **1999**, *103*, 3110−3119.
(21) Myahkostupov, M.; Piotrowiak, P.; Wang, D.; Galoppini, E. Ru(II)-Bpy Complexes Bound to Nanocrystalline TiO_2 Films through Phenyleneethynylene (OPE) Linkers: Effect of the Linkers Length on Electron Injection Rates. *J. Phys. Chem. C* **2007**, *111*, 2827−2829.
(22) Benkö, G.; Kallioinen, J.; Korppi-Tommola, J. E. I.; Yartsev, A. P.; Sundström, V. Photoinduced Ultrafast Dye-to-Semiconductor Electron Injection from Nonthermalized and Thermalized Donor States. *J. Am. Chem. Soc.* **2001**, *124*, 489−493.
(23) Liu, F.; Meyer, G. J. Remote and Adjacent Excited-State Electron Transfer at TiO_2 Interfaces Sensitized to Visible Light with Ru(II) Compounds. *Inorg. Chem.* **2005**, *44*, 9305−9313.
(24) Benkö, G.; Kallioinen, J.; Myllyperkiö, P.; Trif, F.; Korppi-Tommola, J. E. I.; Yartsev, A. P.; Sundström, V. Interligand Electron Transfer Determines Triplet Excited State Electron Injection in RuN_3−Sensitized TiO_2 Films. *J. Phys. Chem. B* **2004**, *108*, 2862−2867.
(25) Schoonover, J. R.; Dattelbaum, D. M.; Malko, A.; Klimov, V. I.; Meyer, T. J.; Styers-Barnett, D. J.; Gannon, E. Z.; Granger, J. C.; Aldridge, W. S.; Papanikolas, J. M. Ultrafast Energy Transfer between the ^{3}MLCT State of $[Ru^{II}(dmb)_2(bpy\text{-}an)]^{2+}$ and the Covalently Appended Anthracene. *J. Phys. Chem. A* **2005**, *109*, 2472−2475.
(26) McNeil, I. J.; Ashford, D. L.; Luo, H.; Fecko, C. J. Power-Law Kinetics in the Photoluminescence of Dye-Sensitized Nanoparticle Films: Implications for Electron Injection and Charge Transport. *J. Phys. Chem. C* **2012**, *116*, 15888−15899.
(27) Mora-Seró, I.; Dittrich, T.; Belaidi, A.; Garcia-Belmonte, G.; Bisquert, J. Observation of Diffusion and Tunneling Recombination of Dye-Photoinjected Electrons in Ultrathin TiO2 Layers by Surface Photovoltage Transients. *J. Phys. Chem. B* **2005**, *109*, 14932−14938.
(28) Seki, K.; Wojcik, M.; Tachiya, M. Dispersive-Diffusion-Controlled Distance-Dependent Recombination in Amorphous Semiconductors. *J. Chem. Phys.* **2006**, *124*, 044702−044711.
(29) Kopidakis, N.; Benkstein, K. D.; van de Lagemaat, J.; Frank, A. J. Transport-Limited Recombination of Photocarriers in Dye-Sensitized Nanocrystalline TiO_2 Solar Cells. *J. Phys. Chem. B* **2003**, *107*, 11307−11315.

THE JOURNAL OF PHYSICAL CHEMISTRY A

Article

pubs.acs.org/JPCA

Photophysical Characterization of a Chromophore/Water Oxidation Catalyst Containing a Layer-by-Layer Assembly on Nanocrystalline TiO_2 Using Ultrafast Spectroscopy

Stephanie E. Bettis, Kenneth Hanson, Li Wang, Melissa K. Gish, Javier J. Concepcion, Zhen Fang, Thomas J. Meyer, and John M. Papanikolas*

Department of Chemistry, University of North Carolina, CB 3290, Chapel Hill, North Carolina 27599, United States

Supporting Information

ABSTRACT: Femtosecond transient absorption spectroscopy is used to characterize the first photoactivation step in a chromophore/water oxidation catalyst assembly formed through a "layer-by-layer" approach. Assemblies incorporating both chromophores and catalysts are central to the function of dye-sensitized photoelectrosynthesis cells (DSPECs) for generating solar fuels. The chromophore, $[Ru_a^{II}]^{2+}$ = $[Ru(pbpy)_2(bpy)]^{2+}$, and water oxidation catalyst, $[Ru_b^{II}\text{-}OH_2]^{2+}$ = $[Ru(4,4'\text{-}(CH_2PO_3H_2)_2bpy)(Mebimpy)(H_2O)]^{2+}$, where bpy = 2,2′-bipyridine, pbpy = 4,4′-$(PO_3H_2)_2$bpy, and Mebimpy = 2,6-bis(1-methylbenzimidazol-2-yl)pyridine), are arranged on nanocrystalline TiO_2 via phosphonate-Zr(IV) coordination linkages. Analysis of the transient spectra of the assembly (denoted TiO_2-$[Ru_a^{II}$-Zr-Ru_b^{II}-$OH_2]^{4+}$) reveal that photoexcitation initiates electron injection, which is then followed by the transfer of the oxidative equivalent from the chromophore to the catalyst with a rate of $k_{ET} = 5.9 \times 10^9\ s^{-1}$ (τ = 170 ps). While the assembly, TiO_2-$[Ru_a^{II}$-Zr-Ru_b^{II}-$OH_2]^{4+}$, has a near-unit efficiency for transfer of the oxidative equivalent to the catalyst, the overall efficiency of the system is only 43% due to nonproductive photoexcitation of the catalyst and nonunit efficiency for electron injection. The modular nature of the layer-by-layer system allows for variation of the light-harvesting chromophore and water oxidation catalyst for future studies to increase the overall efficiency.

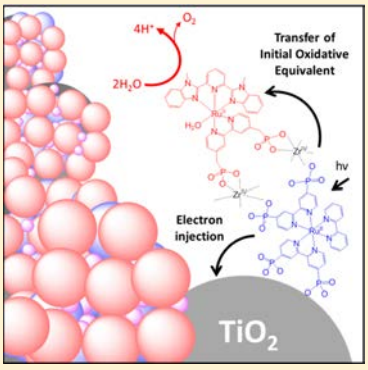

INTRODUCTION

One strategy for solar fuels production is a dye-sensitized photoelectrosynthesis cell (DSPEC) that can use sunlight to drive water oxidation and reduction of protons to hydrogen or CO_2 to carbon-based fuels.[1,2] Central to a DSPEC device architecture is designing a means for arranging the light-absorbing chromophores and catalysts in close proximity to facilitate electron-transfer activation of the catalyst toward water oxidation. There are a limited number of examples of systems that successfully incorporate light-harvesting chromophores and catalysts on nanocrystalline semiconductor surfaces.[3−9] Most approaches are synthetically challenging, often with a lack of versatility. A "layer-by-layer" approach was recently reported by Hanson et. al[10] based on earlier work of Mallouk and Haga.[11−14] This approach does not require the prior synthesis of a covalently bonded assembly. The chromophore and catalyst are synthesized independently and then bound to the metal oxide surface in a stepwise, self-assembled fashion, (i.e., chromophore then Zr^{4+} ions and then catalyst).

Solar water oxidation requires the stepwise transfer of four electrons and four protons in the net reaction $2H_2O \rightarrow O_2 + 4H^+ + 4e^-$.[1] Polypyridyl-based Ru(II) catalysts have been developed for water oxidation, and the catalytic mechanisms are understood both in solution and on metal oxide surfaces.[15−17] In a DSPEC, each step in the water oxidation cycle involves the photo-oxidation of the chromophore by electron injection into the metal oxide film, which is then followed by the transfer of the oxidative equivalent to the catalyst (i.e., intra-assembly chromophore to catalyst electron transfer). Because the completion of the water oxidation cycle requires the consecutive absorption of four photons, the rapid transfer of the oxidative equivalent is critical to efficient DSPEC function.

The layer-by-layer system includes a chromophore, $[Ru_a^{II}]^{2+}$ ($[Ru(pbpy)_2(bpy)]^{2+}$, bpy = 2,2′-bipyridine and pbpy = 4,4′-$(PO_3H_2)_2$bpy), and a water oxidation catalyst, $[Ru_b^{II}\text{-}OH_2]^{2+}$ ($[Ru(4,4'\text{-}(CH_2PO_3H_2)_2bpy)(Mebimpy)(H_2O)]^{2+}$, Mebimpy = 2,6-bis(1-methylbenzimidazol-2-yl)pyridine)), linked by Zr^{4+} ions that are coordinated to the phosphonate groups on each of the metal complexes (Figure 1). This approach results in a self-assembled film consisting of a layer of $[Ru_a^{II}]^{2+}$ chromophores anchored to the TiO_2 through one pbpy ligand and, through a second pbpy ligand, a layer of $[Ru_b^{II}\text{-}OH_2]^{2+}$ catalyst complexes.[10] Here, we report the photophysical characterization of the first photoactivation step of the water oxidation catalyst in this assembly, TiO_2-$[Ru_a^{II}$-Zr-Ru_b^{II}-$OH_2]^{4+}$, using femtosecond transient absorption spectroscopy.

Special Issue: Current Topics in Photochemistry

Received: November 12, 2013
Revised: April 14, 2014
Published: April 15, 2014

dx.doi.org/10.1021/jp411139j | J. Phys. Chem. A 2014, 118, 10301−10308

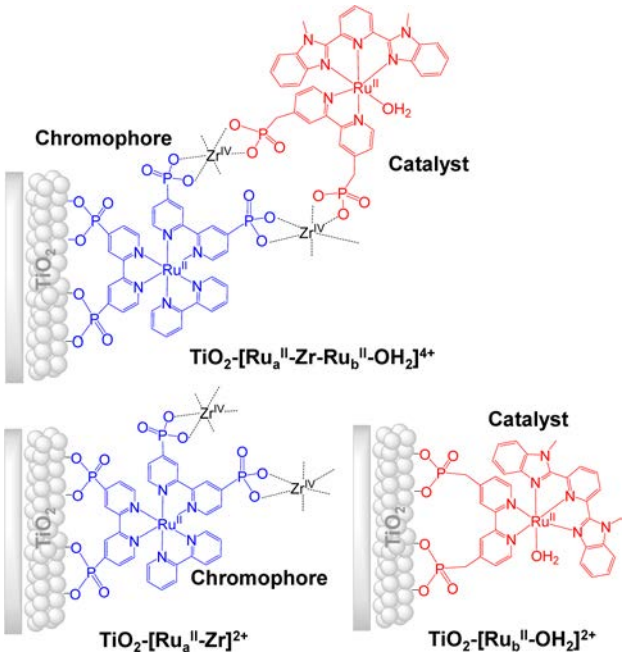

Figure 1. Schematic design of the bilayer molecular assembly $[Ru_a^{II}$-Zr-Ru_b^{II}-$OH_2]^{4+}$, the chromophore $[Ru_a^{II}$-$Zr]^{2+}$, and catalyst $[Ru_b^{II}$-$OH_2]^{2+}$on nanocrystalline TiO_2 films. The bonding motif depicted represents one of several different possible binding configurations between pbpy ligands and the metal oxide surface.

The kinetic processes involved in this step are illustrated in Scheme 1. Photoexcitation of the assembly TiO_2-$[Ru_a^{II}$-Zr-Ru_b^{II}-$OH_2]^{4+}$ can occur at either the chromophore (Scheme 1, eq 1a), or the catalyst (eq 1b). Excitation of the chromophore initiates electron injection into TiO_2, TiO_2-$[Ru_a^{II*}$-Zr-Ru_b^{II}-$OH_2]^{4+}$ → $TiO_2(e^-)$-$[Ru_a^{III}$-Zr-Ru_b^{II}-$OH_2]^{5+}$ (eq 4), which is then followed by an intra-assembly electron-transfer process that moves the oxidative equivalent from the chromophore to the catalyst, $TiO_2(e^-)$-$[Ru_a^{III}$-Zr-Ru_b^{II}-$OH_2]^{5+}$ → $TiO_2(e^-)$-$[Ru_a^{II}$-Zr-Ru_b^{III}-$OH_2]^{5+}$ (eq 5), and the completion of the first photoactivation step in the water oxidation cycle. Experiments reported here indicate that for the bilayer assembly, activation of the catalyst occurs with a time constant of 170 ps. While energy transfer from the photoexcited chromophore to the catalyst, TiO_2-$[Ru_a^{II*}$-Zr-Ru_b^{II}-$OH_2]^{4+}$ → TiO_2-$[Ru_a^{II}$-Zr-Ru_b^{II*}-$OH_2]^{4+}$ (eq 3), is a potential deactivation pathway, its time scale is considerably slower (20 ns) than electron injection, limiting its relevance. A more important deactivation pathway is recombination of the injected electron in the semiconductor with the oxidized catalyst, $TiO_2(e^-)$-$[Ru_a^{II}$-Zr-Ru_b^{III}-$OH_2]^{5+}$ → TiO_2-$[Ru_a^{II}$-Zr-Ru_b^{II}-$OH_2]^{5+}$ (eq 6b), which returns the assembly to its initial state and results in the loss of the transiently stored oxidative equivalent as thermal excitation of the surrounding medium.

EXPERIMENTAL METHODS

The synthesis of $[Ru_a^{II}]^{2+}$ and $[Ru_b^{II}$-$OH_2]^{2+}$ and the layer-by-layer method have been previously published.[10] Briefly the layer-by-layer method was carried out by soaking the nanocrystalline film in a sequence of three separate aqueous solutions, each overnight (12 h). The preparation of sample TiO_2-$[Ru_a^{II}$-$Zr]^{2+}$ involved soaking the nanocrystalline film in 0.1 M $HClO_4$ solutions of $[Ru_a^{2+}]^{2+}$ (150 μM) followed by $ZrOCl_2$ (0.5 mM).[10] Sample TiO_2-$[Ru_a^{II}$-Zr-Ru_b^{II}-$OH_2]^{4+}$ was prepared in a similar manner by soaking the film in 0.1 M $HClO_4$ solutions of (1) $[Ru_a^{II}]^{2+}$ (150 μM), (2) $ZrOCl_2$ (0.5 mM), and (3) $[Ru_b^{II}$-$OH_2]^{2+}$ (150 μM).[10]

Scheme 1. Schematic Diagram Illustrating the Kinetic Processes for TiO_2-$[Ru_a^{II}$-Zr-Ru_b^{II}-$OH_2]^{4+}$ That Occur Following Photoexcitation

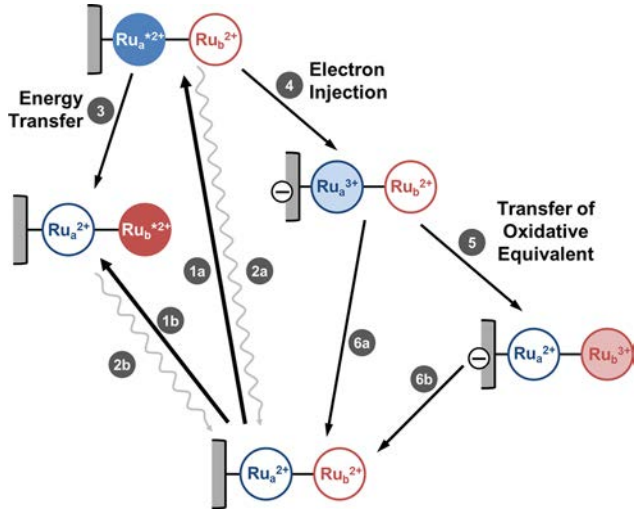

Sample Preparation. The films were placed in a 1.0 cm cuvette at a 45° angle from the incident laser beam. All samples were purged in argon for >45 min just prior to data collection. The solvent for each sample was 0.1 M $HClO_4$. The surface coverages on TiO_2 for TiO_2-$[Ru_a^{II}$-$Zr]^{2+}$, TiO_2-$[Ru_b^{II}$-$OH_2]^{2+}$, and TiO_2-$[Ru_a^{II}$-Zr-Ru_b^{II}-$OH_2]^{4+}$ were $\Gamma = 2.6 \times 10^{-8}$, 2.0×10^{-8}, and 3.1×10^{-8} mol/cm^2/μm, respectively, consistent with closely packed surfaces.[17] Similarly, surface coverages for ZrO_2-$[Ru_a^{II}$-$Zr]^{2+}$, ZrO_2-$[Ru_b^{II}$-$OH_2]^{2+}$, and ZrO_2-$[Ru_a^{II}$-Zr-Ru_b^{II}-$OH_2]^{4+}$ were $\Gamma = 3.0 \times 10^{-8}$, 2.4×10^{-8}, and 2.9×10^{-8} mol/cm^2/μm, respectively. A single bilayer structure has an absorbance of 1.5 at the pump wavelength (420 nm).

Instrumentation. The spectrometers used to perform steady-state absorption and emission spectroscopy, transient emission measurements, and the collection of transient absorption spectra on the femtosecond to microsecond time scale have been described elsewhere.[9]

RESULTS AND DISCUSSION

The initial photoactivation step in the water oxidation cycle of the chromophore−catalyst bilayer film on TiO_2 was characterized using femtosecond transient absorption spectroscopy. Our results indicate that photoexcitation of the chromophore results in electron injection into the TiO_2 with 81% efficiency on time scales that range from femtoseconds to hundreds of picoseconds to produce an oxidized chromophore. Transfer of the oxidative equivalent (i.e., catalyst to chromophore electron transfer) occurs with a time constant of 170 ps. This process is substantially faster than charge recombination, which occurs on the microsecond time scale,[18] suggesting that the intra-assembly electron-transfer step occurs with nearly unit efficiency.

Photoexcitation. The absorptions spectra of both the chromophore, $[Ru_a^{II}$-$Zr]^{2+}$, and the catalyst, $[Ru_b^{II}$-$OH_2]^{2+}$, show well-resolved bands between 400 and 500 nm that arise primarily from singlet metal-to-ligand charge transfer (^{1}MLCT) transitions (Figure 2). The maximum absorption of the catalyst (494 nm) is red-shifted relative to the chromophore (473 nm)

dx.doi.org/10.1021/jp411139j | J. Phys. Chem. A 2014, 118, 10301−10308

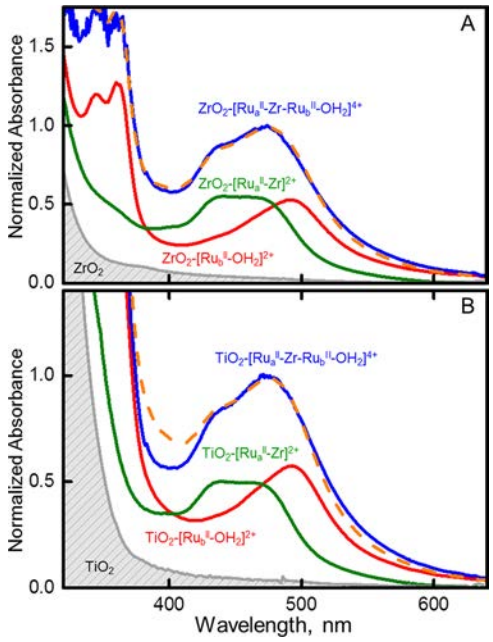

Figure 2. (A) Absorption spectra of 3 μm thick films consisting of ZrO_2 (gray), ZrO_2-$[Ru_a^{II}$-Zr$]^{2+}$ (green), ZrO_2-$[Ru_b^{II}$-$OH_2]^{4+}$ (red), and ZrO_2-$[Ru_a^{II}$-Zr-Ru_b^{II}-$OH_2]^{4+}$ (blue). The sum of ZrO_2-$[Ru_a^{II}$-Zr$]^{2+}$ and ZrO_2-$[Ru_b^{II}$-$OH_2]^{2+}$ is depicted as a dashed orange line. (B) Absorption spectra for a 3 μm TiO_2 film (gray), TiO_2-$[Ru_a^{II}$-Zr$]^{2+}$ (green), TiO_2-$[Ru_b^{II}$-$OH_2]^{2+}$ (red), and TiO_2-$[Ru_a^{II}$-Zr-Ru_b^{II}-$OH_2]^{4+}$ (blue). The sum of TiO_2-$[Ru_a^{II}$-Zr$]^{2+}$ and TiO_2-$[Ru_b^{II}$-$OH_2]^{2+}$ is depicted as a dashed orange line. All samples are in aqueous 0.1 M $HClO_4$, and spectra were collected under ambient conditions.

as a result of the extended π-orbital conjugation of the Mebimpy ligand, which lowers its π^* orbital energy relative to bpy. The ground-state absorption spectra of the bilayer assembly, $[Ru_a^{II}$-Zr-Ru_b^{II}-$OH_2]^{4+}$, on TiO_2 and ZrO_2 are consistent with a superposition of the absorption spectra of individual components ($[Ru_a^{II}$-Zr$]^{2+}$ and $[Ru_b^{II}$-$OH_2]^{2+}$) in the MLCT region (Figure 2), indicating that the metal complexes in the bilayer are only weakly electronically coupled. The superposition spectra were obtained by adding the component spectra with a chromophore to the catalyst ratio of 1:1.5 for TiO_2 and 1:1.3 for ZrO_2. An excess of catalyst in the film is not unusual for this system due to the nature of the assembly formation. On the basis of our analysis of the absorption spectra on TiO_2 at 420 nm, ~53% of the photons are absorbed by the chromophore, with the remaining 47% being absorbed by the catalyst.

Electron Injection. *Chromophore Excited-State Injection, TiO_2-$[Ru_a^{II}$-Zr$]^{2+}$.* The transient absorption spectrum 1 ps after photoexcitation of TiO_2-$[Ru_a^{II}]^{2+}$ exhibits excited-state absorptions at 380 nm and to the red of 500 nm that correspond to $\pi\pi^*$ transitions associated with the bpy^- radical anion, as well as the ^{1}MLCT ground-state bleach (400−500 nm), Figure 3A. The absorbance at 500 nm could also contain contribution from the injected electron in TiO_2;[19] however, the similarity of the transient absorption spectra for the chromophore on TiO_2 and for the chromophore on ZrO_2, where injection is not possible, suggests that it is only a minor contribution (Figure 4). As the excited-state absorptions decay in amplitude, there is only a slight loss of the magnitude of the ground-state bleach. While the decay of the bleach is indicative of replenishment of the ground-state population on the picosecond time scale, presumably through rapid back electron transfer, this process is much slower and occurs to a lesser extent compared to loss of the excited-state absorption, indicating that the spectral evolution is due primarily to electron injection from $[Ru_a^{II}*]^{2+}$ into TiO_2. The rate for electron injection into TiO_2, which is given by the decay of this absorption band (Figure 3B), is multiexponential, with both fast (13 ps) and slow (130 ps) components. In addition to the slow decay components, there is also an ultrafast component to the injection (<100 fs) that occurs within our instrument response and as a result is not observed; however, it has been reported by other groups for similar systems.[20] The distribution of injection times is due to the range of processes that occur upon photoexcitation. Rapid electron injection occurs from the initially formed ^{1}MLCT, or vibrationally "hot" ^{3}MLCT states, while the slower components correspond to injection from the thermally equilibrated ^{3}MLCT excited state.[21,22]

Addition of the Zr^{4+} ions, which coordinate to the unbound phosphonate groups, alters the decay of the 380 nm band (Figure 3D). Fits of the decay to a biexponential function show that the primary difference is in the relative amplitudes of the two components, as opposed to their time constants (τ_1 = 14 ps and τ_2 = 140 ps), which are similar to those observed for TiO_2-$[Ru_a^{II}]^{2+}$ (Table S1, Supporting Information). While it is difficult to quantify the injection rate given the multiexponential nature of the decay, our observations show, at least qualitatively, that the average rate for electron injection is decreased upon coordination of Zr^{4+} to the remote phosphonate groups.

The origin of this affect may stem from the heteroleptic nature of the chromophore. Upon photoexcitation, the excited state is distributed among the three ligands, whose energies differ due to different chemical substituents. For example, the electron-withdrawing phosphonate groups on the pbpy ligand stabilize its energy by about 200 mV relative to bpy. This results in a driving force for transfer of MLCT excited states located on the bpy ligand to pbpy ligands attached to the metal oxide surface. The slower injection observed in the presence of the Zr^{4+} ions may stem from a stabilization of the pbpy ligand energy upon coordination with Zr^{4+}. If the energy order is reversed (i.e., the ancillary ligand is lower in energy than the surface-bound ligand), then MLCT states that become trapped on the outer pbpy ligands must either inject remotely[23,24] or first undergo interligand excitation transfer,[25] slowing down the injection process.

Injection efficiencies are estimated by comparing amplitudes of the 380 nm $bpy^{\bullet-}$ absorption relative to the ground-state bleach using a method described previously (Figure S1, Supporting Information).[8] For TiO_2-$[Ru_a^{II}$-Zr$]^{2+}$, the injection efficiency is estimated to be 81% at 1 ns, with 17% of the injection events taking place within 500 fs. Similar measurements made in the absence of the Zr^{4+} ions (i.e., for TiO_2-$[Ru_a^{II}]^{2+}$) yield higher injection efficiencies (95% overall and 20% ultrafast), indicating that the coordination of the Zr^{4+} ions to the phosphonate groups results in slower injection times and lower injection yields.

Catalyst Injection. The transient absorption spectra of the assembly TiO_2-$[Ru_a^{II}$-Zr-Ru_b^{II}-$OH_2]^{4+}$ also show a decay of the 380 nm excited-state absorption on the picosecond time scale (Figure 4). Because of the structure of the bilayer, it is possible that upon photoexcitation, either the catalyst injects remotely, or some fraction is bound to the TiO_2 and undergoes direct injection.

dx.doi.org/10.1021/jp411139j | J. Phys. Chem. A 2014, 118, 10301−10308

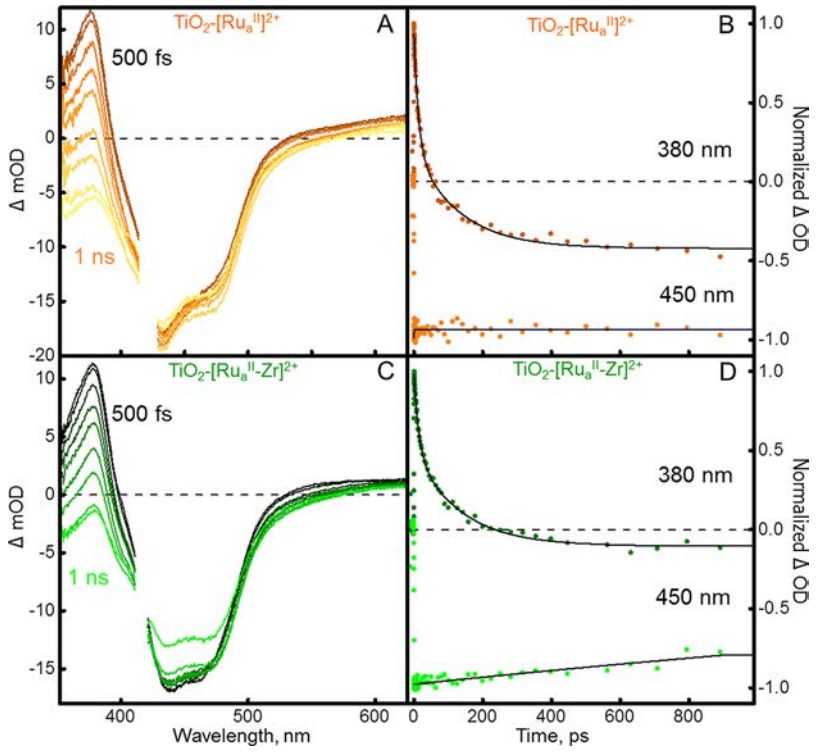

Figure 3. (A) Series of transient absorption spectra obtained from TiO_2-$[Ru_a^{II}]^{2+}$ at 500 fs (dark line), 1, 5, 10, 20, 50, 100, 500, and 1000 ps (light line) after 420 nm laser excitation. (B) Transient absorption kinetics for TiO_2-$[Ru_a^{II}]^{2+}$ at 380 (dark orange) and 450 nm (light orange). (C) Series of transient absorption spectra of TiO_2-$[Ru_a^{II}$-Zr$]^{2+}$ observed at 500 fs (dark line), 1, 5, 10, 20, 50, 100, 500, and 1000 ps (light line) after 420 nm laser excitation. (D) Transient absorption kinetics for TiO_2-$[Ru_a^{II}$-Zr$]^{2+}$ at 380 (dark green) and 450 nm (light green). Nonlinear least-squares fits to biexponential decay models are shown as solid lines, with time constants and amplitudes summarized in Table S1 (Supporting Information). All samples were in aqueous 0.1 M $HClO_4$, and spectra were collected under ambient conditions.

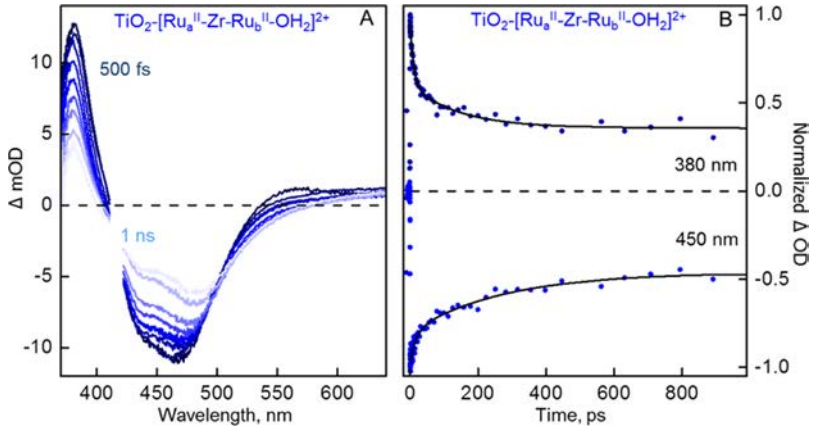

Figure 4. (A) Series of transient absorption spectra obtained from the bilayer assembly, TiO_2-$[Ru_a^{II}$-Zr-Ru_b^{II}-$OH_2]^{4+}$, at 500 fs (dark line), 1, 5, 10, 20, 50, 100, 500, and 1000 ps (light line) after laser excitation at 420 nm. (B) Transient absorption kinetics for $[Ru_a^{II}$-Zr-Ru_b^{II}-$OH_2]^{4+}$ on TiO_2 at 380 (dark) and 450 nm (light). Nonlinear least-squares fits to biexponential decay models are shown as solid lines, with time constants and amplitudes summarized in Table S2 (Supporting Information). All samples were in aqueous 0.1 M $HClO_4$ under ambient conditions.

The transient absorption spectrum of the assembly at 1 ps after excitation, TiO_2-$[Ru_a^{II}$-Zr-Ru_b^{II}-$OH_2]^{4+}$, can be described as the sum of TiO_2-$[Ru_a^{II}$-Zr$]^{2+}$ and ZrO_2-$[Ru_b^{II}$-$OH_2]^{2+}$ spectra (Figure 5). Because the catalyst cannot inject into ZrO_2, the ZrO_2-$[Ru_b^{II}$-$OH_2]^{2+}$ transient spectrum reflects solely the catalyst excited state. The fact that the catalyst contribution to the transient spectra of TiO_2-$[Ru_a^{II}$-Zr-Ru_b^{II}-$OH_2]^{4+}$ can be accounted for entirely by using the spectrum of ZrO_2-$[Ru_b^{II}$-$OH_2]^{2+}$ is consistent with electron injection into TiO_2 only from the excited state of the chromophore $[Ru_a^{II}]^{2+}$, with little or no contribution from photoexcited catalysts.

Catalyst Excited-State Decay. The catalyst $[Ru_b^{II}$-$OH_2]^{2+}$ excited state is best seen on a ZrO_2 film where electron injection is unfavorable. The transient absorption spectrum of ZrO_2-$[Ru_b^{II}$-$OH_2]^{2+}$ has the expected ground-state bleach centered at 490 nm and excited-state absorptions at 380 and 550 nm, similar to TiO_2-$[Ru_a^{II}]^{2+}$ (Figure 6A). The major difference in the excited-state spectra of the catalyst $[Ru_b^{II}$-$OH_2]^{2+}$, when compared to the chromophore $[Ru_a^{II}]^{2+}$, is the

dx.doi.org/10.1021/jp411139j | J. Phys. Chem. A 2014, 118, 10301−10308

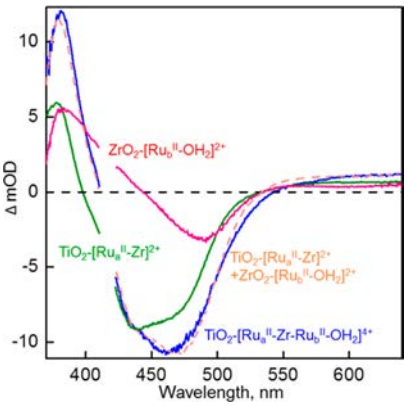

Figure 5. Transient absorption spectra obtained at 1 ps after 420 nm photoexcitation of TiO_2-$[Ru_a^{II}$-Zr$]^{2+}$ (green), TiO_2-$[Ru_a^{II}$-Zr-Ru_b^{II}-$OH_2]^{4+}$ (blue), and TiO_2-$[Ru_b^{II}$-$OH_2]^{2+}$ (red). The sum of TiO_2-$[Ru_a^{II}$-Zr$]^{2+}$ and TiO_2-$[Ru_b^{II}$-$OH_2]^{2+}$ is depicted as the dashed orange line. All samples were on 3 μm thick nanocrystalline metal oxide films in aqueous 0.1 M $HClO_4$, and spectra were collected under ambient conditions.

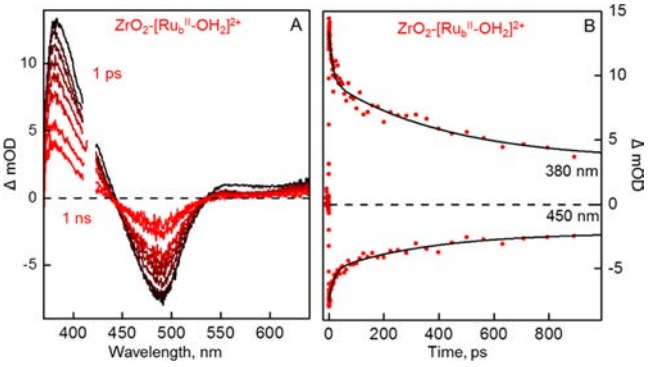

Figure 6. (A) Series of transient absorption spectra obtained from ZrO_2-$[Ru_b^{II}$-$OH_2]^{2+}$ at 1 (dark line), 5, 10, 20, 50, 100, 500, and 1000 ps (light line) after 420 nm laser excitation. (B) Transient absorption kinetics of ZrO_2-$[Ru_b^{II}$-$OH_2]^{2+}$ at 380 (dark) and 490 nm (light). Nonlinear least-squares fits to biexponential decay models are shown as solid lines, with time constants and amplitudes summarized in Table S3 (Supporting Information). The sample was on a 3 μm thick nanocrystalline ZrO_2 film in aqueous 0.1 M $HClO_4$, and spectra were obtained under ambient conditions.

rate for excited-state decay. The decay of the excited state for ZrO_2-$[Ru_b^{II}$-$OH_2]^{2+}$ (Figure 6B) is multiexponential, with a fast component of 18 ps and slow component of 364 ps. The fast component is attributed to an excited-state relaxation process (e.g., vibrational relaxation or interligand excitation transfer) and the long component to the catalyst excited-state lifetime.[26] The short lifetime of the catalyst indicates that excited-state decay of the catalyst contributes to the decay observed in the 380 nm absorption feature in TiO_2-$[Ru_a^{II}$-Zr-Ru_b^{II}-$OH_2]^{4+}$.

Energy Transfer. Energy transfer from the photoexcited chromphore to the catalyst (Scheme 1, eq 3) is observed when the assembly is anchored to nanocrystalline ZrO_2, where electron injection is not possible. Figure 7A shows steady-state emission spectra for ZrO_2-$[Ru_a^{II}$-Zr$]^{2+}$ (centered at 650 nm), ZrO_2-$[Ru_b^{II}$-$OH_2]^{2+}$ (centered at 700 nm), and ZrO_2-$[Ru_a^{II}$-Zr-Ru_b^{II}-$OH_2]^{4+}$ (centered at 660 nm), each normalized to its emission maximum. The emission spectrum of the assembly is considerably weaker and broadened on the lower-energy side relative to the chromophore (ZrO_2-$[Ru_a^{II}$-Zr$]^{2+}$). Time-resolved emission measurements show the lifetime of the assembly to be 20 ns, Figure 7B. This is considerably shorter than that of the chromophore (450 ns), indicating the presence of an added mechanism for excited-state quenching. Given the broadening of the emission band to the red, we attribute the quenching to energy transfer from the chromophore $[Ru_a^{II*}]^{2+}$ to the catalyst $[Ru_b^{II}$-$OH_2]^{2+}$ (Scheme 1, eq 3). The slow rate of this process compared to electron injection into TiO_2 (200 ps) indicates that it is not a competitive excited-state deactivation pathway for the assembly on TiO_2.

Transfer of the Oxidative Equivalent to the Catalyst. The transient absorption spectra for TiO_2-$[Ru_a^{II}$-Zr-Ru_b^{II}-$OH_2]^{4+}$ differ from those of TiO_2-$[Ru_a^{II}$-Zr$]^{2+}$. The most prominent difference is a decrease in the ground-state bleach intensity that occurs during the first nanosecond after photoexcitation (Figure 4). The loss of the ground-state bleach is most likely due to the decay of the catalyst, which can also be excited at 420 nm and whose lifetime is 363 ps. A second clear difference is seen in the normalized transient absorption spectra of TiO_2-$[Ru_a^{II}$-Zr-Ru_b^{II}-$OH_2]^{4+}$ (Figure 8A). In this representation, the shift and broadening of the ground-state bleach to the red, which begins almost immediately (10 ps) and continues during the next 1000 ps, is clearly evident (Figure 8C). Although the chromophore bleach also broadens, it occurs to a much lesser extent (Figure 8B). The magnitude of the broadening is quantified in Figure 8C, which shows the shift in the wavelength of the red edge of the bleach (measured at the 50% point) as a function of pump−probe delay. The assembly TiO_2-$[Ru_a^{II}$-Zr-Ru_b^{II}-$OH_2]^{4+}$ has a shift of 20 nm on the low-energy side of the bleach, whereas the chromophore, TiO_2-$[Ru_a^{II}$-Zr$]^{2+}$, only shifts by 5 nm (Figure 8C). This broadening occurs with both a fast component (18 ps), which is also seen in the shift of the chromophore, and slow component (136 ps). The slow component is attributed to the transfer of the oxidative equivalent to the catalyst. No shift in the ground-state bleach is observed for ZrO_2-$[Ru_a^{II}$-Zr-Ru_b^{II}-$OH_2]^{4+}$ (Figure S2, Supporting Information), confirming that this intra-assembly electron-transfer process requires electron injection from the chromophore into TiO_2.

The overlapping spectral bands of $[\text{-}Ru_a^{II}\text{-}]^{2+}$, $[\text{-}Ru_a^{III}\text{-}]^{3+}$, $[\text{-}Ru_b^{II}$-$OH_2]^{2+}$, and $[\text{-}Ru_b^{III}$-$OH_2]^{3+}$ make it difficult to extract a rate constant for oxidative transfer by merely following the transient absorption signal at a single wavelength. Separating the contributions from each species is accomplished by a global analysis of the transient spectra using a singular value decomposition (SVD) method.

In this global analysis, the transient absorption spectra from 10 ps to 5 ns for TiO_2-$[Ru_a^{II}$-Zr-Ru_b^{II}-$OH_2]^{4+}$ were fit to a predefined kinetic model. The model includes (i) electron injection into TiO_2 (Scheme 1, eq 4), (ii) intra-assembly electron transfer (Scheme 1, eq 5), and (iii) decay of the catalyst excited state (Scheme 1, eq 2b). The other processes in Scheme 1 take place on time scales longer than 5 ns. Specifically, the excited state of $[Ru_a^{II}]^{2+}$ (Scheme 1, eq 2a) has a lifetime of 450 ns, the energy transfer (Scheme 1, eq 3) occurs with a lifetime of 20 ns, and charge recombination (Scheme 1, eq 6) takes place over hundreds of nanoseconds to microseconds.

The number of adjustable parameters in the global fit of TiO_2-$[Ru_a^{II}$-Zr-Ru_b^{II}-$OH_2]^{4+}$ were reduced with the integration of several known spectra and rate constants (Table 1). The rate for electron injection (Scheme 1 eq 4) and transient spectra for the chromophore excited state ($[\text{-}Ru_a^{II*}\text{-}]^{2+}$) and oxidized

dx.doi.org/10.1021/jp411139j | J. Phys. Chem. A 2014, 118, 10301−10308

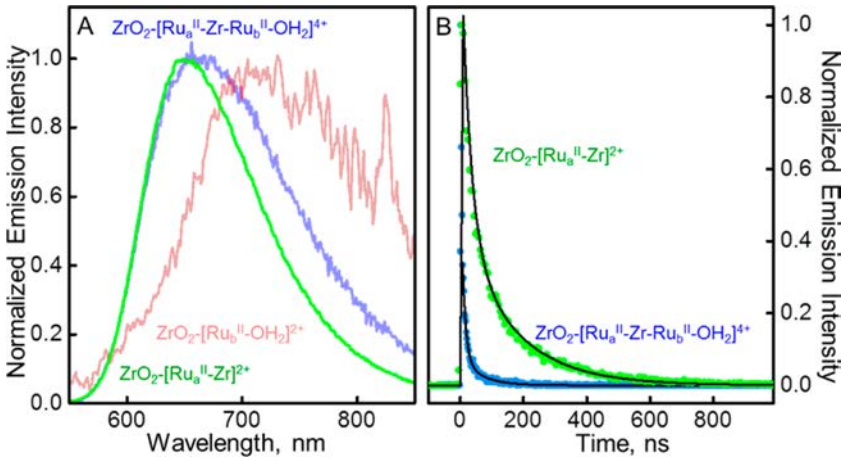

Figure 7. (A) Steady-state emission spectra of ZrO_2-$[Ru_a^{II}$-Zr$]^{2+}$ (green), ZrO_2-$[Ru_a^{II}$-Zr-Ru_b^{II}-$OH_2]^{4+}$ (blue), and ZrO_2-$[Ru_b^{II}$-$OH_2]^{4+}$ (red). Each spectrum is normalized to its maximum intensity. (B) Time-resolved emission of ZrO_2-$[Ru_a^{II}$-Zr$]^{2+}$ (green) and ZrO_2-$[Ru_a^{II}$-Zr-Ru_b^{II}-$OH_2]^{4+}$ (blue) collected at 640 nm. Nonlinear least-squares fits to a biexponential decay model are shown as black lines, and the time constants and amplitudes are summarized in Table S4 (Supporting Information). Measurements were performed in aqueous 0.1 M $HClO_4$ under ambient conditions.

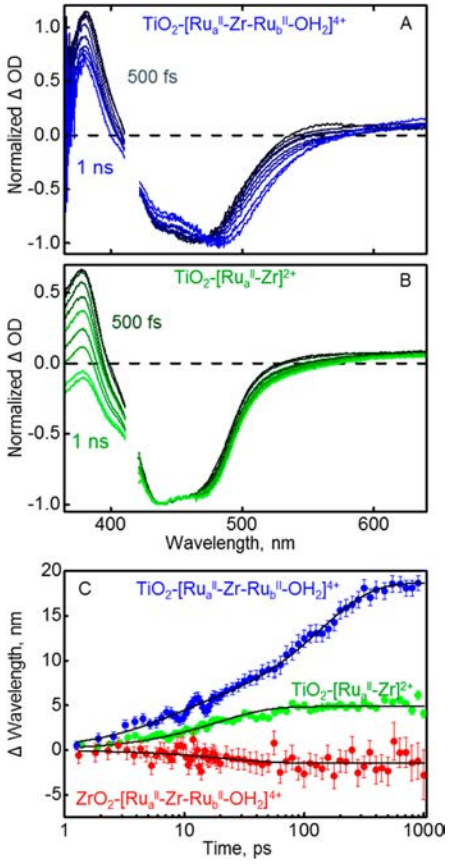

Figure 8. Series of transient absorption spectra normalized to bleach amplitude for (A) TiO_2-$[Ru_a^{II}$-Zr-Ru_b^{II}-$OH_2]^{4+}$ and (B) TiO_2-$[Ru_a^{II}$-Zr$]^{2+}$ at 500 fs (dark line), 1, 5, 10, 20, 50, 100, 500, and 1000 ps (light line) after 420 nm laser excitation. (C) Change in wavelength of the low-energy side of the ground-state bleach (measured at the 50% point) as a function of pump−probe delay. Data sets are shown for TiO_2-$[Ru_a^{II}$-Zr$]^{2+}$ (green), TiO_2-$[Ru_a^{II}$-Zr-Ru_b^{II}-$OH_2]^{4+}$ (blue), and ZrO_2-$[Ru_a^{II}$-Zr-Ru_b^{II}-$OH_2]^{4+}$ (red). The solid lines are nonlinear least-squares fits to a biexponential model, with amplitudes and time constants summarized in Table S5 (Supporting Information). All samples were in aqueous 0.1 M $HClO_4$, and spectra were collected under ambient conditions.

Table 1. Summary of Global Analysis Constraint and Initial/Final Concentration

chemical species	spectral contribution	initial	final
chromophore excited state, $[\text{-}Ru_a^{II}*\text{-}]^{2+}$	fixed[a]	0.46	0.10[c]
oxidized chromophore, $[\text{-}Ru_a^{III}\text{-}]^{3+}$	fixed[a]	0.07	0.00
catalyst excited state, $[\text{-}Ru_b^{II}*\text{-}OH_2]^{2+}$	fixed[b]	0.47	0.00
oxidized catalyst, $[\text{-}Ru_b^{III}\text{-}OH_2]^{3+}$	adjustable	0.00	0.43
ground state	nonabsorptive	0.00	0.47[d]
dynamical process	**rate constant**		
electron injection, eq 4	fixed[a]	$(9.1\ ps)^{-1}$	
oxidative transfer, eq 5	adjustable	$(170\ ps)^{-1}$	
catalyst excited-state decay, eq 2B	fixed[b]	$(363\ ps)^{-1}$	

[a]Spectra obtained from global analysis of TiO_2-$[Ru_a^{II}$-Zr$]^{2+}$ transient spectra. [b]Transient absorption spectra at 500 fs of ZrO_2-$[Ru_b^{II}$-$OH_2]^{2+}$, Figure 6A. [c]Accounts for $[\text{-}Ru_a^{II}*\text{-}]^{2+}$ population that does not inject during the first 1 ns. Values are based on experimental measurements of the injection efficiency. [d]The value reflects the fraction of photexcited catalysts.

chromophore ($[\text{-}Ru_a^{III}\text{-}]^{3+}$) were obtained from a similar analysis on the chromophore control TiO_2-$[Ru_a^{II}$-Zr$]^{2+}$ (Figure 9).

In this analysis, the spectrum of $[\text{-}Ru_a^{II}*\text{-}]^{2+}$ was fixed to the spectrum of TiO_2-$[Ru_a^{II}$-Zr$]^{2+}$ at 0.5 ps. The initial concentrations of $[\text{-}Ru_a^{II}*\text{-}]^{2+}$ and $[\text{-}Ru_a^{III}\text{-}]^{3+}$ were set to 0.67 and 0.14, respectively, to account for the 17% of the chromophores that inject within the instrument response and the 19% that do not inject during the first nanosecond, as determined by the analysis of the injection efficiency described above. The fit yields an electron injection rate of $k = 1.1 \times 10^{11}\ s^{-1}$ (9 ps), and the spectra are shown in Figure 9A. The calculated $[\text{-}Ru_a^{III}\text{-}]^{3+}$ spectrum is in reasonable agreement with the difference spectrum, ΔA ($[Ru^{II}]^{2+}/[Ru^{III}]^{3+}$), measured spectroelectrochemically (Figure 9A), which also shows a broadening to red. This analysis of the transient spectra describes the injection with a single average rate constant and thus cannot reproduce the multiexponential kinetics observed in the transient data. Still, it is a reasonable description of the injection process, and for this reason, it was employed in the analysis of the transient spectra for the bilayer assembly described below.

dx.doi.org/10.1021/jp411139j | J. Phys. Chem. A 2014, 118, 10301−10308

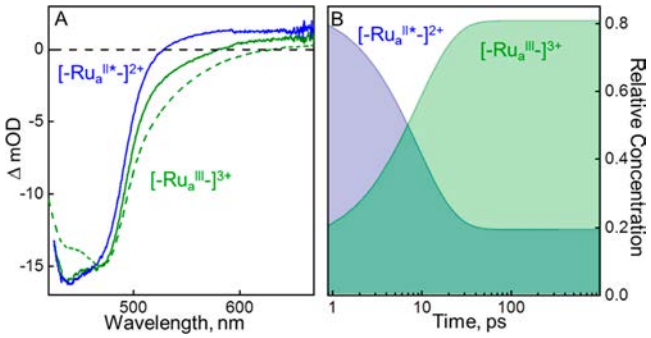

Figure 9. Results of the global analysis of the TiO_2-[Ru_a^{II}-Zr]$^{2+}$ transient spectra. (A) Spectral contributions for [-Ru_a^{II}*-]$^{2+}$ (blue) and [-Ru_a^{III}-]$^{3+}$ (green solid). Also shown for comparison is the difference spectrum (ΔA) measured for [Ru^{II}]$^{2+}$/[Ru^{III}]$^{3+}$ using spectroelectrochemical methods (green dashed). (B) Relative concentration of [-Ru_a^{II}*-]$^{2+}$ (blue) and [-Ru_a^{III}-]$^{3+}$ (green) as a function of pump−probe delay. The residuals are shown in Figure S3 (Supporting Information).

The initial conditions for the global analysis also fixed the spectra for [-Ru_a^{II}*-]$^{2+}$, [-Ru_a^{III}-]$^{3+}$, and [-Ru_b^{II}*-OH_2]$^{2+}$ (Table 1). The initial concentrations reflect the chromophore to catalyst ratio of 1:1.5 (discussed above) and their relative molar absorptivities (0.68 and 0.32). The fit also takes into account the presence of the oxidized chromophore ([Ru_a^{III}]$^{3+}$) that appears within the instrument response due to ultrafast injection, as well as the overall injection yield (81%). The only adjustable parameters in this analysis are the spectra for the catalyst excited state and oxidized catalyst, [-Ru_b^{II}*-OH_2]$^{2+}$* and [-Ru_b^{III}-OH_2]$^{3+}$, and the rate constant for transfer of the oxidative equivalent to the catalyst (Scheme 1, eq 5).

Shown in Figure 10A are the spectral contributions for each of the transient species. The spectra of [-Ru_a^{III}-]$^{3+}$ and [-Ru_b^{III}-OH_2]$^{3+}$ closely resemble the calculated ΔA spectra for ([Ru_a^{II}]$^{2+}$/[Ru_a^{III}]$^{3+}$) and ([Ru_b^{II}-OH_2]$^{2+}$/[Ru_b^{III}-OH_2]$^{3+}$). The relative concentration profiles of each species are shown in Figure 10B. The analysis indicates that the rate constant for the transfer of the oxidative equivalent is $k = 5.9 \times 10^9$ s^{-1} (170 ps). This rate is comparable to that reported for chromophore−catalyst dimer system[8] and a factor of 2 faster than an assembly on a peptide scaffold incorporating the same chromophore and catalyst.[9] The rapid transfer compared to the peptide assembly is consistent with the closer proximity of the chromophore and catalyst in the layer-by-layer system. The efficiency for the transfer of the oxidative equivalent is nearly 100% (based on relative lifetimes), but the overall efficiency of the assembly is only 43% due to a combination of photoexcitation and rapid excited-state decay of the catalyst and incomplete electron injection from the chromophore.

CONCLUSIONS

A layer-by-layer scaffold containing a phosphonated [Ru(bpy)$_3$]$^{2+}$ chromophore and a Ru(bpy)(Mebimpy)$(OH_2)^{2+}$ water oxidation catalyst was loaded onto nanoporous TiO_2, and the first photoactivation step in the DSPEC was analyzed using femtosecond transient absorption spectroscopy. Upon photoexcitation, the chromophore undergoes picosecond electron injection into TiO_2 followed by transfer of the oxidative equivalent to the catalyst. Analysis of the transient spectra reveals a rate for the transfer of the oxidative equivalent to the catalyst of $k = 5.9 \times 10^9$ s^{-1} (170 ps). The efficiency for the transfer of the oxidative equivalent to the catalyst was found to be nearly 100%, with an overall efficiency for the assembly of 43%. This layer-by-layer architecture is an effective scaffold for DSPECs with its ability to position the chromophore and catalyst on a nanocrystalline TiO_2 surface in close proximity.

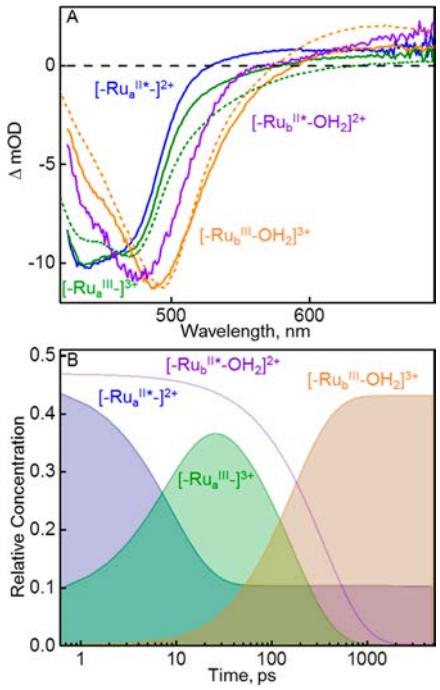

Figure 10. Results of global analysis of the TiO_2-[Ru_a^{II}-Zr-Ru_b^{II}-OH_2]$^{4+}$ transient spectra. (A) Spectral contributions for [-Ru_a^{II}*-]$^{2+}$ (blue), [-Ru_a^{III}-]$^{3+}$ (green), [-Ru_b^{II}*-OH_2]$^{2+}$ (purple), and [-Ru_b^{III}-OH_2]$^{3+}$ (orange). Also shown for comparison are the difference spectra (ΔA) for [Ru_a^{II}]$^{2+}$/[Ru_a^{III}]$^{3+}$ (dashed green) and [Ru_b^{II}-OH_2]$^{2+}$/[Ru_b^{III}-OH_2]$^{3+}$ (dashed orange) measured using spectroelectrochemical methods. (B) Relative concentrations of [-Ru_a^{II}*-]$^{2+}$ (blue), [-Ru_a^{III}-]$^{3+}$ (green), [-Ru_b^{II}*-OH_2]$^{2+}$ (purple), and [-Ru_b^{III}-OH_2]$^{3+}$ (orange) versus time. The residuals are shown in Figure S4 (Supporting Information).

ASSOCIATED CONTENT

Supporting Information

Experimental results, Figures S1−S4, showing spectra for the electron injection efficieny, normalized transient absorption spectra, and residuals from global analyses, and Tables S1−S5, giving a summary of the fits for the various kinetic traces. This material is available free of charge via the Internet at http://pubs.acs.org.

AUTHOR INFORMATION

Corresponding Author

*E-mail: john_papanikolas@unc.edu. Phone: (919) 962-1619.

Notes

The authors declare no competing financial interest.

ACKNOWLEDGMENTS

This research was supported solely by the UNC EFRC: Center for Solar Fuels, an Energy Frontier Research Center funded by the U.S. Department of Energy Office of Basic Energy Science under award DE-SC0001011.

REFERENCES

(1) Alstrum-Acevedo, J. H.; Brennaman, M. K.; Meyer, T. J. Chemical Approaches to Artificial Photosynthesis. 2. *Inorg. Chem.* **2005**, *44*, 6802−6827.

(2) Lewis, N. S.; Nocera, D. G. Powering the Planet: Chemical Challenges in Solar Energy Utilization. *Proc. Nat. Acad. Sci. U.S.A.* **2006**, *103*, 15729−15735.

(3) Ashford, D. L.; Song, W.; Concepcion, J. J.; Glasson, C. R. K.; Brennaman, M. K.; Norris, M. R.; Fang, Z.; Templeton, J. L.; Meyer, T. J. Photoinduced Electron Transfer in a Chromophore−Catalyst Assembly Anchored to TiO_2. *J. Am. Chem. Soc.* **2012**, *134*, 19189−19198.

(4) Li, F.; Jiang, Y.; Zhang, B.; Huang, F.; Gao, Y.; Sun, L. Towards a Solar Fuel Device: Light-Driven Water Oxidation Catalyzed by a Supramolecular Assembly. *Angew. Chem., Int. Ed.* **2012**, *51*, 2417−2420.

(5) Ma, D.; Bettis, S. E.; Hanson, K.; Minakova, M.; Alibabaei, L.; Fondrie, W.; Ryan, D. M.; Papoian, G. A.; Meyer, T. J.; Waters, M. L.; et al. Interfacial Energy Conversion in Ru^{II} Polypyridyl-Derivatized Oligoproline Assemblies on TiO_2. *J. Am. Chem. Soc.* **2013**, *135*, 5250−5253.

(6) Norris, M. R.; Concepcion, J. J.; Harrison, D. P.; Binstead, R. A.; Ashford, D. L.; Fang, Z.; Templeton, J. L.; Meyer, T. J. Redox Mediator Effect on Water Oxidation in a Ruthenium-Based Chromophore−Catalyst Assembly. *J. Am. Chem. Soc.* **2013**, *135*, 2080−2083.

(7) Song, W.; Glasson, C. R. K.; Luo, H.; Hanson, K.; Brennaman, M. K.; Concepcion, J. J.; Meyer, T. J. Photoinduced Stepwise Oxidative Activation of a Chromophore−Catalyst Assembly on TiO_2. *J. Phys. Chem. Lett.* **2011**, *2*, 1808−1813.

(8) Wang, L.; Ashford, D. L.; Thompson, D. W.; Meyer, T. J.; Papanikolas, J. M. Watching Photoactivation in a Ru(II) Chromophore−Catalyst Assembly on TiO_2 by Ultrafast Spectroscopy. *J. Phys. Chem. C* **2013**, *117*, 24250−24258.

(9) Bettis, S. E.; Ryan, D. M.; Gish, M. K.; Alibabaei, L.; Meyer, T. J.; Waters, M. L.; Papanikolas, J. M. Photophysical Characterization of a Helical Peptide Chromophore−Water Oxidation Catalyst Assembly on a Semiconductor Surface Using Ultrafast Spectroscopy. *J. Phys. Chem. C* **2014**, *118*, 6029−6037.

(10) Hanson, K.; Torelli, D. A.; Vannucci, A. K.; Brennaman, M. K.; Luo, H.; Alibabaei, L.; Song, W.; Ashford, D. L.; Norris, M. R.; Glasson, C. R. K.; et al. Self-Assembled Bilayer Films of Ruthenium(II)/Polypyridyl Complexes through Layer-by-Layer Deposition on Nanostructured Metal Oxides. *Angew. Chem., Int. Ed.* **2012**, *51*, 12782−12785.

(11) Lee, H.; Kepley, L. J.; Hong, H. G.; Akhter, S.; Mallouk, T. E. Adsorption of Ordered Zirconium Phosphonate Multilayer Films on Silicon and Gold Surfaces. *J. Phys. Chem.* **1988**, *92*, 2597−2601.

(12) Lee, H.; Kepley, L. J.; Hong, H. G.; Mallouk, T. E. Inorganic Analogs of Langmuir−Blodgett Films: Adsorption of Ordered Zirconium 1,10-Decanebisphosphonate Multilayers on Silicon Surfaces. *J. Am. Chem. Soc.* **1988**, *110*, 618−620.

(13) Ishida, T.; Terada, K.; Hasegawa, K.; Kuwahata, H.; Kusama, K.; Sato, R.; Nakano, M.; Naitoh, Y.; Haga, M. Self-Assembled Monolayer and Multilayer Formation using Redox-Active Ru Complex with Phosphonic Acids on Silicon Oxide Surface. *Appl. Surf. Sci.* **2009**, *255*, 8824−8830.

(14) Terada, K.; Kobayashi, K.; Hikita, J.; Haga, M. Electric Conduction Properties of Self-Assembled Monolayer Films of Ru Complexes with Disulfide/Phosphonate Anchors in a Au−(Molecular Ensemble)−(Au Nanoparticle) Junction. *Chem. Lett.* **2009**, *38*, 416−417.

(15) Concepcion, J. J.; Jurss, J. W.; Brennaman, M. K.; Hoertz, P. G.; Patrocinio, A. O. v. T.; Murakami Iha, N. Y.; Templeton, J. L.; Meyer, T. J. Making Oxygen with Ruthenium Complexes. *Acc. Chem. Res.* **2009**, *42*, 1954−1965.

(16) Concepcion, J. J.; Jurss, J. W.; Templeton, J. L.; Meyer, T. J. One Site is Enough. Catalytic Water Oxidation by $[Ru(tpy)(bpm)(OH_2)]^{2+}$ and $[Ru(tpy)(bpz)(OH_2)]^{2+}$. *J. Am. Chem. Soc.* **2008**, *130*, 16462−16463.

(17) Concepcion, J. J.; Tsai, M.-K.; Muckerman, J. T.; Meyer, T. J. Mechanism of Water Oxidation by Single-Site Ruthenium Complex Catalysts. *J. Am. Chem. Soc.* **2010**, *132*, 1545−1557.

(18) Hanson, K.; Brennaman, M. K.; Ito, A.; Luo, H. L.; Song, W. J.; Parker, K. A.; Ghosh, R.; Norris, M. R.; Glasson, C. R. K.; Concepcion, J. J.; et al. Structure−Property Relationships in Phosphonate-Derivatized, Ru-II Polypyridyl Dyes on Metal Oxide Surfaces in an Aqueous Environment. *J. Phys. Chem. C* **2012**, *116*, 14837−14847.

(19) Kolle, U.; Moser, J.; Gratzel, M. Dynamics of Interfacial Charge-Transfer Reactions in Semiconductor Dispersions: Reduction of Cobaltoceniumdicarboxylate in Colloidal TiO_2. *Inorg. Chem.* **1985**, *24*, 2253−2258.

(20) Asbury, J. B.; Ellingson, R. J.; Ghosh, H. N.; Ferrere, S.; Nozik, A. J.; Lian, T. Femtosecond IR Study of Excited-State Relaxation and Electron-Injection Dynamics of $Ru(dcbpy)_2(NCS)_2$ in Solution and on Nanocrystalline TiO_2 and Al_2O_3 Thin Films. *J. Phys. Chem. B* **1999**, *103*, 3110−3119.

(21) Benkö, G.; Kallioinen, J.; Korppi-Tommola, J. E. I.; Yartsev, A. P.; Sundström, V. Photoinduced Ultrafast Dye-to-Semiconductor Electron Injection from Nonthermalized and Thermalized Donor States. *J. Am. Chem. Soc.* **2002**, *124*, 489−493.

(22) Myahkostupov, M.; Piotrowiak, P.; Wang, D.; Galoppini, E. Ru(II)−Bpy Complexes Bound to Nanocrystalline TiO_2 Films Through Phenyleneethynylene (Ope) Linkers: Effect of the Linkers Length on Electron Injection Rates. *J. Phys. Chem. C* **2007**, *111*, 2827−2829.

(23) Benkö, G.; Kallioinen, J.; Myllyperkiö, P.; Trif, F.; Korppi-Tommola, J. E. I.; Yartsev, A. P.; Sundström, V. Interligand Electron Transfer Determines Triplet Excited State Electron Injection in RuN_3-Sensitized TiO_2 Films. *J. Phys. Chem. B* **2004**, *108*, 2862−2867.

(24) Liu, F.; Meyer, G. J. Remote and Adjacent Excited-State Electron Transfer at TiO_2 Interfaces Sensitized to Visible Light with Ru(II) Compounds. *Inorg. Chem.* **2005**, *44*, 9305−9313.

(25) Schoonover, J. R.; Dattelbaum, D. M.; Malko, A.; Klimov, V. I.; Meyer, T. J.; Styers-Barnett, D. J.; Gannon, E. Z.; Granger, J. C.; Aldridge, W. S.; Papanikolas, J. M. Ultrafast Energy Transfer Between the ^{3}MLCT State of $[Ru^{II}(dmb)_2(bpy\text{-}An)]^{2+}$ and the Covalently Appended Anthracene. *J. Phys. Chem. A* **2005**, *109*, 2472−2475.

(26) Medlycott, E. A.; Hanan, G. S. Designing Tridentate Ligands for Ruthenium(II) Complexes with Prolonged Room Temperature Luminescence Lifetimes. *Chem. Soc. Rev.* **2005**, *34*, 133−142.

JACS
JOURNAL OF THE AMERICAN CHEMICAL SOCIETY

Communication

pubs.acs.org/JACS

Driving Force Dependent, Photoinduced Electron Transfer at Degenerately Doped, Optically Transparent Semiconductor Nanoparticle Interfaces

Byron H. Farnum, Zachary A. Morseth, M. Kyle Brennaman, John M. Papanikolas, and Thomas J. Meyer*

Department of Chemistry, University of North Carolina, Chapel Hill, North Carolina 27599-3290, United States

Supporting Information

ABSTRACT: Photoinduced, interfacial electron injection and back electron transfer between surface-bound $[Ru^{II}(bpy)_2(4,4'\text{-}(PO_3H_2)_2\text{-}bpy)]^{2+}$ and degenerately doped In_2O_3:Sn nanoparticles, present in mesoporous thin films (nanoITO), have been studied as a function of applied external bias. Due to the metallic behavior of the nanoITO films, application of an external bias was used to vary the Fermi level in the oxide and, with it, the driving force for electron transfer ($\Delta G^{o\prime}$). By controlling the external bias, $\Delta G^{o\prime}$ was varied from 0 to −1.8 eV for electron injection and from −0.3 to −1.3 eV for back electron transfer. Analysis of the back electron-transfer data, obtained from transient absorption measurements, using Marcus−Gerischer theory gave an experimental estimate of λ = 0.56 eV for the reorganization energy of the surface-bound $Ru^{III/II}$ couple in acetonitrile with 0.1 M $LiClO_4$ electrolyte.

Heterogeneous electron-transfer reactions initiated by visible light excitation of molecular chromophores surface bound to wide band gap semiconductor nanoparticles provide the basis for dye-sensitized solar energy conversion strategies.[1−3] For n-type metal oxides such as TiO_2, SnO_2, and ZnO, electron injection occurs by electron transfer from a molecular excited state to the conduction band of the semiconductor with rate constants typically in the range of 10^{10}−10^{12} s^{-1}.[4−7] Back electron transfer between the injected electron and oxidized chromophore is typically orders of magnitude slower, 10^3−10^6 s^{-1}.[6,8−11] Injection and back electron transfer are illustrated in eqs 1 and 2 for a generic n-type metal oxide (MO_x) and a prototypical Ru^{II}-polypyridyl chromophore. The difference in time scales for eqs 1 and 2 provides a basis for transient redox separation and applications in dye-sensitized solar cells and dye-sensitized photoelectrosynthesis cells.[1−3,12−15]

$$MO_x\text{−}Ru^{2+} \xrightarrow{h\nu} MO_x\text{−}Ru^{2+*} \rightarrow MO_x(e^-)\text{−}Ru^{3+} \quad (1)$$

$$MO_x(e^-)\text{−}Ru^{3+} \rightarrow MO_x\text{−}Ru^{2+} \quad (2)$$

Electron injection into nanostructured metal oxides, monitored by ultrafast transient absorption measurements, has been shown to be adequately described by Marcus−Gerischer theory.[4,6,16,17] Within this framework, the rate constant for interfacial electron transfer, dictated by the requirement for energy conservation, is determined by the energetic overlap of electronic levels in the semiconductor with the distribution of activation energies in the reacting molecule.[16−19] Similar success has not been realized for back electron transfer where there is limited evidence for a free-energy dependence.[20−22] Efforts in this area have been complicated by slow, complex electron-transfer kinetics at the interface believed to be the result of trap-state limited electron diffusion through the metal oxide nanostructures.[6,8,9,11,23,24]

Here we report the results of an investigation on photoinduced electron injection and back electron transfer for the surface-bound chromophore, $[Ru^{II}(bpy)_2(4,4'\text{-}(PO_3H_2)_2\text{-}bpy)]^{2+}$ (RuP^{2+}: bpy is 2,2′-bipyridine, Figure S2) on mesoporous In_2O_3:Sn nanoparticle films (nanoITO) by transient absorption spectroscopy. The results are novel in taking advantage of the metallic properties of the degenerately doped transparent conductive oxide (TCO) nanoparticles to avoid complications from electron diffusion in the oxide allowing a focus on the electron-transfer characteristics of a single-site, surface-bound molecule. Further, doping densities >10^{20} cm^{-3} allow for band bending of only a few nanometers at the nanoparticle surface such that the Fermi level at the nanoITO/solution interface can be controlled through an applied external bias.[25−27] This has allowed, heretofore, unprecedented experimental access to the driving force dependence of interfacial electron transfer for a single molecular site. The results are interpreted by application of Marcus−Gerischer theory which provides a direct estimate of the reorganization energy for the single-site, surface-bound $Ru^{III/II}$ redox couple.

Thin (3 μm) films of nanoITO were deposited on SnO_2:F (FTO) coated glass by a doctor blade technique from an ITO nanoparticle (10−20 nm diameter) dispersion. The resulting films were annealed under two different conditions: (1) 500 °C/1 h in air (oxidized; nanoITO(ox)) and (2) 500 °C/1 h in air followed by 300 °C/1 h under H_2(5%)/N_2 gas flow (reduced; nanoITO(red)). UV−vis near-IR absorbance spectral comparisons between the two materials revealed a noticeable blue shift in the localized surface plasmon resonance (LSPR) in the near-IR following the second, reductive annealing step, Figure S2. This feature has been noted elsewhere and arises from an increase in electron density for the reduced oxide.[27−32] The LSPR feature could be simulated by application of the standard Drude analysis giving estimated electron densities of N = 3.1 and 7.8 × 10^{20} cm^{-3} for oxidized and reduced nanoITO, respectively, Figure S2.[32,33]

Received: August 27, 2014
Published: October 20, 2014

   dx.doi.org/10.1021/ja508862h | J. Am. Chem. Soc. 2014, 136, 15869−15872

The band gap transition at $\lambda < 400$ nm was also found to be blue-shifted for reduced nanoITO with respect to oxidized films consistent with conduction band filling known as the Burstein–Moss effect.[34]

Oxidized and reduced nanoITO films were surface derivatized with RuP^{2+} by soaking overnight in methanol solutions with $[RuP](Cl)_2$ = 0.5 mM. Figure S1 shows UV–vis absorbance spectra of oxidized and reduced nanoITO–RuP^{2+} films recorded in acetonitrile (MeCN) with 0.1 M $LiClO_4$ electrolyte. Saturated surface coverages of $\Gamma = 3.1$ and 2.7×10^{-8} mol cm^{-2} for oxidized and reduced nanoITO, respectively, were estimated from UV–vis absorbance spectra. See Supporting Information for further details.[35]

Derivatized nanoITO–RuP^{2+} films were used as the working electrode in three-electrode spectroelectrochemical cells in order to monitor spectral changes on the ps–ns time scale by transient absorption measurements as a function of applied bias. A constant external bias, E_{app}, was applied to the nanoITO–RuP^{2+} electrode during the transient absorption experiment and varied in 0.2 V increments from 1.0 to −0.8 V vs SCE. Ohmic losses were small in the spectroelectrochemical cell, and the applied bias was assumed to define the equilibrated Fermi level (E_F) throughout the nanoITO film. The applied potential range was dictated by the reduction potentials for the metal-centered Ru^{III}/Ru^{II}, $E^{o\prime}(-RuP^{3+/2+})$ = 1.30 V vs SCE, and ligand-based $Ru^{II}(4,4'\text{-}(PO_3H_2)_2\text{-bpy})^{2+}/Ru^{II}(4,4'\text{-}(PO_3H_2)_2\text{-bpy}^{\bullet-})^{+}$), $E^{o\prime}(-RuP^{2+/+})$ = −1.53 V, couples to avoid background electrochemical reactions. Steady-state UV–vis spectra recorded before and after transient absorption measurements showed no sign of irreversible decomposition of the surface-bound chromophores.

Figure 1 illustrates representative transient absorbance difference spectra at the indicated delay times following 420 nm pulsed laser excitation (0.7 mJ cm^{-2}) of nanoITO(ox)–RuP^{2+} at E_{app} = 1.0 V. The features that appear in the transient spectra were general to both oxidized and reduced nanoITO and are consistent with loss of the characteristic, ground-state metal-to-ligand charge transfer (MLCT) absorption features in the visible due to formation of the excited state, $-RuP^{2+}*$. Appearance of the excited state was complete by 1 ps, followed by electron injection, eq 1, which occurred from 1 ps to 1 ns. Electron injection was monitored most directly by observing the change in ΔAbs signal at 375 nm where an initial positive $\pi \rightarrow \pi^*(4,4'\text{-}(PO_3H_2)_2\text{-bpy}^{\bullet-})$ absorption feature for the MLCT excited state decayed over time to yield ground-state bleach features representative of $-RuP^{3+}$ and nanoITO(e^-).[28] Back electron transfer between nanoITO(e^-) and $-RuP^{3+}$, eq 2, was observed on the ns–μs time scale during which the transient absorption features returned to the baseline with reformation of nanoITO–RuP^{2+}.

The time scale for electron injection was found to be highly dependent on the applied external bias. Figure S3 shows single wavelength ΔAbs traces at 375 nm as a function of E_{app} from 1.0 to −0.8 V for nanoITO(ox)–RuP^{2+}. As E_{app} was decreased, the time scale for $\Delta Abs_{375\ nm}$ decay increased from tens of picoseconds to hundreds of picoseconds consistent with slower electron injection. A potential dependence for injection is expected as the driving force was varied with applied bias where $\Delta G^{o\prime}_{inj} = -F(E_F - E^{o\prime}(RuP^{3+/2+}*))$, with F Faraday's constant, E_F (= E_{app}) the Fermi level in the oxide and $E^{o\prime}(RuP^{3+/2+}*)$ = −0.78 V vs SCE for the $-Ru^{III}(4,4'\text{-}(PO_3H_2)_2\text{-bpy})^{3+}/-Ru^{III}(4,4'\text{-}(PO_3H_2)_2\text{-bpy}^{\bullet-})^{2+}*$ couple. Based on the applied potentials, $\Delta G^{o\prime}_{inj}$ was calculated to vary from −1.8 to 0 eV.

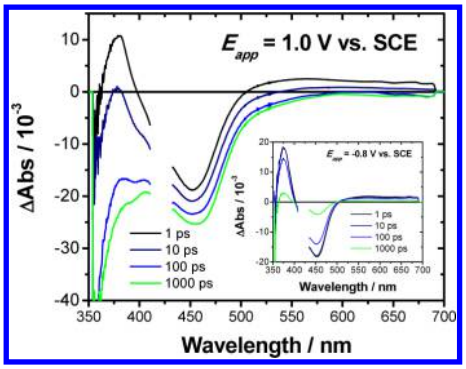

Figure 1. Transient absorbance difference spectra recorded at the indicated delay times for nanoITO(ox)–RuP^{2+} electrodes in MeCN (0.1 M $LiClO_4$) at E_{app} = 1.0 V vs SCE at room temperature. (inset) Transient absorption difference spectra recorded at E_{app} = −0.8 V for the same sample.

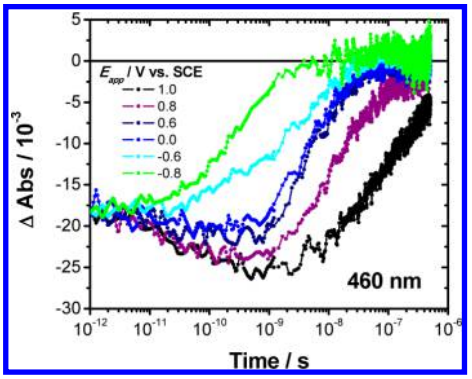

Figure 2. Single wavelength transient absorbance traces recorded at 460 nm as a function of E_{app} for nanoITO(ox)–RuP^{2+} in MeCN (0.1 M $LiClO_4$).

Beyond $E_{app} < -0.2$ V the formation of $-RuP^{3+}$ and nanoITO(e^-) was less evident in the transient spectra. At E_{app} = −0.8 V, the difference spectra were only characteristic of excited-state decay, Figure 1 inset. The kinetics for $-RuP^{2+}*$ decay under these conditions was found to be nearly first-order on both oxidized and reduced nanoITO with lifetimes of 380 and 290 ps, respectively. These values are notably decreased compared to the characteristic excited-state lifetime of 840 ns measured on the surface of the inert oxide ZrO_2 in MeCN (0.1 M $LiClO_4$) at room temperature, Figure S4. This observation points to participation by one or more additional pathways for excited state decay on nanoITO at $E_{app} < -0.2$ V. The origin of this effect is currently under investigation.

In the range E_{app} = 1.0–0 V, back electron transfer was monitored at 460 nm, Figure 2. At the most positive applied bias of 1.0 V the ΔAbs signal decreased over the first 1000 ps due to conversion from $-RuP^{2+}*$ to $-RuP^{3+}$ by electron injection. As shown in Figure 2, back electron transfer occurred on the ns–μs time scale with an obvious increase in rate as the applied bias was decreased from 1.0 to 0 V. Near E_{app} = 0 V, the rate of back electron transfer reached a bias-independent plateau. At more negative applied potentials complications appeared from incomplete electron injection and competing excited-state decay, as described above and shown in Figure 2 for E_{app} = −0.6 and −0.8 V, thus limiting analysis of the data to $E_{app} > 0$ V.

As is commonly observed at metal oxide interfaces, back electron-transfer kinetics were complex and nonexponential.[6,8,9,11] The data were analyzed as the characteristic time for

dx.doi.org/10.1021/ja508862h | J. Am. Chem. Soc. 2014, 136, 15869–15872

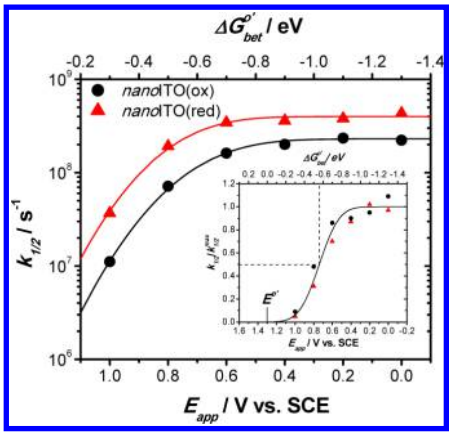

Figure 3. Back electron transfer rate constants reported as $k_{1/2}$ for $\Delta Abs_{460\ nm}$ decay as a function of E_{app} and $\Delta G^{o\prime}{}_{bet}$ for nanoITO(ox) (black circles) and nanoITO(red) (red triangles).

1/2 of the ΔAbs signal to decay to zero ($t_{1/2}$) or as the inverse rate constant, $k_{bet} = k_{1/2} = 1/t_{1/2}$.[10,20] Figure 3 shows values of $k_{1/2}$ for back electron transfer measured on oxidized and reduced nanoITO plotted versus E_{app}. These data illustrate that $k_{1/2}$ increased as E_{app} was varied from 1.0 to 0 V, reaching limiting values of $k_{1/2}{}^{max} = 2.3$ and $4.0 \times 10^8\ s^{-1}$ for oxidized and reduced nanoITO, respectively. As calculated from $\Delta G^{o\prime}{}_{bet} = -F(E^{o\prime}(RuP^{3+/2+}) - E_F)$ with $E^{o\prime}(RuP^{3+/2+}) = 1.30$ V vs SCE and $E_F = E_{app}$, the driving force for back electron transfer was varied from −0.3 to −1.3 eV.

The driving force dependence of back electron transfer was analyzed using Marcus−Gerischer theory, eq 3.[16−19] Here, $g(E)$ is the distribution of electronic levels in nanoITO as a function of energy, $f(E,E_F)$ is the Fermi function that describes the occupancy of electronic levels at energy E, $H_{ab}(E)$ is the electron-transfer coupling matrix element, and $W(E)$ is the Gaussian distribution of classical activation energies. From Marcus theory in the classical, harmonic limit, $W(E)$ is given by eq 4 where λ is the total reorganization energy, intramolecular (λ_i) plus solvent (λ_o), and $\Delta G(E)$ is the driving force for electron transfer at energy E.

$$k_{bet} = \frac{2\pi}{\hbar}\int_{-\infty}^{\infty} g(E)f(E, E_F)|H_{ab}(E)|^2 W(E)dE \quad (3)$$

$$W(E) = \frac{1}{\sqrt{4\pi\lambda kT}}\exp\left(\frac{-(\Delta G(E) + \lambda)^2}{4\lambda kT}\right) \quad (4)$$

The Marcus−Gerischer model differs from the standard Marcus approach in that electron transfer from nanoITO to $-RuP^{3+}$ occurs over the range of energy levels below the Fermi level (i.e., $E > E_F$) with each occurring isoenergetically.[17,19] Contributions from these levels are included in the overlap integral in eq 3 with the integral dominated by energies where both $g(E)$ and $W(E)$ are large. For metals, $g(E)$ is nearly constant over all E; however, for semiconductors, $g(E)$ is only large within the conduction and valence bands but is ∼0 within the band gap. Degenerately doped semiconductors such as nanoITO "bridge the gap" between metals and semiconductors by providing a large density of dopant levels within the band gap. Given the metallic behavior of nanoITO,[34,36] $g(E)$ was assumed to be constant with $g(E) \sim NV$ where N is the electron density and V is the volume of occupied electronic levels. With this assumption, eqs 3 and 4 simplify to eqs 5 and 6 for $k_{1/2}$ and $k_{1/2}{}^{max}$, respectively. In these equations $H_{ab}(E)$ is assumed to be constant, and the low temperature limit is assumed for $f(E, E_F)$. Based on eq 5, the driving force dependence of $k_{1/2}$ is governed by the integrated value of $W(E)$ for the $-RuP^{3+/2+}$ couple. This equation can be solved directly by integrating from E_F to ∞ to give eq 7 with $\Delta G^{o\prime}{}_{bet}$ defined previously.

$$k_{1/2} = k_{1/2}^{max}\int_{E_F}^{\infty} \frac{1}{\sqrt{4\pi\lambda kT}}\exp\left(\frac{-(\Delta G(E) + \lambda)^2}{4\lambda kT}\right)dE \quad (5)$$

$$k_{1/2}^{max} = \frac{2\pi}{\hbar}H_{ab}{}^2 NV \quad (6)$$

$$k_{1/2} = (k_{1/2}^{max}/2)\left[1 - \mathrm{erf}\left(\frac{\Delta G_{bet}^{o\prime} + \lambda}{2\sqrt{\lambda kT}}\right)\right] \quad (7)$$

Iterative fits of the data in Figure 3 to eq 7 with the $k_{1/2}{}^{max}$ values cited above resulted in $\lambda = 0.60$ and 0.52 eV for oxidized and reduced nanoITO, respectively, giving an average value of $\lambda = 0.56 \pm 0.04$ eV. This value for λ is close to values found for $[Ru(bpy)_3]^{3+/2+}$ self-exchange in aqueous solution with $\lambda = 0.4$[37] and 0.57[38] eV having been reported and attributed mainly to solvent reorganization (λ_o). Although not an overly sensitive probe, this result suggests that the solvent environment around the surface-bound $-RuP^{3+/2+}$ couple is comparable to fluid solution. This is in contrast to models for interfacial electron transfer that predict partial desolvation and decreases in λ_o compared to a fluid.[18,19]

A prediction of the Marcus−Gerischer model that follows from eq 7 is that at $-\Delta G^{o\prime}{}_{bet} = \lambda$, $k_{1/2} = k_{1/2}{}^{max}/2$ or $k_{bet} = k_{bet}{}^{max}/2$. This is in contrast to a reaction between discrete molecules in solution for which, $k = k^{max}$ at $-\Delta G^{o\prime} = \lambda$ and is a consequence of the contribution from multiple levels in the oxide below the Fermi level. The inset in Figure 3 shows the ratio $k_{1/2}/k_{1/2}{}^{max}$ plotted against both E_{app} and $\Delta G^{o\prime}{}_{bet}$ illustrating experimental verification of this prediction. The line overlaying the data was calculated from the ratio $k_{1/2}/k_{1/2}{}^{max}$ and eq 7 with $\lambda = 0.56$ eV. The condition, $-\Delta G^{o\prime}{}_{bet} = \lambda$, with $k_{1/2}/k_{1/2}{}^{max} = 0.5$ is indicated in the inset.

According to eq 6, the maximum rate constants for back electron transfer should be proportional to both N and H_{ab}. The experimental ratio $k_{1/2}{}^{max}(red)/k_{1/2}{}^{max}(ox) = 1.7$ is nearly equal to the ratio of electron densities, $N(red)/N(ox) = 2.5$, obtained by analysis of the near-IR LSPR feature mentioned above consistent with back electron transfer proportional to the electron density of the oxide. In terms of H_{ab}, it is notable that experimental values for the maximum rate constants for back electron transfer, $k_{1/2}{}^{max} = 2.3$ and $4.0 \times 10^8\ s^{-1}$, are relatively small and point to relatively weak electronic coupling to the nanoITO surface.

The photoinduced electron-transfer behavior observed for the nanoITO−RuP^{2+} electrodes is summarized in the Gerischer diagram in Scheme 1. It assumes a constant $g(E)$ for nanoITO with electron occupancy defined in the low-temperature limit such that filled levels exist at $E > E_F$ and unfilled levels at $E < E_F$. Although not explored in detail here, electron injection (k_{inj}) from the thermally equilibrated excited-state $-RuP^{2+*}$, is illustrated and depends on the overlap of unfilled levels in nanoITO with the excited-state distribution function $W_{Ru2+*}(E)$, defined by the reorganizational energy λ^* (purple dashed region).

As shown in the diagram and demonstrated here, back electron transfer (k_{bet}) depends on the overlap of filled levels in nanoITO

dx.doi.org/10.1021/ja508862h | J. Am. Chem. Soc. 2014, 136, 15869−15872

Scheme 1. Gerischer Diagram Depicting the Energetics Associated with Electron Injection by $-RuP^{2+}$* and Back Electron Transfer to $-RuP^{3+}$ (see text for further description)

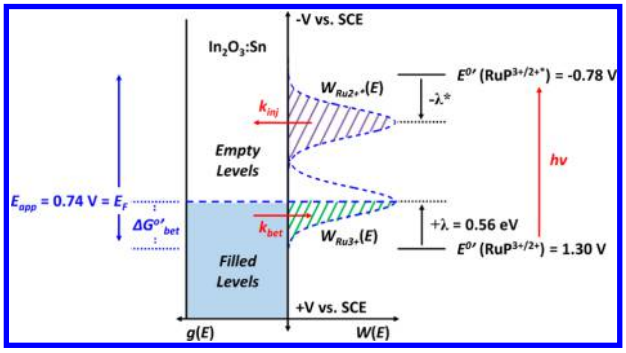

with the ground-state distribution function $W_{Ru3+}(E)$, defined by the reorganization energy λ (green dashed region). The special condition, $-\Delta G^{o'}{}_{bet} = \lambda$, is shown in the scheme at $E_{app} = E_F$ = 0.74 V vs SCE where half of the $W_{Ru3+}(E)$ Gaussian distribution function is overlapped with filled levels in the oxide leading to $k_{bet} = k_{bet}{}^{max}/2$, as discussed above.

The results reported here are important in demonstrating, for the first time, the use of a derivatized nanoTCO film to explore the role of driving force in interfacial, molecular electron-transfer kinetics over a range of nearly 2 eV. The ability to use an applied external bias to control driving force over a wide potential range is in contrast to intrinsic semiconductor nanoparticle films of the oxides TiO_2, SnO_2, and ZnO. For those oxides the range of applied biases is limited to the conduction band edge and above. The kinetic facility, optical transparency, and high density of electrons in nanoITO enable kinetic parameters to be obtained for single redox sites in contrast to solution measurements where two redox sites are required. The driving force dependence on the rate constant for back electron transfer was found to be consistent with Marcus−Gerischer theory with an average reorganization energy of λ = 0.56 ± 0.04 eV for the $Ru^{III/II}$ couple, comparable to values obtained from solution measurements for $[Ru(bpy)_3]^{3+/2+}$ self-exchange. Finally, the experimental protocols and analyses reported here are general, and we anticipate that the procedures described will find broad usage in characterizing interfacial electron-transfer reactions for a wide range of surface-bound molecules.

■ ASSOCIATED CONTENT

Supporting Information

Experimental details and additional figures. This material is available free of charge via the Internet at http://pubs.acs.org.

■ AUTHOR INFORMATION

Corresponding Author

tjmeyer@unc.edu

Notes

The authors declare no competing financial interest.

■ ACKNOWLEDGMENTS

This material is based upon work supported by the U.S. Department of Energy, Office of Science, Office of Basic Energy Sciences, under award no. DE-FG02-06ER15788.

■ REFERENCES

(1) Ardo, S.; Meyer, G. J. *Chem. Soc. Rev.* **2009**, *38*, 115.
(2) Gratzel, M. *Nature* **2001**, *414*, 338.
(3) Hagfeldt, A.; Boschloo, G.; Sun, L.; Kloo, L.; Pettersson, H. *Chem. Rev.* **2010**, *110*, 6595.
(4) Anderson, N. A.; Lian, T. *Annu. Rev. Phys. Chem.* **2005**, *56*, 491.
(5) Benkö, G.; Kallioinen, J.; Korppi-Tommola, J. E. I.; Yartsev, A. P.; Sundström, V. *J. Am. Chem. Soc.* **2002**, *124*, 489.
(6) Katoh, R.; Furube, A.; Barzykin, A. V.; Arakawa, H.; Tachiya, M. *Coord. Chem. Rev.* **2004**, *248*, 1195.
(7) Tachibana, Y.; Haque, S. A.; Mercer, I. P.; Moser, J. E.; Klug, D. R.; Durrant, J. R. *J. Phys. Chem. B* **2001**, *105*, 7424.
(8) Barzykin, A. V.; Tachiya, M. *J. Phys. Chem. B* **2002**, *106*, 4356.
(9) Nelson, J.; Haque, S.; Klug, D.; Durrant, J. *Phys. Rev. B* **2001**, *63*, 205321.
(10) Haque, S. A.; Tachibana, Y.; Klug, D. R.; Durrant, J. R. *J. Phys. Chem. B* **1998**, *102*, 1745.
(11) Bisquert, J. *J. Phys. Chem. C* **2007**, *111*, 17163.
(12) Youngblood, W. J.; Lee, S. A.; Kobayashi, Y.; Hernandez-pagan, E. A.; Hoertz, P. G.; Moore, T. A.; Moore, A. L.; Gust, D.; Mallouk, T. E. *J. Am. Chem. Soc.* **2009**, *131*, 926.
(13) Song, W.; Vannucci, A. K.; Farnum, B. H.; Lapides, A. M.; Brennaman, M. K.; Kalanyan, B.; Alibabaei, L.; Concepcion, J. J.; Losego, M. D.; Parsons, G. N.; Meyer, T. J. *J. Am. Chem. Soc.* **2014**, *136*, 9773.
(14) Gao, Y.; Ding, X.; Liu, J.; Wang, L.; Lu, Z.; Li, L.; Sun, L. *J. Am. Chem. Soc.* **2013**, *135*, 4219.
(15) Alibabaei, L.; Brennaman, M. K.; Norris, M. R.; Kalanyan, B.; Song, W.; Losego, M. D.; Concepcion, J. J.; Binstead, R. A.; Parsons, G. N.; Meyer, T. J. *Proc. Natl. Acad. Sci. U. S. A.* **2013**, *110*, 20008.
(16) Gerischer, H. *Photochem. Photobiol.* **1972**, *16*, 243.
(17) Gerischer, H.; Willig, F. *Top. Curr. Chem.* **1976**, *61*, 31.
(18) Marcus, R. A. *Annu. Rev. Phys. Chem.* **1964**, *15*, 155.
(19) Royea, W. J.; Fajardo, A. M.; Lewis, N. S. *J. Phys. Chem. B* **1997**, *101*, 11152.
(20) Clifford, J. N.; Palomares, E.; Nazeeruddin, K. M.; Gratzel, M.; Nelson, J.; Li, X.; Long, N. J.; Durrant, J. R. *J. Am. Chem. Soc.* **2004**, *126*, 5225.
(21) Moser, J. E.; Gratzel, M. *Chem. Phys.* **1993**, *176*, 493.
(22) Kuciauskas, D.; Freund, M. S.; Gray, H. B.; Winkler, J. R.; Lewis, N. S. *J. Phys. Chem. B* **2001**, *105*, 392.
(23) Nelson, J.; Chandler, R. E. *Coord. Chem. Rev.* **2004**, *248*, 1181.
(24) Nelson, J. *Phys. Rev. B* **1999**, *59*, 374.
(25) Albery, W. J.; Bartlett, P. N. *J. Electrochem. Soc.* **1984**, *131*, 315.
(26) Boschloo, G.; Fitzmaurice, D. *J. Phys. Chem. B* **1999**, *103*, 3093.
(27) Zum Felde, U.; Haase, M.; Weller, H. *J. Phys. Chem. B* **2000**, *104*, 9388.
(28) Farnum, B. H.; Morseth, Z. A.; Lapides, A. M.; Rieth, A. J.; Hoertz, P. G.; Brennaman, M. K.; Papanikolas, J. M.; Meyer, T. J. *J. Am. Chem. Soc.* **2014**, *136*, 2208.
(29) Garcia, G.; Buonsanti, R.; Runnerstrom, E. L.; Mendelsberg, R. J.; Llordes, A.; Anders, A.; Richardson, T. J.; Milliron, D. J. *Nano Lett.* **2011**, *11*, 4415.
(30) Llordés, A.; Garcia, G.; Gazquez, J.; Milliron, D. J. *Nature* **2013**, *500*, 323.
(31) Lounis, S. D.; Runnerstrom, E. L.; Bergerud, A.; Nordlund, D.; Milliron, D. J. *J. Am. Chem. Soc.* **2014**, *136*, 7110.
(32) Mendelsberg, R. J.; Garcia, G.; Li, H.; Manna, L.; Milliron, D. J. *J. Phys. Chem. C* **2012**, *116*, 1226.
(33) Nütz, T.; zum Felde, U.; Haase, M. *J. Chem. Phys.* **1999**, *110*, 12142.
(34) Hamberg, I.; Granqvist, C. G. *J. Appl. Phys.* **1986**, *60*, R123.
(35) Hanson, K.; Brennaman, M. K.; Ito, A.; Luo, H.; Song, W.; Parker, K. A.; Ghosh, R.; Norris, M. R.; Glasson, C. R. K.; Concepcion, J. J.; Lopez, R.; Meyer, T. J. *J. Phys. Chem. C* **2012**, *116*, 14837.
(36) Hoertz, P. G.; Chen, Z.; Kent, C. A.; Meyer, T. J. *Inorg. Chem.* **2010**, *49*, 8179.
(37) Young, R. C.; Keene, F. R.; Meyer, T. J. *J. Am. Chem. Soc.* **1977**, *99*, 2468.
(38) Sutin, N. *Acc. Chem. Res.* **1982**, *15*, 275.

JACS
JOURNAL OF THE AMERICAN CHEMICAL SOCIETY

Communication

pubs.acs.org/JACS

Photoinduced Interfacial Electron Transfer within a Mesoporous Transparent Conducting Oxide Film

Byron H. Farnum,[†] Zachary A. Morseth,[†] Alexander M. Lapides,[†] Adam J. Rieth,[‡] Paul G. Hoertz,[‡] M. Kyle Brennaman,[†] John M. Papanikolas,[†] and Thomas J. Meyer*[,†]

[†]Department of Chemistry, University of North Carolina, Chapel Hill, North Carolina 27599-3290, United States

[‡]RTI International, Research Triangle Park, North Carolina 27709-2194, United States

Supporting Information

ABSTRACT: Interfacial electron transfer to and from conductive Sn-doped In_2O_3 (ITO) nanoparticles (NPs) in mesoporous thin films has been investigated by transient absorption measurements using surface-bound $[Ru^{II}(bpy)_2(dcb)]^{2+}$ (bpy is 2,2′-bipyridyl and dcb is 4,4′-$(COOH)_2$-2,2′-bipyridyl). Metal-to-ligand charge transfer excitation in 0.1 M $LiClO_4$ MeCN results in efficient electron injection into the ITO NPs on the picosecond time scale followed by back electron transfer on the nanosecond time scale. Rates of back electron transfer are dependent on thermal annealing conditions with the rate constant increasing from 1.8×10^8 s^{-1} for oxidizing annealing conditions to 8.0×10^8 s^{-1} for reducing conditions, presumably due to an enhanced electron concentration in the latter.

Molecular photosensitization of high surface area, wide band gap semiconductor materials is a key element in photoelectrochemical approaches to solar energy conversion that yield electrical power or chemical fuels.[1−5] Improving our fundamental understanding of interfacial electron transfer reactions between molecular chromophores and semiconductor materials is therefore an important element in learning how to maximize performance in these systems.[2,6,7] We report here the dynamics of photoinduced, interfacial electron transfer following excitation of a Ru^{II} polypyridyl chromophore, surface-bound to nanoparticles (NPs) of the transparent conducting oxide Sn(IV)-doped In_2O_3 (ITO).

n-Type transparent conducting oxides (TCOs) are heavily doped, wide band gap semiconductors typically based on SnO_2, In_2O_3, or ZnO, whose optical transparency and conductivity have proven useful in a wide range of applications.[8−11] More recently, NP films of these materials have been prepared and characterized with mesoscopic structures analogous to NP films of TiO_2, SnO_2, and ZnO studied for dye-sensitized solar cell applications.[12−15] Their high effective surface areas and conductivities have allowed derivatized films to be used in both spectroelectrochemical and electrocatalytic applications.[7,13,16,17]

n-type TCOs are of interest in their own right as semiconductor materials with relatively high electron densities ($>10^{19}$ cm^{-3}). An investigation of interfacial electron transfer at TCO interfaces offers an interesting contrast to intrinsic metal oxide semiconductors (TiO_2, SnO_2, ZnO, WO_3, In_2O_3, Nb_2O_5, etc.).[2,4,18]

Defect oxygen vacancy states are expected to play an important role in these materials through their effect on back electron transfer. They are prevalent in metal oxide semiconductors and arise from under-coordinated metal ion sites in the bulk and at the surface of the crystal lattice.[19−21] In intrinsic semiconductors, they act as dopants which can lead to enhanced back electron transfer rates limiting the time scale for local charge separation and device efficiencies.[2,4,22]

In an earlier study on high surface area, conductive Sb-doped SnO_2 (ATO) electrodes, doping levels were controlled by varying the Sb dopant. An increase in back electron transfer rate was observed as the dopant concentration was increased.[23,24] In the current study, we have investigated both photoinjection and back electron transfer kinetics on ∼10 nm ITO NPs in mesoporous thin films (*nano*ITO). In this study, doping levels are controlled by varying the pretreatment of the oxide using either oxidative or reductive conditions with an influence on rates of back electron transfer by a factor of 4−5 and a potentially exploitable time window of ∼2 orders of magnitude between injection and recombination.

Mesoporous *nano*ITO thin films of 3 μm thickness were doctor bladed onto conductive FTO (fluorine-doped SnO_2) glass from a 10 wt % ITO NP suspension in hydroxypropyl cellulose/ethanol. Thin films were annealed in two steps: (1) 500 °C in air followed by (2) 300 °C under H_2/N_2 gas flow. SEM and TEM images revealed that the films were highly porous with an average NP size of 10 nm, Figure 1. Comparisons of UV−visible spectra after the first and second annealing steps revealed differences consistent with oxidation of the NPs (500 °C in air) followed by reduction (300 °C in H_2/N_2). Such thermal

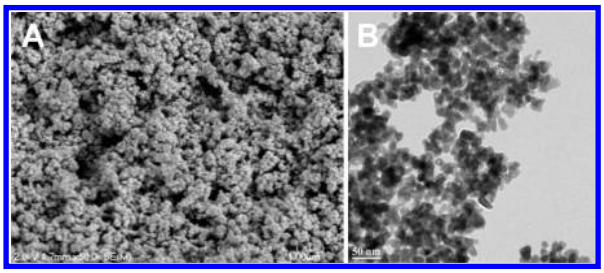

Figure 1. (A) SEM image of a high surface area *nano*ITO thin film. (B) TEM image of ITO NPs.

Received: October 17, 2013
Published: January 24, 2014

   dx.doi.org/10.1021/ja4106418 | *J. Am. Chem. Soc.* 2014, 136, 2208−2211

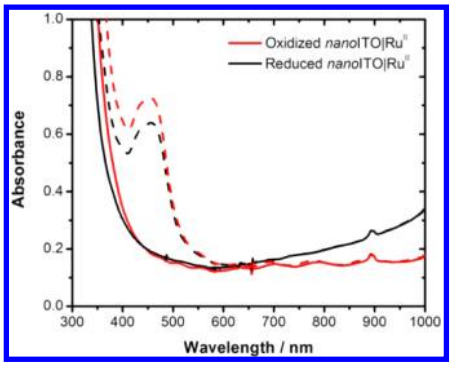

Figure 2. UV−visible spectra of 3 μm thick *nano*ITO films annealed under the oxidative and reductive conditions described in the text in 0.1 M $LiClO_4$ MeCN. Dashed lines show spectra of films derivatized with $[Ru^{II}(bpy)_2(dcb)]^{2+}$ at maximum surface loadings.

treatments of ITO thin films have been well documented in the literature.[20,25] In Figure 2, the narrow UV feature can be assigned to the optical band gap of ITO reported to be ∼3.5−3.8 eV.[19,26] A shift in the band gap upon thermal reduction from 3.7 to 3.8 eV can be assigned to a Burstein−Moss effect caused by an increase in the number of filled conduction band states.[21,26] Reduced *nano*ITO films also exhibited a higher energy localized surface plasmon resonance (LSPR), located in the near-IR at an onset of ∼800 nm, with respect to oxidized films. This feature has been well noted and arises from collective oscillations of free electrons in *nano*ITO.[27,28]

In order to explore the electrochemical properties of *nano*ITO, spectroelectrochemical measurements were conducted on films annealed under both oxidizing and reducing conditions. Thin films deposited on FTO glass were immersed in 0.1 M $LiClO_4$ MeCN solutions and connected as the working electrode in a three-electrode cell (details in Supporting Information). The external bias applied to the *nano*ITO films was varied from +2.0 to −1.0 V vs SCE, and UV−visible absorption spectra were recorded at 100 mV increments from 300 to 1000 nm, Figure S1. Spectral changes were observed over the entire potential range, in contrast to intrinsic semiconductors such as TiO_2 where spectral changes are only observed at applied potentials near the conduction band edge.[21]

Following application of the most positive applied potential at +2.0 V, a reverse, negative scan resulted in a shift of the optical band gap and the LSPR toward higher energies. Both features are consistent with an increase in electron density of the film and similar to changes observed after thermal reduction of *nano*ITO under H_2. At applied potentials more negative than 0 V vs SCE, a large increase in current flow resulted in an increase in absorbance from 400 to 600 nm, Figures S1−S2. This feature is tentatively assigned to an In(5s) → In(5p) interband transition that appears as the In(5s) conduction band is filled by reduction.[19]

*nano*ITO films were derivatized with $[Ru^{II}(bpy)_2(dcb)](PF_6)_2$ (Ru^{II}: bpy is 2,2′-bipyridine and dcb is 4,4′-$(CO_2H)_2$-2,2′-bipyridine), by soaking overnight in 1 mM acetonitrile solutions. Surface attachment through carboxylate linkages is a common method for derivatizing metal oxide NPs.[2,13] Langmuir binding isotherms for surface attachment gave equilibrium constants of 3.2×10^4 and 4.5×10^4 M^{-1} for oxidized and reduced *nano*ITO with maximum surface coverages of 3.6×10^{-8} and 3.0×10^{-8} mol/cm^2, respectively. UV−visible absorption spectra of the derivatized films are shown in Figure 2.

Transient absorption measurements on oxidized and reduced *nano*ITO|Ru^{II} on the picosecond time scale were used to monitor the dynamics of photoinduced electron injection into the ITO NPs. Laser excitation into the metal-to-ligand charge transfer (MLCT) absorption manifold of $[Ru^{II}(bpy)_2(dcb)]^{2+}$ at 420 nm (0.7 mJ/cm^2) in 0.1 M $LiClO_4$ MeCN resulted in transient spectral changes consistent with initial formation of the MLCT excited-state −Ru^{II}* (eq 1) followed by electron injection into *nano*ITO (eq 2). On a slower time scale back electron transfer to −Ru^{III} returned the film to *nano*ITO|Ru^{II} (eq 3).

$$nanoITO|Ru^{II} + h\nu \rightarrow nanoITO|Ru^{II}* \quad (1)$$

$$nanoITO|Ru^{II}* \rightarrow nanoITO(e^-)|Ru^{III} \quad (2)$$

$$nanoITO(e^-)|Ru^{III} \rightarrow nanoITO|Ru^{II} \quad (3)$$

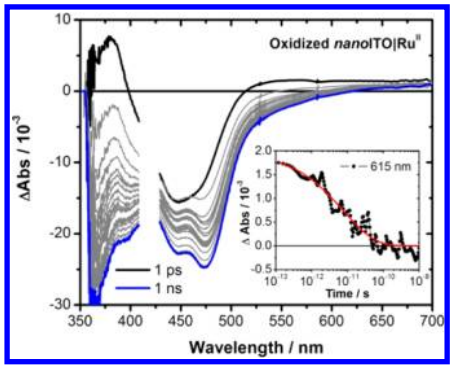

Figure 3. Transient absorption difference spectra following 420 nm laser excitation for an oxidized 3 μm *nano*ITO|Ru^{II} thin film in 0.1 M $LiClO_4$ MeCN at 22 °C. Inset shows the absorbance−time trace at 615 nm fit to eq 4 used in the kinetic analysis (see text).

Figures 3 and S3 show representative transient absorption difference spectra from 1 ps to 1 ns for oxidized and reduced *nano*ITO|Ru^{II} films, respectively, following 420 nm laser excitation. The initially formed −Ru^{II}* excited state was observed clearly at 1 ps. Isosbestic points appeared at 400 and 515 nm consistent with the transient difference spectrum of Ru^{II}* in homogeneous MeCN solution, Figure S4. In these spectra we note that the expected ΔAbs maximum arising from the $\pi^*(dcb^{\bullet-})$ absorption at 375 nm could not be fully resolved due to background *nano*ITO absorption.

Following excitation, excited-state electron injection into the ITO NPs occurred giving the interfacial redox-separated state *nano*ITO(e^-)|Ru^{III}. The conversion from −Ru^{II}* to −Ru^{III} was most easily monitored by loss of the characteristic $\pi^*(dcb^{\bullet-})$ feature at 375 nm and by a shift in the isosbestic point from 515 nm for Ru^{II}*/Ru^{II} to 615 nm for Ru^{III}/Ru^{II}.[29]

The change in absorbance at 615 nm was used to monitor the kinetics of electron injection, Figure 3 insets. Absorbance−time traces were nonexponential but could be satisfactorily fit to the Kolrausch−Williams−Watts (KWW) distribution function, eq 4, which gives a characteristic lifetime, τ, and distribution width, β.[30,31] Average electron injection rate constants were calculated as the first moment of the underlying Lévy distribution described by τ and β, eq 5.[30,31] The results from these fits are listed in Table 1 and gave $\langle k_{inj} \rangle = 6.4 \times 10^{10}$ and 8.4×10^{10} s^{-1} for oxidized and reduced *nano*ITO, respectively with injection 95% complete by 100 ps.

$$\Delta Abs = \Delta Abs_o \exp[-(t/\tau)^{\beta}] \quad (4)$$

dx.doi.org/10.1021/ja4106418 | J. Am. Chem. Soc. 2014, 136, 2208−2211

$$\left\langle k_{inj} \right\rangle = [(\tau/\beta)\Gamma(1/\beta)]^{-1} \quad (5)$$

Table 1. Photoinduced, Interfacial Electron Transfer Rate Constants for *nano*ITO|Ru^{II} in 0.1 M $LiClO_4$ MeCN

	oxidized[a]	reduced[b]
τ_{inj} (β)	7.8 ps (0.50)	4.8 ps (0.45)
$\langle k_{inj} \rangle$	6.4×10^{10} s^{-1}	8.4×10^{10} s^{-1}
τ_{bet} (β)	4.0 ns (0.63)	0.35 ns (0.39)
$\langle k_{bet} \rangle$	1.8×10^{8} s^{-1}	8.0×10^{8} s^{-1}

[a]500 °C/air. [b]500 °C/air + 300 °C/H_2/N_2; see text.

Additional features appeared in the transient difference spectra that were attributable to an increase in the electron density of *nano*ITO. The magnitude of a bleach feature from 350 to 400 nm in Figure 3 exceeded the absorbance change expected for $-Ru^{III}$ alone and appears to arise from a blue shift of the ITO band gap. This assignment is based on the appearance of related features in the spectroelectrochemical experiments described above and is consistent with a transient increase in the electron density of *nano*ITO due to injection by $-Ru^{II}$*. A second spectral marker was the appearance of a bleach maximum at 475 nm assigned to a Stark-like perturbation of ground-state $-Ru^{II}$ MLCT absorbers. Similar observations have been made at TiO_2 interfaces and arise from changes in the local electric field upon injection.[32−35] Independent analysis of the Stark effect on *nano*ITO|Ru^{II} by Li^+ titrations in MeCN revealed an identical bleach maximum at 475 nm, Figure S5.

Figure 4 provides a comparison between experimental data obtained at 1 ns for oxidized *nano*ITO|Ru^{II} and simulated spectra

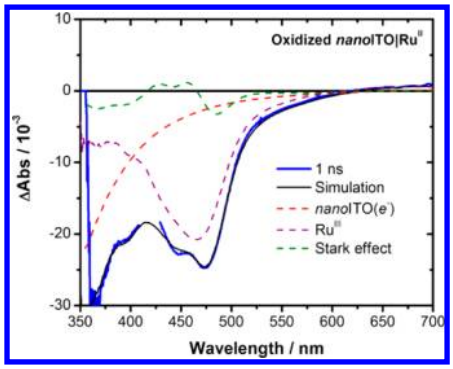

Figure 4. Experimental transient absorption difference spectra obtained at 1 ns (blue) for oxidized *nano*ITO|Ru^{II} in 0.1 M $LiClO_4$ MeCN at 22 °C compared with a simulated spectra (black). The simulation was obtained by a linear summation of known difference spectra for *nano*ITO(e^-) (red dash), -Ru^{III} (purple dash), and the Stark effect (green dash).

modeled by using known difference spectra for $-Ru^{III}$, *nano*ITO(e^-), and the Stark effect. The agreement between the experimental and simulated data in Figure 4 is excellent, providing strong evidence that excited-state electron injection from $-Ru^{II}$* yields $-Ru^{III}$, *nano*ITO(e^-), and a Stark effect.

Spectral simulations over a range of delay times revealed that the dynamic loss of $-Ru^{II}$* and growth of $-Ru^{III}$ were matched by those for the appearance of both *nano*ITO(e^-) and the Stark effect, Figure S6. These results agree with recent reports on the transient growth of Stark effects on TiO_2 over the femtosecond to picosecond time scales which correlated with the time dependence of electron injection.[36,37] As the electron density in/on the ITO NPs changes, the local electric field sensed by the $-Ru^{II}$ chromophore changes resulting in the observed spectral shifts.

Injection yields measured at 1 ns for oxidized and reduced *nano*ITO were 99% and 78%, respectively. Given similar $\langle k_{inj} \rangle$ values between the two films, the lower apparent injection yield for reduced *nano*ITO must arise from a rapid *nano*ITO(e^-) → $-Ru^{III}$ back electron transfer component occurring on the time scale for injection or by an additional quenching mechanism at the surface of reduced *nano*ITO.

Back electron transfer was investigated by transient absorption measurements on the nanoseconds time scale. From these measurements the decay of spectral features for $-Ru^{III}$, *nano*ITO(e^-), and the Stark effect occurred on the same time scale. This allowed for back electron transfer kinetics to be monitored independently of wavelength. Figure 5 shows

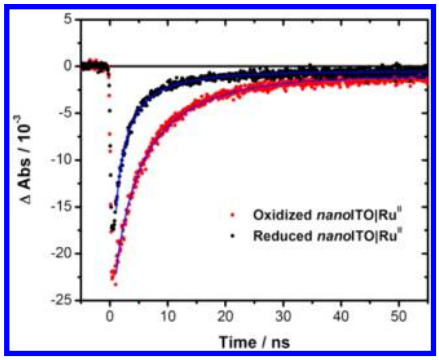

Figure 5. Nanosecond absorbance−time traces at 475 nm for *nano*ITO(e^-)|Ru^{III} → *nano*ITO|Ru^{II} back electron transfer on oxidized and reduced *nano*ITO in 0.1 M $LiClO_4$ MeCN at 22 °C. Data were fit to the KWW distribution function in eq 4.

absorbance−time traces at 475 nm for both oxidized and reduced *nano*ITO|Ru^{II}. Back electron transfer kinetics at reduced *nano*ITO were noticeably faster than at oxidized *nano*ITO. Application of eqs 4−5, but for back electron transfer, gave $\langle k_{bet} \rangle$ = 1.8×10^8 and 8.0×10^8 s^{-1} for oxidized and reduced *nano*ITO, respectively.

The role of the thermodynamics for excited-state injection and back electron transfer for *nano*ITO|Ru^{II} are of interest in comparison with related wide band gap metal oxides. The Fermi level for ITO should be at or near its conduction band edge, −0.2 V vs SCE, depending on the degree of *n*-doping.[38] This value is in the same range as the conduction band edges for TiO_2 (−0.4 V), SnO_2 (0.1 V), and ZnO (−0.4 V) under comparable conditions.[18,21] Based on the exited-state reduction potential $E^{\circ\prime}(Ru^{III/II*})$ = −1.16 V vs SCE, oxidative quenching is highly favored for the series of semiconductors with $\Delta G^{\circ\prime}$ varying from −0.8 to −1.3 eV resulting in $k_{inj} > 10^{10}$ s^{-1} throughout the series.[18,39]

By contrast, there is a significant difference in the time scale for back electron transfer which ranges from nanoseconds on *nano*ITO to microseconds and milliseconds on TiO_2, SnO_2, and ZnO. As mentioned above, in mesoscopic ATO films higher *n*-doping leads to faster back electron transfer due to the higher electron density in the doped metal oxide.[23,24] Electron densities of ~10^{20} cm^{-3} for ITO NPs presumably play a similar role in back electron transfer kinetics.[27,28]

A notable finding in our results is the influence of thermal treatment of *nano*ITO on back electron transfer kinetics. The

dx.doi.org/10.1021/ja4106418 | J. Am. Chem. Soc. 2014, 136, 2208−2211

microscopic origin of these effects under reducing conditions has been attributed to the creation of oxygen vacancy states arising from In and Sn atoms adjacent to empty O atom sites in the ITO lattice.[19,40] The influence of oxygen vacancy states on bulk electron transport and interfacial electron transfer has been noted in other metal oxides including TiO_2 and SnO_2 NP thin films.[2,4,21,22] Thermal treatment with oxygen or hydrogen modifies the density of oxygen vacancy states by inserting (oxidized *nano*ITO) or removing (reduced *nano*ITO) oxygen atoms from the lattice.[20,25] For back electron transfer, decreasing the density of oxygen vacancies by treatment with O_2 resulted in a factor of 4−5 decrease in $\langle k_{bet} \rangle$.

In summary, our kinetic studies demonstrate rapid, efficient electron injection by $[Ru^{II}(bpy)_2(dcb)]^{2+*}$ on the surfaces of *nano*ITO films. Injection occurs with $k_{inj} = (6-9) \times 10^{10}$ s^{-1} in 0.1 M $LiClO_4$ MeCN with a maximum injection efficiency of 99% for oxidized *nano*ITO and 78% for reduced *nano*ITO. Back electron transfer is also rapid ($k_{bet} > 10^8$ s^{-1}) due to the high electron density of the doped metal oxide material and is dependent on the density of oxygen vacancy sites.

The results of the dynamics study are important in revealing efficient electron injection and a potentially exploitable time window of ∼2 orders of magnitude between injection and recombination. We are currently investigating the possible exploitation of this window in driving net chemical reactions and the effects of applied potential on both injection and back electron transfer. The latter is of particular interest since, in contrast to TiO_2 or SnO_2, the Fermi level and, presumably, interfacial dynamics can be controlled by application of an external bias.

■ ASSOCIATED CONTENT

Supporting Information

Experimental details, spectroelectrochemical and Stark effect UV-visible spectra, and injection kinetics. This material is available free of charge via the Internet at http://pubs.acs.org.

■ AUTHOR INFORMATION

Corresponding Author

*tjmeyer@unc.edu

Notes

The authors declare no competing financial interest.

■ ACKNOWLEDGMENTS

B.H.F. acknowledges support from the U.S. Department of Energy, Office of Science, Office of Basic Energy Sciences, under Award No. DE-FG02-06ER15788. Z.A.M., A.J.R., P.G.H., and M.K.B. acknowledge support from the UNC EFRC: Center for Solar Fuels, an Energy Frontier Research Center funded by the U.S. Department of Energy, Office of Basic Energy Sciences under Award No. DE-SC0001011. A.M.L. acknowledges support from the Department of Defense, Air Force Office of Scientific Research, National Defense Science and Engineering Graduate (NDSEG) Fellowship, 32 CFR 168a, under Award No. FA9550-11-C-0028. B.H.F. would also like to thank Dr. Amar Kumbhar for assistance in TEM measurements.

■ REFERENCES

(1) Alstrum-Acevedo, J. H.; Brennaman, M. K.; Meyer, T. J. *Inorg. Chem.* **2005**, *44*, 6802.
(2) Ardo, S.; Meyer, G. J. *Chem. Soc. Rev.* **2009**, *38*, 115.
(3) Bard, A. J.; Fox, M. A. *Acc. Chem. Res.* **1995**, *28*, 141.
(4) Hagfeldt, A.; Boschloo, G.; Sun, L.; Kloo, L.; Pettersson, H. *Chem. Rev.* **2010**, *110*, 6595.
(5) O'Regan, B.; Gratzel, M. *Nature* **1991**, *353*, 737.
(6) Ashford, D. L.; Song, W.; Concepcion, J. J.; Glasson, C. R. K.; Brennaman, M. K.; Norris, M. R.; Fang, Z.; Templeton, J. L.; Meyer, T. J. *J. Am. Chem. Soc.* **2012**, *134*, 19189.
(7) Song, W.; Ito, A.; Binstead, R. A.; Hanson, K.; Luo, H.; Brennaman, M. K.; Concepcion, J. J.; Meyer, T. J. *J. Am. Chem. Soc.* **2013**, *135*, 11587.
(8) Chopra, K. L.; Major, S.; Pandya, D. K. *Thin Solid Films* **1983**, *102*, 1.
(9) Ellmer, K. *Nat. Photonics* **2012**, *6*, 809.
(10) Llordes, A.; Garcia, G.; Gazquez, J.; Milliron, D. J. *Nature* **2013**, *500*, 323.
(11) Robertson, J.; Falabretti, B. In *Handbook of Transparent Conductors*; Ginley, D. S., Ed.; Springer Science + Business Media: New York, 2010.
(12) Biancardo, M.; Argazzi, R.; Bignozzi, C. A. *Displays* **2006**, *27*, 19.
(13) Hoertz, P. G.; Chen, Z.; Kent, C. A.; Meyer, T. J. *Inorg. Chem.* **2010**, *49*, 8179.
(14) Hou, K.; Puzzo, D.; Helander, M. G.; Lo, S. S.; Bonifacio, L. D.; Wang, W.; Lu, Z.; Scholes, G. D.; Ozin, G. A. *Adv. Mater.* **2009**, *21*, 2492.
(15) Schwab, P. F. H.; Diegoli, S.; Biancardo, M.; Bignozzi, C. A. *Inorg. Chem.* **2003**, *42*, 6613.
(16) Chen, Z.; Concepcion, J. J.; Jurss, J. W.; Meyer, T. J. *J. Am. Chem. Soc.* **2009**, *131*, 15580.
(17) Chen, Z.; Concepcion, J. J.; Luo, H.; Hull, J. F.; Paul, A.; Meyer, T. J. *J. Am. Chem. Soc.* **2010**, *132*, 17670.
(18) Anderson, N. A.; Lian, T. *Annu. Rev. Phys. Chem.* **2005**, *56*, 491.
(19) Fan, J. C. C.; Goodenough, J. B. *J. Appl. Phys.* **1977**, *48*, 3524.
(20) Frank, G.; Kostlin, H. *Appl. Phys. A: Mater. Sci. Process.* **1982**, *27*, 197.
(21) Rothenberger, G.; Fitzmaurice, D.; Gratzel, M. *J. Phys. Chem.* **1992**, *96*, 5983.
(22) Prasittichai, C.; Hupp, J. T. *J. Phys. Chem. Lett.* **2010**, *1*, 1611.
(23) Guo, J.; She, C.; Lian, T. *J. Phys. Chem. B* **2005**, *109*, 7095.
(24) Guo, J.; She, C.; Lian, T. *J. Phys. Chem. C* **2008**, *112*, 4761.
(25) Hamberg, I.; Granqvist, C. G. *J. Appl. Phys.* **1986**, *60*, R123.
(26) Kim, H.; Gilmore, C. M.; Pique, A.; Horwitz, J. S.; Mattoussi, H.; Murata, H.; Kafafi, Z. H.; Chrisey, D. B. *J. Appl. Phys.* **1999**, *86*, 6451.
(27) Garcia, G.; Buonsanti, R.; Runnerstrom, E. L.; Mendelsberg, R. J.; Llordes, A.; Anders, A.; Richarson, T. J.; Milliron, D. J. *Nano Lett.* **2011**, *11*, 4415.
(28) Mendelsberg, R. J.; Garcia, G.; Li, H.; Manna, L.; Milliron, D. J. *J. Phys. Chem. C* **2012**, *116*, 12226.
(29) Juris, A.; Balzani, V.; Barigelletti, F.; Campagna, S.; Belser, P.; Von Zelewsky, A. *Coord. Chem. Rev.* **1988**, *84*, 85.
(30) Lindsey, C. P.; Patterson, G. D. *J. Chem. Phys.* **1980**, *73*, 3348.
(31) Williams, G.; Watts, D. C. *Trans. Faraday Soc.* **1970**, *66*, 80.
(32) Anderson, A. Y.; Barnes, P. R. F.; Durrant, J. R.; O'Regan, B. C. *J. Phys. Chem. C* **2010**, *114*, 1953.
(33) Ardo, S.; Sun, L.; Castellano, F. N.; Meyer, G. J. *J. Phys. Chem. B* **2010**, *114*, 14596.
(34) Ardo, S.; Sun, L.; Staniszewski, A.; Castellano, F. N.; Meyer, G. J. *J. Am. Chem. Soc.* **2010**, *132*, 6696.
(35) O'Donnell, R. M.; Ardo, S.; Meyer, G. J. *J. Phys. Chem. Lett.* **2013**, *4*, 2817.
(36) Bairu, S.; Mghanga, E.; Hasan, J.; Kola, S.; Rao, V. J.; Bhanuprakash, K.; Giribabu, L.; Wiederrecht, G. P.; da Silva, R.; Rego, L. G. C.; Ramakrishna, G. *J. Phys. Chem. C* **2013**, *117*, 4824.
(37) Meister, M.; Baumeier, B.; Pschirer, N.; Sens, R.; Bruder, I.; Laquai, F.; Andrienko, D.; Howard, I. A. *J. Phys. Chem. C* **2013**, *117*, 9171.
(38) Hotchkiss, P. J.; Jones, S. C.; Paniagua, S. A.; Sharma, A.; Kippelen, B.; Armstrong, N. R.; Marder, S. R. *Acc. Chem. Res.* **2012**, *45*, 337.
(39) Vinodgopal, K.; Hua, X.; Dahlgren, R. L.; Lappin, A. G.; Patterson, L. K.; Kamat, P. V. *J. Phys. Chem.* **1995**, *99*, 10883.
(40) Gassenbauer, Y.; Klein, A. *J. Phys. Chem. B* **2006**, *110*, 4793.

JACS
JOURNAL OF THE AMERICAN CHEMICAL SOCIETY

Communication

pubs.acs.org/JACS

Interfacial Energy Conversion in Ru^{II} Polypyridyl-Derivatized Oligoproline Assemblies on TiO_2

Da Ma,[†,§] Stephanie E. Bettis,[†,§] Kenneth Hanson,[†] Maria Minakova,[‡] Leila Alibabaei,[†] William Fondrie,[†] Derek M. Ryan,[†] Garegin A. Papoian,[‡] Thomas J. Meyer,[†] Marcey L. Waters,*[,†] and John M. Papanikolas*[,†]

[†]Department of Chemistry, CB 3290, University of North Carolina, Chapel Hill, North Carolina 27599, United States

[‡]Department of Chemistry and Biochemistry, University of Maryland, College Park, Maryland 20742, United States

Supporting Information

ABSTRACT: Solid-phase peptide synthesis has been applied to the preparation of phosphonate-derivatized oligoproline assemblies containing two different Ru^{II} polypyridyl chromophores coupled via "click" chemistry. In water or methanol the assembly adopts the polyproline II (PPII) helical structure, which brings the chromophores into close contact. Excitation of the assembly on ZrO_2 at the outer Ru^{II} in 0.1 M $HClO_4$ at 25 °C is followed by rapid, efficient intra-assembly energy transfer to the inner Ru^{II} (k_{EnT} = 3.0 × 10^7 s^{-1}, implying 96% relative efficiency). The comparable energy transfer rate constants in solution and on nanocrystalline ZrO_2 suggest that the PPII structure is retained when bound to ZrO_2. On nanocrystalline films of TiO_2, excitation at the inner Ru^{II} is followed by rapid, efficient injection into TiO_2. Excitation of the outer Ru^{II} is followed by rapid intra-assembly energy transfer and then by electron injection. The oligoproline/click chemistry approach holds great promise for the preparation of interfacial assemblies for energy conversion based on a family of assemblies having controlled compositions and distances between key functional groups.

Molecular structure and organization are key elements in molecular-level energy conversion. An object lesson is photosystem II in natural photosynthesis where light-driven oxidation of water occurs. Absorption of light in an antenna complex drives a sequence of five electron transfer reactions resulting in oxidative activation of the oxygen evolving complex and delivery of a reductive equivalent, as the semiquinone form of plastoquinone, separated by a distance of ~50 Å.[1,2]

At the heart of PSII is a structurally controlled array of light absorbers, electron transfer relays, and catalysts in the thylakoid membranes of chloroplasts. Mimicking these features, both in content and relative orientation, in an artificial device poses a significant synthetic challenge. We report here a systematic strategy based on solid-phase peptide synthesis (SPPS) combined with the copper catalyzed azide–alkyne cycloaddition (CuAAC or 'click' reaction) for modular synthesis of a spatially preorganized bichromophoric assembly.[3] This strategy has been applied to the preparation of an interfacial assembly for photochemical electron and energy transfer when bound in nanocrystalline films of TiO_2.

A number of strategies have been explored for the preparation of light harvesting assemblies including porphyrin arrays,[4] polymers,[5] DNA,[6] dendrimers,[7] metal–organic frameworks,[8] and molecular assemblies.[9] For interfacial applications, as in dye-sensitized solar cells (DSSC)[10] or dye-sensitized photoelectrosynthesis cells,[11] it is important to combine broad visible to near IR absorption with directional control of energy and electron transfer toward the semiconductor interface. Several examples of surface-bound assemblies have been discussed in the context of DSSCs[12] but lack detailed kinetic analysis of the excited-state photophysics.

Controlling the direction of electron and energy transfer requires the control of chromophore positioning and orientation relative to the surface as well as the ability to incorporate different chromophores at specific positions. Peptides are useful as molecular scaffolds for multiple functional units due to the ability to encode highly ordered secondary and tertiary structures based on their amino acid sequence. Oligoprolines with at least five proline residues are particularly notable in this regard because they form left-handed polyproline II (PPII) helices in polar solvents, providing a rigid scaffold for positioning multiple chromophores.[13] Additionally, SPPS allows for absolute control of the positioning of functional groups. With application of 'click' coupling, the amino acid sequence can be modified systematically with assembly structures by incorporating the appropriate functional groups (i.e., azide or alkyne) at specific locations in the peptide sequence.[3] This offers the additional advantage of incorporating molecular components with different functionalities (e.g., light-harvesting chromophores and molecular catalysts for water splitting) with a high degree of structural control.

The well-defined structural characteristics of oligoprolines[14] and other peptide scaffolds[15] have been exploited previously to investigate the distance dependence of electron and energy transfer in Ru^{II}-bpy modified derivatives. Herein, we report the design and synthesis of an oligoproline assembly containing two different chromophores on the surface of nanostructured films of TiO_2 and application of ultrafast transient spectro-

Received: January 7, 2013
Published: March 20, 2013

   dx.doi.org/10.1021/ja312143h | *J. Am. Chem. Soc.* 2013, 135, 5250–5253

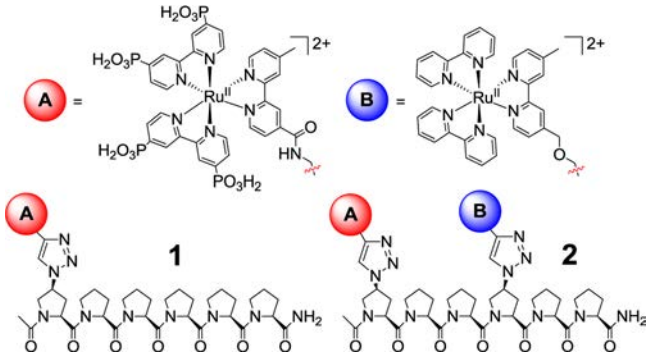

Figure 1. Structure of **1** and **2**.

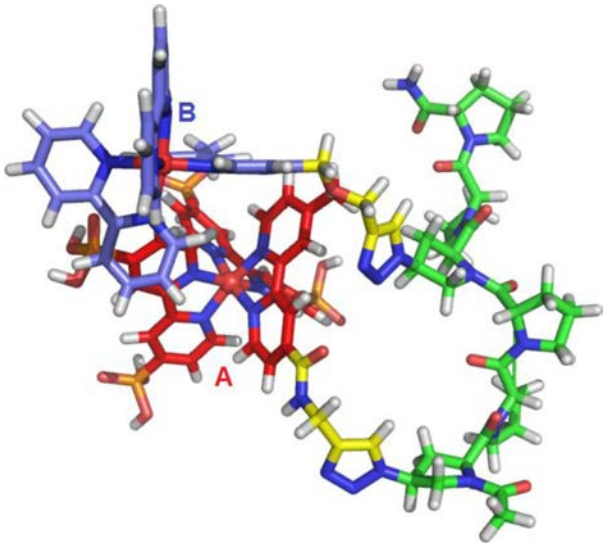

Figure 2. All-atom molecular dynamics simulation of **2** in solution showing the Ru^{II} chromophores in close contact. Green indicates oligoproline backbone, yellow indicates linkers, red indicates chromophore **A**, and blue indicates chromophore **B**.

scopic measurements to demonstrate and evaluate intra-assembly energy transfer and excited-state injection.

Two peptide-chromophore assemblies were investigated: Assembly **1** is a control compound containing only the inner chromophore **A**, which will bind directly to the surface, whereas assembly **2** contains both an inner and outer chromophore, **A** and **B**, respectively (Figure 1). The design of structure **2** was guided by: (1) having six proline residues to induce helical secondary structure; (2) including a Ru^{II} polypyridyl complex with phosphonate-derivatized bipyridine ligands for binding to metal oxide surfaces;[16] (3) using a two-proline spacer unit between the Ru^{II} chromophores, which in the PPII helix (Figure 2), aligns the two chromophores on the same side of the helix and minimizes their internuclear separation distance; (4) incorporating Ru^{II} chromophores with MLCT excited states "tuned" to create an energy transfer gradient toward the interface. Although subtle, the latter feature is present in **2** because of the electronic effects of the substituents on the π^* acceptor levels in the MLCT excited states of **A**. The unfunctionalized bpy ligands in **B** form an excited state that is slightly higher in energy than the functionalized ligands on **A**.

Assembly **1** was synthesized via SPPS with 4*S*-azido-L-proline coupled at the N-terminal position, followed by capping, cleavage from the resin, and subsequent solution-phase CuAAC to attach **A**. For **2**, the peptide was synthesized via SPPS up to the interior azidoproline at position 4, followed by on-bead CuAAC to attach **B**. SPPS was then continued to complete the peptide with azidoproline at the N-terminus and **A** was attached as for **1**. In this way, two different chromophores were attached in a position-dependent manner using the same coupling reaction without the use of orthogonal protecting group chemistry.

In water, at pH = 1.0, 4.0, and 7.4 or in MeOH, **2** exhibits left-handed PPII helical structure as indicated by circular dichroism (Figure S1). Molecular dynamics simulations support the formation of a PPII helical conformation (Figure 2) with the chromophores in close contact and an average Ru–Ru spacing of 13 Å (see SI).

The assemblies were loaded onto 3 μm thick, nanocrystalline (20 nm particles) films of TiO_2 or ZrO_2 by soaking the films overnight in a 150 μM solution of the peptide in aqueous 0.1 M $HClO_4$. Surface coverage was estimated by UV–visible measurements (Figure S6). Relative to $[Ru^{II}(bpy)_2(4,4'\text{-}(PO_3H_2)_2(bpy))]^{2+}$ (**RuP**), which exhibits full surface coverage[17] with $\Gamma = 8.6 \times 10^{-8}$ mol/cm^2 (2.9×10^{-8} mol/cm^2/μm), assemblies **1** and **2** have nearly full surface coverage with $\Gamma = 7.9 \times 10^{-8}$ mol/cm^2 and 7.1×10^{-8} mol/cm^2, respectively.

The dynamic events anticipated to occur following transient excitation of **2** on TiO_2 are illustrated in Scheme 1. Photon

Scheme 1. Schematic Representation of Photophysical Events of 2 on Nanocrystalline TiO_2

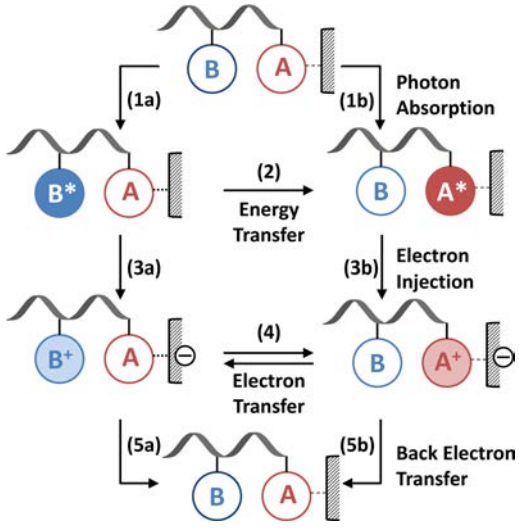

absorption can occur at either **A** or **B**. Photoexcitation at the **A** is expected to result in rapid electron injection into TiO_2 as observed for **RuP** on TiO_2 (Scheme 1, eq 1b).[17] Deactivation of **B*** can occur either by energy transfer to **A** (eq 2) followed by electron injection from **A*** (eq 3b) or by remote injection from **B*** (eq 3a). Following electron injection, electron transfer from **B** to A^+ (eq 4) is energetically favorable by ~130 mV as indicated by electrochemical measurements. Ultimately the electron in TiO_2 will recombine with the oxidized complex (A^+ or B^+) through back electron transfer (eq 5).

The energy transfer dynamics of **2** (Scheme 1, eq 2) were investigated by time-resolved emission measurements in aqueous 0.1 M $HClO_4$ at rt on the nanosecond time scale both in solution and on nanocrystalline ZrO_2 (where electron injection does not occur). As shown in Figure S7, excitation of

dx.doi.org/10.1021/ja312143h | J. Am. Chem. Soc. 2013, 135, 5250–5253

2 in solution and on ZrO_2 at 450 nm results in ^{3}MLCT emission with a time-dependent shift in the emission maximum from 630 to 645 nm. These observations are consistent with excitation of **B** (eq 1a) followed by intra-assembly energy transfer to **A**, (eq 2), which is favored by 70 meV (Figure S5). Analysis of the time-dependent emission data by application of model free global analysis resulted in τ_{EnT} = 31 ns in solution and τ_{EnT} = 33 ns on ZrO_2 (Figures S8–9 and Tables S1–2). The comparable energy transfer rate constants in solution and on nanocrystalline ZrO_2 suggest that the secondary structure of the oligoproline assembly is retained on the surface of ZrO_2.

Electron injection kinetics from **1*** and **2*** into nanocrystalline TiO_2 were measured by transient absorption spectroscopy (Supporting Information). In transient absorption difference spectra, obtained 600 fs after excitation at 475 nm, Figure 3,

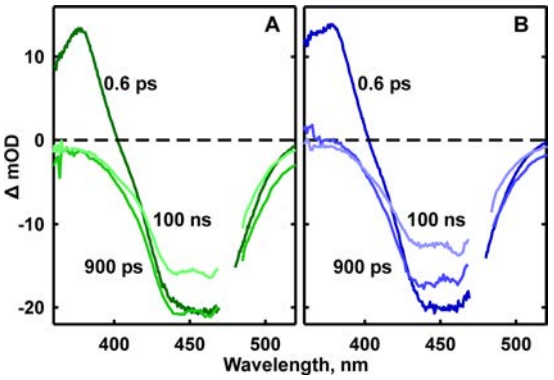

Figure 3. Transient absorption spectra of (a) **1** and (b) **2** at 0.6 ps (dark line), 900 ps (medium line), and 100 ns (light line) after laser excitation. Both samples were on 3 μm thick nanocrystalline TiO_2 film in aqueous 0.1 M $HClO_4$ at 25 °C. The excitation wavelength was 475 nm.

characteristic $\pi\pi^*$ absorptions appear at 375 nm for the reduced polypyridyl ligand radical anion characteristic of the MLCT excited state, along with a prominent ground-state bleach of ^{1}MLCT absorption band of **A** and **B** at 450 nm. For **1** and **2** the transient absorption feature at 375 nm disappears rapidly (<1 ns) leaving behind the 450 nm bleach. These spectral changes are a clear signature of electron injection from the assembly into TiO_2. On longer time scales, 100s of ns, the bleach recovers, due to recombination by back electron transfer of the injected electron in TiO_2 with the oxidized chromophore on the surface.

The intensity of the transient absorption signal at 375 nm is shown as a function of pump–probe delay in Figure 4. For both **1** and **2** an initial decay in the absorbance occurs in the first 20 ps (Figure 4a), indicative of rapid electron injection by **1*** and by inner chromophore **A*** in **2** (eqs 1b and 3b in Scheme 1). There is a presumably sub-100 fs injection component that lies within the instrument response and is not detected here, but has been reported for similar systems.[18] The initial decay is followed by a slower decay which becomes a bleach feature on the 100 ps to 1 ns time scale.[19] Kinetic analysis of the time-dependent absorbance changes for **1** and **2** over this time range (Figure 4a) were fit to biexponential kinetics with τ_1 = 20 and τ_2 = 200 ps (Table S3) with the difference being in the amplitudes. We estimate an injection efficiency for assembly **1** to be 56% based on the amplitude of the 405 nm transient absorption at 1 ns (SI).[17]

After 1 ns (Figure 4b), **1** decays by complex nonexponential kinetics over a period of several microseconds as found for **RuP** on TiO_2.[17] This is consistent with slow back electron transfer process (eq 5). Assembly **2**, on the other hand, shows a continued decrease in the amplitude of the excited-state absorption band over the next 100 ns, followed by a slow decay back to zero. Kinetic analysis of the data by multiexponential fit resulted in τ = 20 ns for the growth of a negative signal (Table S4).

The continued loss of excited-state absorption in **2** is indicative of delayed injection into TiO_2 that occurs with a 20 ns time constant. We attribute this delayed injection to excitation of the outer chromophore **B**, which then either injects remotely (eq 3a), or undergoes energy transfer to **A** (eq 2) followed by fast electron injection (eq 3b). Given the similarity in time scale for loss of excited-state absorption in **2** (20 ns) and intra-assembly energy transfer on ZrO_2 (~30 ns), we ascribe the delayed injection to the latter. In either case, these results point to high efficiency, ~96%, energy transfer/electron injection based on the relative lifetimes for excited-state decay (τ ~ 490 ns) and energy transfer/injection, and imply an injection efficiency for **2** of 54%. Therefore, **2** is an efficient antenna for interfacial sensitization by energy transfer.

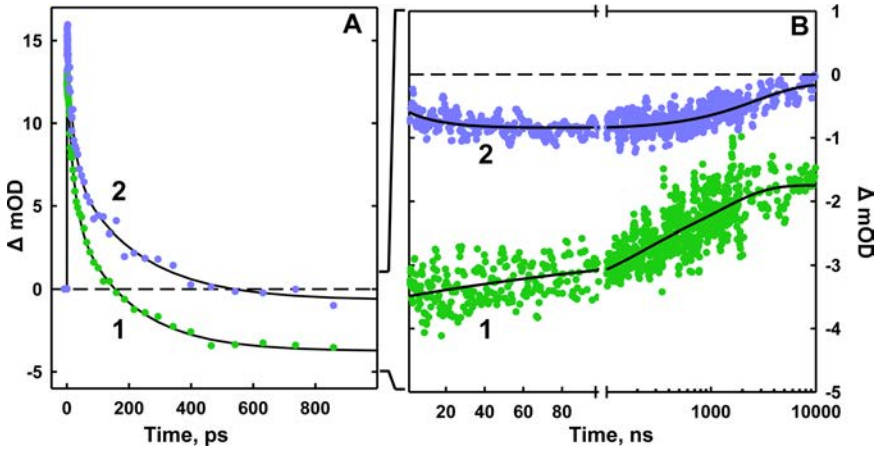

Figure 4. Transient absorption kinetics and fits of the $\pi\pi^*$ absorption (375 nm ±3 nm) for **1** (green) and **2** (blue) in a) the first 1000 ps and b) 1 to 10,000 ns after excitation at 475 nm. All samples were on 3 μm thick nanocrystalline TiO_2 film in aqueous 0.1 M $HClO_4$ solution at 25 °C.

dx.doi.org/10.1021/ja312143h | J. Am. Chem. Soc. 2013, 135, 5250–5253

The rates of back electron transfer are reflected in the decay of the ground-state bleach transient absorption signal at 450 nm (Figure S10). The back electron transfer kinetics for **1** and **2** exhibit multiexponential behavior due to the variety of back electron migration pathways in TiO_2, as shown previously for **RuP** under the same conditions.[17] The average lifetimes for recovery of the bleach at 450 nm, $\langle\tau\rangle$, are 19 and 11 μs for assemblies **1** and **2**, respectively, compared to 17 μs for **RuP** (Table S5).[17] While the average back electron transfer time exceeds a microsecond, there is 20 ns component resulting presumably from direct excitation of **A** (eq 1b) that occurs along with the slower injection arising from excitation of **B** (Table S5). This 20 ns back electron transfer component makes it problematic to draw quantitative conclusions regarding injection efficiencies from the amplitudes of the kinetic components.

Our results are notable in introducing a new, modular approach to the synthesis of preorganized and highly tunable assemblies for interfacial molecular energy conversion using solid-phase peptide synthesis coupled with 'click' chemistry. We have demonstrated that such scaffolds maintain their secondary structure in solution and on surfaces as well as provide the necessary arrangement of chromophores for directional energy transfer followed by electron injection into TiO_2. We are currently synthesizing a family of multichromophoric oligoprolines to explore the distance dependence of intra-assembly electron and energy transfer. Additionally chromophore-catalyst assemblies are being investigated for applications in dye-sensitized photoelectrosynthesis cells.

■ ASSOCIATED CONTENT

Ⓢ Supporting Information

Experimental, theoretical methods, and data analysis. This material is available free of charge via the Internet at http://pubs.acs.org.

■ AUTHOR INFORMATION

Corresponding Author

mlwaters@email.unc.edu; john_papanikolas@unc.edu

Author Contributions

[§]These authors contributed equally.

Notes

The authors declare no competing financial interest.

■ ACKNOWLEDGMENTS

This material is based upon work wholly supported as part of the UNC EFRC Center for Solar Fuels, an Energy Frontier Research Center funded by the U.S. Department of Energy, Office of Science, Office of Basic Energy Sciences under award no. DE-SC0001011. We acknowledge the UNC SERC Instrumentation Facility funded by the U.S. Department of Energy, Office of Energy Efficiency and Renewable Energy, award no. DE-EE0003188.

■ REFERENCES

(1) Ferreira, K. N.; Iverson, T. M.; Maghlaoui, K.; Barber, J.; Iwata, S. *Science* **2004**, *303*, 1831.

(2) Gagliardi, C. J.; Vannucci, A. K.; Concepcion, J. J.; Chen, Z.; Amadelli, T. J. *Energy Environ. Sci.* **2012**, *5*, 7704.

(3) Kümin, M.; Sonntag, L.-S.; Wennemers, H. *J. Am. Chem. Soc.* **2007**, *129*, 466.

(4) Mozer, A. J.; Griffith, M. J.; Tsekouras, G.; Wagner, P.; Wallace, G. G.; Mori, S.; Sunahara, K.; Miyashita, M.; Earles, J. C.; Gordon, K. C.; Du, L.; Katoh, R.; Furube, A.; Officer, D. L. *J. Am. Chem. Soc.* **2009**, *131*, 15621. Uetomo, A.; Kozaki, M.; Suzuki, S.; Yamanaka, K.; Ito, O.; Okada, K. *J. Am. Chem. Soc.* **2011**, *133*, 13276.

(5) Fang, Z.; Eshbaugh, A. A.; Schanze, K. S. *J. Am. Chem. Soc.* **2011**, *133*, 3063. Liu, Y.; Summers, M. A.; Edder, C.; Fréchet, J. M. J.; McGehee, M. D. *Adv. Mater.* **2005**, *17*, 2960. Kim, Y.-G.; Walker, J.; Samuelson, L. A.; Kumar, J. *Nano Lett.* **2003**, *3*, 523. Wang, L.; Puodziukynaite, E.; Vary, R. P.; Grumstrup, E. M.; Walczak, R. M.; Zolotarskaya, O. Y.; Schanze, K. S.; Reynolds, J. R.; Papanikolas, J. M. *J. Phys. Chem. Lett.* **2012**, *3*, 2453.

(6) Dutta, P. K.; Varghese, R.; Nangreave, J.; Lin, S.; Yan, H.; Liu, Y. *J. Am. Chem. Soc.* **2011**, *133*, 11985. Garo, F.; Häner, R. *Angew. Chem., Int. Ed.* **2012**, *51*, 916.

(7) Gilat, S. L.; Adronov, A.; Fréchet, J. M. J. *Angew. Chem., Int. Ed.* **1999**, *38*, 1422. Hasobe, T.; Kashiwagi, Y.; Absalom, M. A.; Sly, J.; Hosomizu, K.; Crossley, M. J.; Imahori, H.; Kamat, P. V.; Fukuzumi, S. *Adv. Mater.* **2004**, *16*, 975.

(8) Lee, C. Y.; Farha, O. K.; Hong, B. J.; Sarjeant, A. A.; Nguyen, S. T.; Hupp, J. T. *J. Am. Chem. Soc.* **2011**, *133*, 15858. Kent, C. A.; Liu, D.; Ma, L.; Papanikolas, J. M.; Meyer, T. J.; Lin, W. *J. Am. Chem. Soc.* **2011**, *133*, 12940.

(9) Hu, K.; Robson, K. C. D.; Johansson, P. G.; Berlinguette, C. P.; Meyer, G. J. *J. Am. Chem. Soc.* **2012**, *134*, 8352. Huang, Z.; Geletii, Y. V.; Musaev, D. G.; Hill, C. L.; Lian, T. *Ind. Eng. Chem. Res.* **2012**, *51*, 11850.

(10) O'Regan, B.; Grätzel, M. *Nature* **1991**, *353*, 737.

(11) Song, W.; Chen, Z.; Brennaman, M. K.; Concepcion, J. J.; Patrocinio, A. O. T.; Murakami Iha, N. Y.; Meyer, T. J. *Pure Appl. Chem.* **2011**, *83*, 749.

(12) O'Regan, B.; Gratzel, M. *Nature* **1991**, *353*, 737. Amadelli, R.; Argazzi, R.; Bignozzi, C. A.; Scandola, F. *J. Am. Chem. Soc.* **1990**, *112*, 7099. Parussulo, A. L. A.; Iglesias, B. A.; Toma, H. E.; Araki, K. *Chem Commun.* **2012**, *48*, 6939. Kleverlaan, C.; Alebbi, M.; Argazzi, R.; Bignozzi, C. A.; Hasselmann, G. M.; Meyer, G. J. *Inorg. Chem.* **2000**, *39*, 1342.

(13) Deber, C. M.; Bovey, F. A.; Carver, J. P.; Blout, E. R. *J. Am. Chem. Soc.* **1970**, *92*, 6191.

(14) Serron, S. A.; Aldridge, W. S; Fleming, C. N.; Danell, R. M.; Baik, M.-H.; Sykora, M.; Dattelbaum, D. M.; Meyer, T. J. *J. Am. Chem. Soc.* **2004**, *126*, 14506. Striplin, D. R.; Reece, S. Y.; McCafferty, D. G.; Wall, C. G.; Friesen, D. A.; Erickson, B. W.; Meyer, T. J. *J. Am. Chem. Soc.* **2004**, *126*, 5282.

(15) Springer, J. W.; Parkes-Loach, P. S.; Reddy, K. R.; Krayer, M.; Jiao, J.; Lee, G. M.; Niedzwiedzki, D. M.; Harris, M. A.; Kirmaier, C.; Bocian, D. F.; Lindsey, J. S.; Holten, D.; Loach, P. A. *J. Am. Chem. Soc.* **2012**, *134*, 4589. Channon, K. J.; Devlin, G. L.; MacPhee, C. E. *J. Am. Chem. Soc.* **2009**, *131*, 12520. Hong, J.; Kharenko, O. A.; Ogawa, M. Y. *Inorg. Chem.* **2006**, *45*, 9974. Knorr, A.; Galoppini, E.; Fox, M. A. *J. Phys. Org. Chem.* **1997**, *10*, 484. Wilger, D. J.; Bettis, S. E.; Materese, C. K.; Minakova, M.; Papoian, G. A.; Papanikolas, J. M.; Waters, M. L. *Inorg. Chem.* **2012**, *51*, 11324. Hanson, K.; Wilger, D.; Jones, S. T.; Harrision, D. P.; Bettis, S. E.; Luo, H.; Papanikolas, J. M.; Waters, M. L.; Meyer, T. J. *Biopolymers* **2013**, *100*, 25.

(16) Hanson, K.; Brennaman, M. K.; Luo, H.; Glasson, C. R. K.; Concepcion, J. J.; Song, W.; Meyer, T. J. *ACS Appl. Mater. Interfaces* **2012**, *4*, 1462.

(17) Hanson, K.; Brennaman, M. K.; Ito, A.; Luo, H.; Song, W.; Parker, K. A.; Ghosh, R.; Norris, M. R.; Glasson, C. R. K.; Concepcion, J. J.; Lopez, R.; Meyer, T. J. *J. Phys. Chem. C.* **2012**, *116*, 14837.

(18) Asbury, J. B.; Ellingson, R. J.; Ghosh, H. N.; Ferrere, S.; Nozik, A. J.; Lian, T. *J. Phys. Chem. B* **1999**, *103*, 3110.

(19) Although dominated by the excited-state absorption at early times, the transient absorption signal has contributions from positive going signal due to the appearance of excited-state absorption and a negative going signal due to loss of ground-state absorption, i.e., bleach. The approach to an overall negative signal at 375 nm reflects the presence of a small bleach contribution at this wavelength that becomes apparent as the excited-state absorption band disappears due to injection.